Universidad de Valladolid

ESCUELA DE INGENIERÍAS INDUSTRIALES

UNIVERSIDAD DE VALLADOLID

ESCUELA DE INGENIERIAS INDUSTRIALES

Grado en Ingeniería Química

ENHANCEMENT OF REDOX PROPERTIES OF IRON OXIDE THROUGH METAL MODIFICATION IN CATALYST ASSISTED CHEMICAL LOOPING

Autor:

Santander de Soto, Laura

Responsable de Intercambio en la Uva:

Bolado Rodríguez, Silvia

Ghent University

Valladolid, Junio de 2016.

TFG REALIZADO EN PROGRAMA DE INTERCAMBIO

TÍTULO: Enhancement of redox properties of iron oxide through metal modification in catalyst assisted chemical looping

ALUMNO: Laura Santander de Soto

FECHA: 22 Abril de 2016

CENTRO: Laboratory for Chemical Technology

TUTOR: Aditya Dharanipragada Naga Venkata Ranga

PROMOTOR: Dr. Vladimir Galvita

ABSTRACT

El objetivo de este trabajo es investigar el comportamiento de ciertos materiales bifuncionales mediante catálisis asistida en un proceso llamado Chemical Looping. La necesidad de obtener energía ha llevado a un considerable aumento del contenido de CO_2 en la atmósfera a lo largo de las últimas décadas (principal fuente de emisión: combustibles fósiles). Por ello, hoy en día, el uso de energías renovables o la reutilización de CO_2 están ganando fuerza. Surge así el proceso Chemical Looping mediante el cual se puede obtener hidrógeno (fuente de energía limpia) o transformar CO_2 en CO. Se trata de un proceso cíclico a través de un transportador de oxígeno que es reducido (con CH_3OH o C_2H_5OH) y reoxidado (CO_2 o H_2O). Diferentes ferritas ($CoFe_2O_4$ y $NiFe_2O_4$) modificadas mediante $CeZrO_2$ fueron sintetizadas vía método de coprecipitación. La caracterización y análisis de la estabilidad y actividad rédox se llevaron a cabo mediante XRD, B.E.T., TEM-EDX, TPR/TPO… El material más estable y activo resultó ser 20wt%$CoFe_2O_4$-$CeZrO_2$.

KEYWORDS

Chemical looping, transportador de oxígeno, ferritas, metanol, hidrógeno.

Enhancement of redox properties of iron oxide through metal modification in catalyst assisted chemical looping

Laura Santander de Soto

Supervisor: Dr. Vladimir Galvita, Dr. Hilde Poelman
Counsellor: Aditya Dharanipragda

Master's dissertation submitted in order to obtain the academic degree of
Master of Science in Chemical Engineering

Department of Chemical Engineering and Technical Chemistry
Chair: Prof. Dr. ir. Guy Marin
Faculty of Engineering and Architecture
Academic year 2015-2016

UNIVERSITEIT GENT

UNIVERSITEIT GENT

FACULTY OF **ENGINEERING AND ARCHITECTURE**

Department of Chemical Engineering and Technical Chemistry
Laboratory for Chemical Technology
Director: Prof. Dr. Ir. Guy B. Marin

Laboratory for Chemical Technology

Declaration concerning the accessibility of the master thesis

Undersigned,

Laura Santander de Soto

Graduated from Ghent University, academic year 2015-2016 and is author of the master thesis with title:

Enhancement of redox properties of iron oxide through metal modification in catalyst assisted chemical looping

Preface

After almost 8 months far from my home working on my Master thesis, I can undoubtedly affirm that it has been a long and not easy way but very gratifying. This great experience has helped me to grow up as person, to be more independent, to value how lucky we are, to appreciate much more each person around me and to be more aware of every effort has a reward and, mine, it has been everything what I have learnt here in Ghent and at the Departament of Chemical Engineering and Technical Chemistry.

This had never been possible without some colaborations. Thank University of Valladolid for having entrusted me and, also, thank University of Ghent for giving me the chance to study here.

I am also very grateful to my counsellor Aditya Dharanipragada for his patience, his time and his dedication teaching and helping me. Also I would like to thank Dr. Vladimir for his advice and his help during my master thesis. I am thankful to Stavros Theofanidis and Lukas Buelens for their assistance in some issues with experimental setups. Finally, I am very grateful to Prof. Dr. ir. Guy B Marin for bringing me the opportunity to carry out my master thesis at the Laboratory for Chemical Technology.

Without forgetting, all my loved ones who always support me and they are available for everything what I need.

Abstract

The focus of this work is to investigate the behavior of bifunctional materials in catalyst assisted chemical looping process. Different ferrite ($CoFe_2O_4$ and $NiFe_2O_4$) materials modified by $CeZrO_2$ were synthesized via co-precipitation method. Characterization was performed by several analytical techniques such as in-situ XRD, B.E.T., TEM-EDX, etc. The redox activity and stability at different temperatures (500^oC and 750^oC) were studied in order to determine the most stable bifunctional material. The chemical looping reforming was carried out in two stages, in the first step the bifunctional material was reduced by CH_3OH or C_2H_5OH. In the second step H_2O or CO_2 were used for regeneration of to study the production of high purity H_2 and CO. Addition of $CeZrO_2$ improved the redox behavior of ferrite materials. Among the modified ferrite materials $CoFe_2O_4$ were the best performing materials as they could reduce and reoxidize to the as prepared state. The most stable material was 20wt%$CoFe_2O_4$-$CeZrO_2$ during methanol and ethanol chemical looping. $NiFe_2O_4$ supported materials suffered from deactivation due to phase transformation as they could not cycle back to spinel ($NiFe_2O_4$) phase.

***Keywords*- Chemical looping process, ethanol, methanol, ferrites, spinel, oxygen storage material.**

Enhancement of redox properties of iron oxide through metal modification in catalyst assisted chemical looping

Laura Santander de Soto

Supervisor(s): Dr. Vladimir Galvita, Dr. Hilde Poelman

Counsellor: Aditya Dharanipragada

Abstract- The focus of this work is to investigate the behavior of bifunctional materials in catalyst assisted chemical looping process. Different ferrite ($CoFe_2O_4$ and $NiFe_2O_4$) materials modified by $CeZrO_2$ were synthesized via co-precipitation method. Characterization was performed by several analytical techniques such as in-situ XRD, B.E.T., TEM-EDX, etc. The redox activity and stability at different temperatures (500°C and 750°C) were studied in order to determine the most stable bifunctional material. The chemical looping reforming was carried out in two stages, in the first step the bifunctional material was reduced by CH_3OH or C_2H_5OH. In the second step H_2O or CO_2 were used for regeneration of to study the production of high purity H_2 and CO. Addition of $CeZrO_2$ improved the redox behavior of ferrite materials. Among the modified ferrite materials $CoFe_2O_4$ were the best performing materials as they could reduce and reoxidize to the as prepared state. The most stable material was 20wt%$CoFe_2O_4$-$CeZrO_2$ during methanol and ethanol chemical looping. $NiFe_2O_4$ supported materials suffered from deactivation due to phase transformation as they could not cycle back to spinel ($NiFe_2O_4$) phase.

***Keywords*- chemical looping process, ethanol, methanol, ferrites, spinel, oxygen storage material.**

I. INTRODUCTION

Over the past centuries, human dependence on fossil fuels has increased exponentially. This has led to a considerable greenhouse emission (CO_x, NO_x and SO_x) rise incrementing average global temperature. Nowadays, CO_2 is the largest contributor, its global atmospheric content is more than 390 ppn[1] since approximately 30 billion tons per year are emitted[2]. Fossil fuel combustion is responsible for more than 65% according to IPPC. In order to mitigate CO_2 emissions, renewable energy sources are increasingly in development. Chemical looping process is a promising alternative to conventional H_2 and syngas production networks, which leads to value added chemicals. It is a cyclic process through an oxygen carrier which is, respectively, reduced and reoxidized using feed fuels like CH_3OH, C_2H_5OH or bio-gas as reducing agent and H_2O/CO_2 as oxidizer. Iron oxides are the most applied as oxygen carrier due to its high oxygen storage capacity, its abundant availability, its environmental compatibility and its low cost[1], [3], [4]. To improve reduction process splitting oxidative carbon products, iron oxides are modified with metals forming ferrites[1]. On the basis of literature, Co and Ni have been studied in this work. However, ferrites tend to deactivate because of sintering[5] so stability is enhanced with promoter elements addition, ex: $CeZrO_2$ possess assuring mechanical and redox properties towards chemical looping[6].

Laura Santander, Chemical Engineering Department, Ghent University (UGent), Gent, Belgium. E-mail: laura.santanderdesoto@Ugent.be

Thus, $CeZrO_2$ promoted ferrites solid oxygen storage materials seem to be good candidates for performing chemical looping dry and steam reforming in an efficient way. The objective is to find the best performing material to produce high purity H_2 or CO and value added chemicals.

II. MATERIALS AND SETUP

A. Material Preparation

Samples containing 100, 80, 50 and 20 wt% of $CoFe_2O_4/NiFe_2O_4$ promoted by $CeZrO_2$ were synthesized via co-precipitation method. Precursors were dissolved in deionized water and subjected to stirring in order to homogenize the mixture. Ammonium hydroxide base solution was added dropwise until reaching a constant pH around 10-11. Post-treatment consisted of vacuum filtration, drying in an oven (240 °C), crushing and calcining (650 °C and 750°C). $Fe(NO_3)_3 \cdot 9H_2O$, $Co(NO_3)_2 \cdot 6H_2O$, $Ni(NO_3)_2 \cdot 6H_2O$, $ZrO(NO_3)_2 \cdot xH_2O$, $Ce(NO_3)_3 \cdot 6H_2O$ were used as precursors for metals and pH was controlled by ammonium hydroxide.
All chemicals were supplied by Sigma-Aldrich®.

B. Material Characterization Techniques

B.E.T. N_2-adsorption experiments were performed on Micrometrics Tristar II 3020. TEM imaging was done with JEOL JEM-2200 setup and EDX analysis was performed by EDAX Genesis 4000. XRD was performed with a Siemens Kristalloflex D5000 and in situ XRD analysis on phase transformation was performed in Bruker Discover D8 (Vantec linear detector) setup. For Temperature-Programmed reduction and oxidation, Micrometrics Autochem II 2920 was utilized. Cyclic stability was tested in Step Response reactor setup.

III. RESULTS AND DISCUSSION

A. Transmission Electron Microscopy (TEM) and Energy Dispersive X-Ray analysis (EDX).

On Figure 1a, fresh 20wt% $CoFe_2O_4$-$CeZrO_2$ sample morphology with crystallite sizes varying between ~10-20 nm is showed. Fe and Co are uniformly dispersed (Figure 1b) indicating $CoFe_2O_4$ formation. $CeZrO_2$ support is also formed according to their uniform distribution exhibited in Figure 1c. On Figure 2, same sample is showed after methanol redox cycles. Diameter has increased with values in order of ~30-50 nm due to sintering. Figure 2b shows large crystals of Co and Fe together in form of spinel phase. However, Fe also remains dispersed along with C (Figure 2c) forming carbides which lead to deactivation.

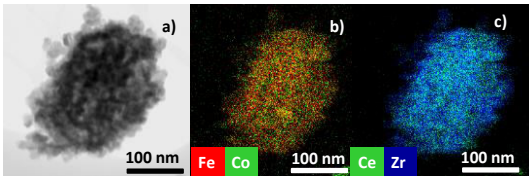

Figure 1 – TEM-EDX images of fresh $20CoFe_2O_4/80CeZrO_2$,: a) morphology, b) elemental mapping of Fe and Co, c) elemental mapping of Ce and Zr.

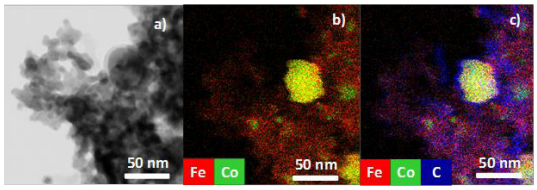

Figure 2 – TEM-EDX images of $20CoFe_2O_4/80CeZrO_2$ after methanol redox cycles,: a) morphology, b) elemental mapping of Fe and Co, c) elemental mapping of Fe, Co, C..

B. *Temperature programmed reaction.*

Redox properties on bulk iron oxides and modified ferrites were tested by means of H_2-TPR and CO_2-TPO measurements. Ferrite materials resulted in enhanced redox properties in comparison to bulk Fe_2O_3. However, second cycle of both Co and Ni ferrites does not show the same behavior due to deactivation because of phase segregation and sintering. Thus, $CeZrO_2$ supported ferrites have been investigated leading to repeated reduction and oxidation cycles at similar temperatures.

C. *In situ XRD analysis*

In-situ XRD analyses performed in prior $CoFe_2O_4$ manifested spinel segregation into metallic Co and Fe_3O_4 instead of cycling back during oxidation. For prior $NiFe_2O_4$, alloy formed during reduction remained stable and only traces of magnetite were observed in patterns. This is in agreement from H_2-TPR and CO_2-TPO study.

In order to understand phase transformations responsible for the repeated reduction and oxidation, an in-situ XRD study was carried out. Alloy formation during reduction occurred at a relatively lower temperature (460 ºC) for Co supported ferrites and it was reoxidized to spinel original state at 600ºC without any segregation. However for Ni ferrites, despite repeated cycles achieved, alloy remained stable with some decomposition into Ni which gave rise to Fe segregation.

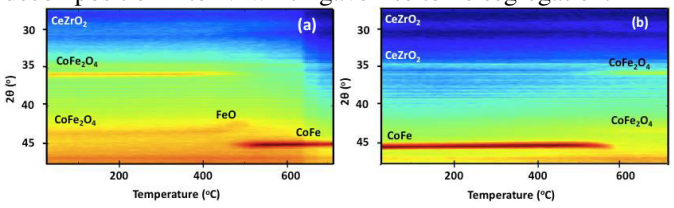

Figure 3 – In-situ XRD for $80wt\%CoFe_2O_4$-$CeZrO_2$: a) H_2-TPR and b) CO_2-TPO.

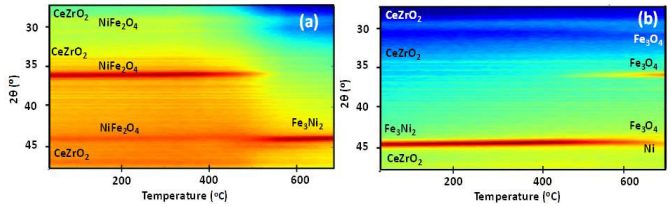

Figure 4 – In-situ XRD for $80wt\%NiFe_2O_4$-$CeZrO_2$: a) H_2-TPR and b) CO_2-TPO.

D. *N_2- adsorption*

The B.E.T measurements showed that the surface area increased with the progressive loading of $CeZrO_2$. Highest specific surface area of 42 m^2/g was obtained in $20wt\%$ $CoFe_2O_4$-$CeZrO_2$.

E. *Cyclic stability*

On Figure 5, different oxygen storage materials are compared. Activity and stability were studied by means of three different stages of redox process. First, methanol/ethanol decomposition activity into syngas was investigated along with CO_2 regeneration and He purging in between. Secondly, a pre-treatment was performed to test stability after 100 cycles upon H_2-reduction and CO_2-reoxidation. Finally, to test activity, four more cycles were undertaken under the same conditions as first stage. The highest CO_2 conversion to CO is attained by $20wt\%CoFe_2O_4$-$CeZrO_2$ using methanol as feed gas. During the first three cycles rapid deactivation is observed. This deactivation can be attributed to carbon formation whereas in the pretreatment step with H_2 and CO_2 the effect of sintering and stability during prolonged redox cycles was investigated.

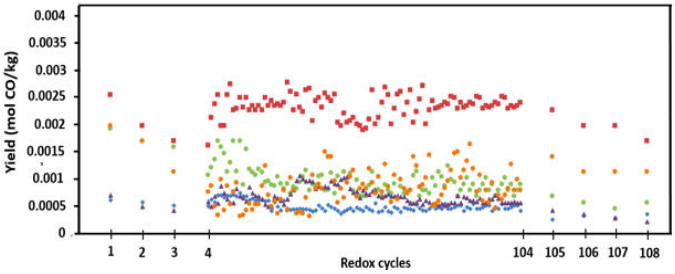

Figure 5 - Estimated CO yield for CO_2 conversion over several redox cycles at 500 ºC. (■) $20wt\%CoFe_2O_4$-$CeZrO_2$,

IV. CONCLUSION

Among the modified ferrite materials, $CoFe_2O_4$ with $CeZrO_2$ were the most active and stable in comparison to $NiFe_2O_4/CeZrO_2$. These ferrite materials could reduce and reoxidize to as prepared state. However deactivation due to carbon formation and sintering was observed in both the bifunctional materials. The carbon formation hinders the ability to form high purity H_2, but however these materials due to their improved oxygen storage characteristics can be used as a H_2 storage material. The material can be pre reduced with H_2 and then oxidized by H_2O to produce high purity H_2 which can be used in fuel cell based automobile applications. In this way it could be potential clean energy technology.

REFERENCES

[1] J. Adanez, A. Abad, F. Garcia-Labiano, P. Gayan, and L. F. De Diego, "Progress in chemical-looping combustion and reforming technologies," *Prog. Energy Combust. Sci.*, vol. 38, no. 2, pp. 215–282, 2012.

[2] J. Adánez, L. F. De Diego, F. García-Labiano, P. Gayán, A. Abad, and J. M. Palacios, "Selection of oxygen carriers for chemical-looping combustion," *Energy and Fuels*, vol. 18, no. 2, pp. 371–377, 2004.

[3] V. J. Aston, B. W. Evanko, and A. W. Weimer, "Investigation of novel mixed metal ferrites for pure H 2 and CO 2 production using chemical looping," *Int. J. Hydrogen Energy*, vol. 38, no. 22, pp. 9085–9096, 2013.

[4] M. Najera, R. Solunke, T. Gardner, and G. Veser, "Carbon capture and utilization via chemical looping dry reforming," *Chem. Eng. Res. Des.*, vol. 89, no. 9, pp. 1533–1543, 2011.

[5] V. V. Galvita, H. Poelman, C. Detavernier, and G. B. Marin, "Catalyst-assisted chemical looping for CO2 conversion to CO," *Appl. Catal. B Environ.*, vol. 164, pp. 184–191, 2015.

[6] V. V Galvita, H. Poelman, V. Bliznuk, C. Detavernier, and G. B. Marin, "CeO 2 - Modified Fe 2 O 3 for CO 2 Utilization via Chemical Looping," *Ind. Eng. Chem. Res.*, vol. 52, no. 25, pp. 8416–8426, 2013.

Table of Contents

List of symbols and acronyms

Symbol	Description	Units	Remarks
A	Concentration of gas phase molecules	ml/m^3 STP	Used in B.E.T. theory calculations
a_m	Molecular surface area	m^2	B.E.T. equation
a_s	Specific surface area	m^2/g	B.E.T. equation
b	Instrumental width	rad, deg	Scherrer equation
c	Molar concentration	mol/m^3	Lambert-Beer Law
c_n	Storage capacity	g CO_2/g	n corresponds to a determinate number of cycles
d	Plane distance	nm	Distance between two lattice planes
d	Path length	m	Lambert-Beer Law
d_{XRD}	Particle dimension	nm	Used for XRD measurements
E_1	heat of adsorption for the first layer	J/kg	Used in B.E.T. equation
E_L	heat of adsorption for the second and higher layers	J/kg	Used in B.E.T. equation
K	Dimesionless shape factor	-	Scherrer equation
K_α			XRD
I	Measured intensity		Lambert-Beer Law
I_o	Measured reference intensity		Lambert-Beer Law
m_{ox}	mass of oxidized metal	g	
m_{red}	mass of reduced metal	g	
MW_i	Molecular Weight of component i	g/mol	
n	Cycle number	-	Integer number
n	Positive integer (order of reflection)	-	Bragg's Law
N_A	Avogadro's Constant	mol^{-1}	The value of this constant is : $6.022 \cdot 10^{23}$ mol^{-1}
n_{CO}	Mole of CO produced	mol	
$n_{f,o}$	Initial molar amount of fuel	mol	
n_f	Final molar amount of fuel	mol	Molar amount of fuel at certain cycle n
p_A	Saturated pressure of adsorbate gas	Pa	B.E.T. equation
p_i	Partial pressure of component i	Pa	B.E.T. equation
p^0	Vapor pressure	Pa	B.E.T. equation
R	Constant of Ideal Gases	J/mol ·°C	Value of gas constant: 8.314 J/mol ·°C
s_i	Surface area	m^2/g	
ss	Specific surface area	m^2/m^3	
T	Temperature	°C	
V_m	Theoretical monolayer adsorption capacity	ml STP	B.E.T. equation
W	Sample weight		B.E.T. equation
W_{Fe}	Mass of oxygen carrier material	kg	Yield
X_f	Fuel conversion		
Xi	Fraction of active metal oxide in the sample		

Greek symbol	Description	Units	Remarks
β	Peak width	deg, rad	Full width half maximun according to Scherrer's equation
β	Linear heating rate	°C/min	Parameter in TPR
θ	Diffraction angle	deg, rad	Angle between incoming X-rays and the normal to the reflecting lattice plane.
λ	X-ray wavelength	nm	Scherrer's and Bragg's law
$\Delta H°_r$	Standard reaction enthalpy	kJ/mol	Standard reaction enthalpy per mole of reaction

Acronym	Description	Remarks
AES	Atomic Emission Spectroscopy	Determine elemental composition
B.E.T.	Brunauer,emett, Teller	Theory of N_2-adsorption
CLC	Chemical Loopig Combustion	
CLDR	Chemical Looping Dry Reforming	
CLP	Chemical Looping Process	
CLSR	Chemical Looping Steam Reforming	
CP	Co-precipitation	Material preparation method
EDX	Energy-dispersive X-ray spectroscopy	
FWHM	Full Widh Half Maximun	Scherrer's equation
HTWGS	High Temperature Water shift	
ICP	Inductively Coupled Plasma	
IPCC	Intergovernmental Panel on Climate Control	
LTWGS	Low Temperature Water gas shift	
M	Metal in its reduced form	
MeO	Metal in its oxidized form	
MS	Mass Spectrometer	
OC	Oxygen Carrier	
OES	Optical Emission Spectroscopy	Determine elemental composition
RT	Room Temperature	
SSA	Specific surface Area	
STP	Standard Temperature and Pressure	T=273.15 K and P=1.013 bar
TCD	Thermal Conductivity Detector	
TEM	Transmission Electron Microscopy	
TPO	Temperature-Programmed Oxidation	
TPR	Temperature-Programmed Reduction	Also Temperature-Programmed Reaction
WGS	Water Gas shift reaction	
XRD	X-Ray Diffraction	To determine the crystalline structure

CHAPTER 1 INTRODUCTION

Since the industrial revolution, human dependence on fossil fuels has increased exponentially. This has resulted in increased emission of greenhouse gases (CO_x, NO_x and SO_x) which are responsible towards global warming [1]. Thus there is a need to minimize the dependence on fossil fuels and rely on clean energy renewable sources. One of the abundant inexpensive renewable source of chemicals and energy is biomass. Feedstocks containing alcohols especially methanol and ethanol due to high carbon to hydrogen ratio and their easy biomass derivability are promising towards clean energy production [2], [3]. One attractive process to convert these fuels to value added chemicals and produce high purity H_2/CO is chemical looping process.

It is a cyclic process based on the periodic reduction and reoxidation of the oxygen storage material [4]. During this process, the oxygen storage material is reduced by feed (ex: CH_3OH, C_2H_5OH or bio-gas) to produce value added chemicals. Then in the second step H_2O/CO_2 is used again as a reoxidation agent to regenerate the material resulting in the production of high purity H_2/CO. However the operating temperatures and stability are governed by the oxygen storage materials. The most widely investigated materials as oxygen storage materials are the transition metal oxides (Fe, Ni, Cu)[5]. However among these, iron oxides due to the high oxygen storage capacity, abundant availability and environmentally friendly are widely applied [6]. The oxygen carriers are usually novel metal materials that can be modified to improve redox properties. In the present study the chemical looping approach consists of two-steps i.e., first the reduction of a modified metal oxide by a reducing agent, which is oxidized to carbon oxides, hydrogen and water, followed by the re-oxidation of the pre-reduced oxide with H_2O or CO_2, to produce high purity H_2 or CO respectively.

However when iron oxides are applied in chemical looping processes with hydrocarbon containing feed ex: bio gas (CH_4, H_2O) as a feed, the reduction step produces CO_2 and H_2O along with H_2 and CO. The oxidizing gases produced during reduction of methane limit the kinetics in this step [7], [8]. In order to improve the kinetics of the reduction step an extra element is added to the oxygen storage material, which can split the oxidative products and enhance the reduction. Usually iron oxides are modified with metals to form ferrites. Among these Ni and Co based ferrites have been applied towards this process, [9], [10], however Co, Ni-ferrites tend to deactivate rapidly. In order to improve the stability, support such as $CeZrO_2$ are employed due to their promising mechanical and redox properties towards chemical looping. In this master thesis, the application of ferrite materials towards chemical looping process using methanol or ethanol as feed gas and H_2O/CO_2 as oxidizer has been investigated.

CHAPTER 2 LITERATURE SURVEY

The literature study mainly focusses on the applicability of chemical looping towards production of value added chemicals. It discusses the use of various potential feedstocks, and oxygen storage materials applied in this process. The importance of renewable feed stocks (ex: bio-ethanol and bio-methanol) and modified iron oxides materials are the major focus.

2.1 IMPORTANCE OF RENEWABLE ENERGY

The current rise in global temperatures because of the increase in the emission of greenhouse gases from the use of fossil fuels has been provoking a serious alarm. This has led to increased concern in global climate change and impose some restrictions on gases emissions.

Hence over the past decade the importance of using renewable sources to minimize greenhouse gases (SO_x, NO_x, CO_x) has been stressed. Among greenhouse gases, CO_2 due to a high residence time in the atmosphere poses a serious threat to the climate. The global atmospheric content of CO_2 has increased from 280 ppm to 390 ppm in the past decades [1] and, according to the Intergovernmental Panel on Climate Control (IPCC), the percent of carbon dioxide from fossil fuels combustion and industrial processes emitted to the atmosphere is 65%. Therefore, it was established that, by 2050, a considerable reduction is indispensable to control the global temperature rise lower than 2 °C [11] meaning that CO_2 concentrations cannot exceed 450 ppm [1].

In order to minimize the carbon dioxide emissions into the atmosphere, several technologies such as CO_2 capture and utilization techniques have gained significance. In this aspect chemical looping provides an interesting alternative towards CO_2 utilization. This process converts CO_2 to value added chemical such as CO which can be used as raw material for Fischer Tropsch processes.

The second alternative to minimize greenhouse gas emissions, is to rely on clean energy sources such as H_2. The use of Hydrogen as a clean energy fuel, is a promising alternative as the only by product resulting from the combustion is H_2O. However, the main challenge is to produce high purity hydrogen which can be used in fuel cell based technologies to produce energy in small scale ex: automobile engines and domestic household purposes. Feedstock containing alcohols, especially ethanol and methanol, are promising to produce hydrogen due to their biomass derivability, easy handling and high hydrogen to carbon ratio.

In the coming sections, the various conventional technologies to produce hydrogen will be described. Further, the simplicity and applicability of hydrogen energy production and advantages of CO_2 utilization through chemical looping are discussed.

2.1.1 Hydrogen applications

Hydrogen is used as a raw material in various applications ranging from small scale, e.g. hydrogenations in pharmaceuticals and fine chemicals, medium scale, e.g. manufacture of chemicals such as aniline, cyclohexanol and butanol, to large scale, e.g. manufacture of a number of important bulk chemicals like methanol, ammonia and sponge iron[3]. In addition, large amounts of hydrogen are consumed in different industrial processes like refining petroleum such as hydrodemetallation, hydrodewaxing, hydrodesulphurization, hydrocracking, hydrodenitrogenation, etc., treating metals, processing food and producing fertilizer.

As energy source, H_2 can be utilized in conventional electric power generation technologies, for transportation and for portable electronic devices like mobile phones and laptops [12]. For example, NASA (National Aeronautics and Space Administration) is an important user of hydrogen as fuel. At the beginning, liquid hydrogen was its rocket fuel and, moreover, NASA was one of the first to employ fuel cells to power electrical systems on space craft. The main exploitations of hydrogen as a clean energy source are in automobile engines, power plant turbines or in fuel cells.

- Transportation

Transportation applications include buses, trucks, passenger vehicles and trains. Search of hydrogen use in fuel cells and internal combustion engines (methanol systems also) is being a big challenge to overcome. [12] This work is conducted towards hydrogen production for using specially in automobiles and fuel cells. The infrastructure for fuel cells vehicles will be improved step by step because a lot of benefits over traditional vehicles can be procured from fuel cells such as energy security and reduced carbon dioxide emissions. [12]

- Stationary power generation

This point involves back-up power units, grid management, power for remote locations, stand-alone power plants for towns and cities, distributed generation for buildings and cogeneration [12].

- Portable power generation

Applications for fuel cells comprises consumer electronics, business machinery and recreational devices

2.1.2 Conventional methods to produce hydrogen

H_2 is the most abundant element in the Universe. Nevertheless, hydrogen in its elemental state is difficult to find on Earth. Hence should be generated/stored and used instantaneously. A wide variety of process technologies can be utilized to produce hydrogen, from fossil fuels (natural gas, coal) and renewable sources (water, biomass) to chemical and biological processes. The Figure 2.1 shows a scheme of the various sources to produce hydrogen energy. The most widely used methods for bulk H_2 production are: steam reforming, gasification of coal and other hydrocarbons, electrolysis of water, biomass conversion (thermochemical and biochemical processes). Steam reforming is the most industrially applied processes and is described in detail in the next section.

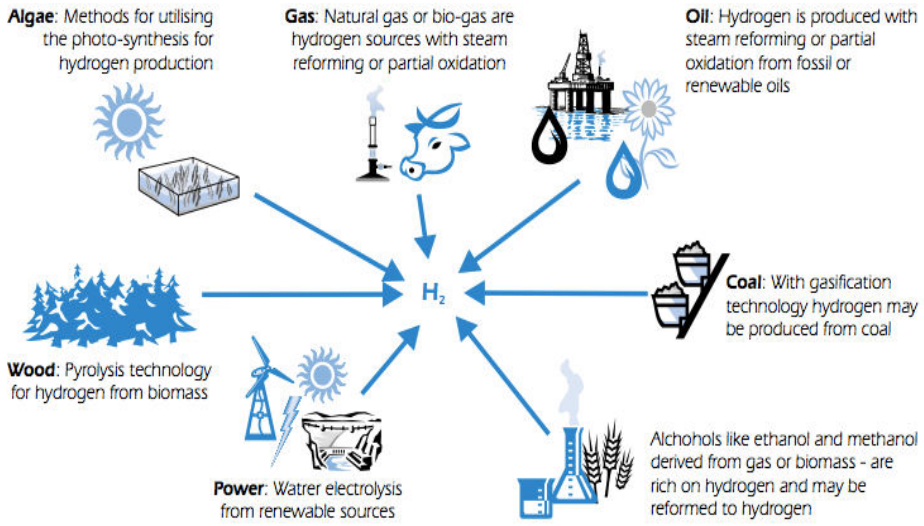

Figure 2.1 – Some feedstock and process alternatives [13]

Method	Process
Steam reforming	In presence of nickel catalyst & at 700 – 1100°C: $CH_4(g) + H_2O(g) \rightarrow CO(g) + 3H_2(g)$ Next reaction at lower temperature: $CO(g) + H_2O(g) \Rightarrow CO_2(g) + H_2(g)$
Gasification	At high temperature and pressure: $Coal + H_2O(g) + O_2(g) \Rightarrow$ syngas
Electrolysis	Electric current passed through water: $2H_2O(l) \Rightarrow 2H_2(g) + O_2(g)$

Method	Implementation	Advantages	Disadvantages
Steam reforming	Current major source of H_2	65-75 % Efficiency Economical (cheapest method) Established infrastructure	Nonrenewable source CO_2 emissions
Gasification	Current method of mass H_2 production	Large supplies of coal Inexpensive resources	CO_2 emissions 45% efficiency
Electrolysis	Not in so much use due to cost of electricity	Depend on electricity source	CO_2 emissions if coal is energy source. Production can require more energy than it is released.

Table 2.1 – Main methods to produce hydrogen [14]

2.1.2.1 Steam reforming network

It is the most common way to generate commercial bulk H_2 and it has dominated synthesis-gas production for 70 years. The process is performed in a reformer into which steam reacts with a hydrocarbon fuel (fossil fuel), typically natural gas whose main constituent is methane (CH_4) which possesses a high heating value and the greatest H/C ratio [15].

Scientists are continually looking for improvements in steam reforming such as catalysts, operation conditions and heat transfer. However, its intensive energy requirement is inevitable.[15] Steam reforming is entirely feasible thermodynamically and entangles the strongly endothermic conversion of fossil fuel (CH_4) and H_2O into H_2 and CO (Reaction 2.1) whose enthalpy is ΔH_r=206 kJ/mol [13].

$$CH_4 + H_2O\ (g) + heat \rightarrow CO + 3H_2 \qquad \textbf{Reaction 2.1}$$

Given that methane is not a reactive molecule because of the high energy of C-H bond (439 kJ/mol), the process normally takes place at high temperatures, between 700-850°C, and pressures of 3 to 25 bar.

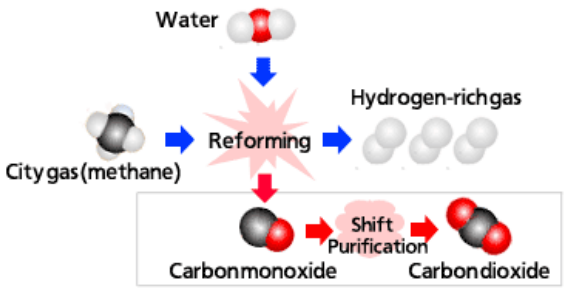

Figure 2.2. Steam reforming process

In consequence, the reaction catalyst has to be active and resistant in this regard the most widely used are nickel-based catalysts which are shown a reasonable methane conversion [16]. In fact, zirconium oxide was a good support according to Yasuyuki et al. [17]

Unfortunately, the efficiency of the process can decrease if the methane source used as feed gas contains some impurities of sulfur or other compounds since it would require a pre-treatment cleanup to remove them[18]. Besides, other issues are: a) thermodynamics confirms that only above 900°C higher conversions are achieved, however heat transfer coefficient is become the rate-limiting factor if working temperature is so elevated and b) thermodynamically, reduced species formation is favorable giving rise to carbon filaments (Boudouard reaction and coke deposition) covering nickel particles and its subsequent chemical deactivation or, even, catalyst breaking. If water is fed in excess, these problems could be solved.[19]

In addition, a membrane reactor has been proposed by Yasutuki Matsumura et al. in which hydrogen is separated from the mixture increasing the equilibrium conversion of methane [17]. Uemiya et al. also reported very high methane conversion at lower temperature using this type of reactor [20].

In addition to produce high purity H_2, the following steps need to be carried out.

2.1.2.2 Water gas shift reaction

Fuel cells can use hydrogen feed stream with different purities depending on the type and future application of fuel cell. As a case in point high-temperature fuel cells admit high concentration of CO or/and CO_2 in the feed flow whereas, for low-temperature fuel cells, CO adsorbs irreversibly on the surface of electrode catalysts blocking the reaction sites for hydrogen [21]. Because of this and with the goal of increasing hydrogen selectivity, CO coming from methane steam reforming can be transformed in CO_2 and H_2 through the water-gas shift reaction [13].

It is an historical and industrial important reaction which reached a large development in 1960 when one catalyst of copper and zinc was discovered for low temperature shift reaction. Since then, the water gas shift reaction has been performed mainly to generate hydrogen for processes like ammonia synthesis or hydro treating of petroleum stocks. Nowadays, it is being used mainly for fuel cells in steam reforming as it was declared above. The development is focused on searching for catalyst characterization, kinetic and reactor modeling. [5] The exothermic reaction describes the conversion of carbon monoxide and steam to carbon dioxide and hydrogen and the involved enthalpy is ΔH_r = -41.1 kJ/mol [22].

$$CO + H_2O \leftrightarrow CO_2 + H_2$$ **Reaction 2.2**

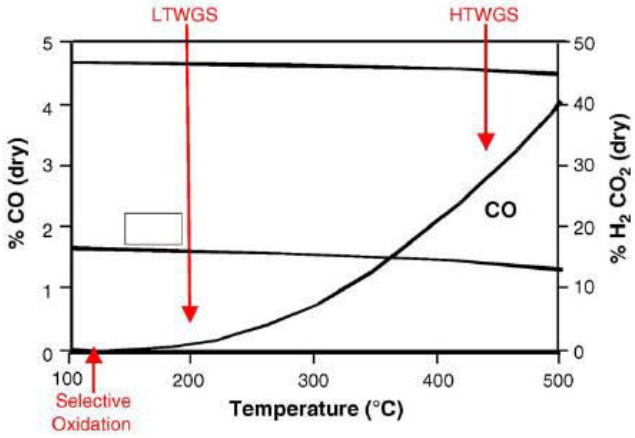

Figure 2.3. WGSR progress as function of temperature [23]

The notable temperature dependency makes that the equilibrium constant decreases with a temperature rise which means that at lower temperatures (Figure 2.3) it is noticed a higher carbon monoxide conversion. Thus, WGSR is inhibited at high temperatures and, besides, it is slow compared to other hydrocarbon reactions what gives room to a reactor with large dimensions, usually the biggest element in this type of processes. To accomplish a reactor size reduction is a fundamental matter[5].

Nevertheless, the higher temperature, the higher reaction rates so, in order to take advantage of both the thermodynamics and kinetics of the reaction, WGSR is executed in multiple adiabatic steps involving a high temperature shift (HTWGS) followed by a low temperature shift (LTWGS) with intersystem cooling. Different catalysts are required in each stage because of diverse operation conditions.

- ***High temperature WGS (HTWGS)***

In a typical operation, gas comes from reformer at approximately 350-450°C. Next, HTWGS also occurs within a temperature range between 310-450 °C . The incoming temperature is maintained to prevent a very high exit temperature since this rises during the length of reactor due to its exothermic nature. Typical pressure condition is a range from atmospheric to 8375 kPa.

HTWGS initial step is favored by high reaction rates, but it is thermodynamically restricted so carbon monoxide conversion is incomplete and, about 3-4% CO concentration still remains in exit stream [23].

The most commonly used and commercial HTWGS catalyst is the iron oxide-chromium oxide. Its use has been recognized owing to its advantages such as low cost, long life and reasonable resistance to sulphur though the restraint is its deactivity below 350 °C [23]. Iron oxides are in charge of material catalysis and the chromium acts to stabilize iron oxide and prevents sintering.

- ***Low temperature WGS (LTWGS)***

A consecutive low temperature shift reaction is performed to produce a CO exit concentration of less than 1% and to achieve hydrogen production. LTWGS reactor operates at a range of 200 to 250 °C. The typical LTWGS catalyst is a copper-based catalyst but its temperature stability is poor above 300 °C and it tends to poisoning by sulfur and thermal sintering. Copper-based catalysts are usually combined with ZnO, which provides structural support and prevents sulfur poisoning, and with Al_2O_3 which prevents dispersion. It is important to operate at low temperatures to preserve the activity and to prevent side reactions.

2.1.2.3 Disadvantages of steam reforming

Nowadays, concerning the effort to minimize CO_2 emissions, the search of alternative methods to replace fossil fuels for hydrogen generation is the main focus of renewable energy sources development. Mainly, taking into account that most of H_2 production technologies exhibit a high penalty of energy giving rise to an efficiency loss and a price rise [11], ex: Figure 2.5 represents the long chain of steps that steam reforming network entails, including steam reforming and water-gas shift reaction, in order to achieve a reasonable hydrogen conversion and high hydrogen stream purity.

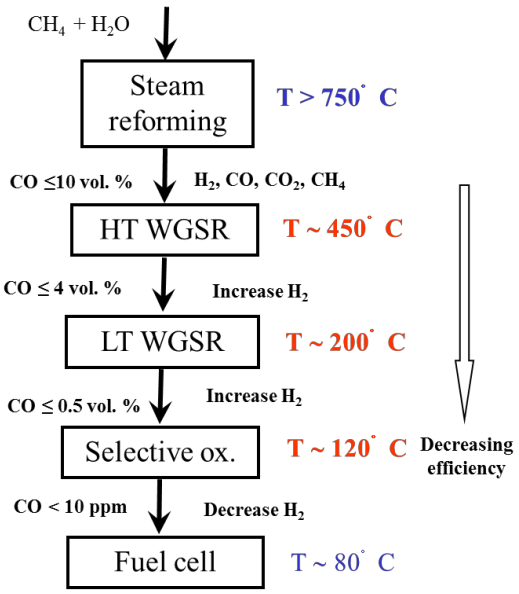

Figure 2.4. Hydrogen production network [23]

Among different alternatives proposed during the last years, Chemical looping process has gained special attention. This emerging technology is able to collaborate in a wide range of applications such as fuels, chemicals and electricity productions in addition to reducing carbon dioxide emission[4].

2.2 MAIN FUNDAMENTALS OF CHEMICAL LOOPING PROCESS

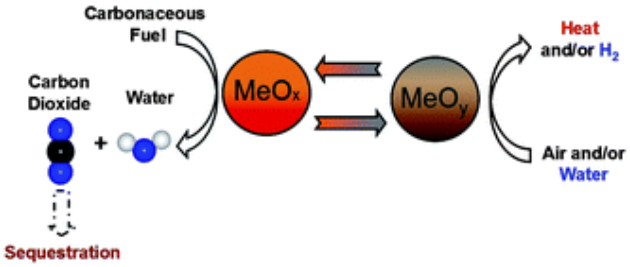

Figure 2.5 Chemical looping process basis

Chemical looping is a process based on redox cycles (Figure 2.5) through an oxygen carrier which is reduced and reoxidized, respectively, transporting the required oxygen to convert a specific fuel. The oxygen carrier is commonly a transition metal oxide (MeO) which is reduced by a fuel gas producing CO_2 and/or H_2O and, subsequently, it is reoxidized by means of air or steam/carbon dioxide generating heat or CO/H_2.

In a normal chemical looping unit, the solid material (metal oxide, MeO) is circulated between two reactors: the reducer and oxidizer [4]. Diverse reducing agents like hydrogen, methane and syngas can be chosen and, among oxidizing agents, air, CO_2 and H_2O are the most frequently employed. Furthermore, other studies have considered the option of metal thermal reduction applying concentrated solar energy and providing oxygen[24]. Depending on the gas employed in the oxidation step the chemical looping can be broadly be classified into the following categories:

Chemical looping combustion (CLC): Air is used to regenerate the oxygen storage material. It basically consists of carbonaceous conversion into heat following the operation scheme described above. [1], [4].

Reactions performed during CLC are described in what follows as well as a process scheme that consists of two interconnected reactors[25]:

$$(2n+m)Me_xO_y + C_nH_{2m} \rightarrow (2n+m)Me_xO_{y-1} + mH_2O + nCO_2 \qquad \textbf{Reaction 2.3}$$

$$2Me_xO_{y-1} + O_2(g) \rightarrow 2Me_xO_y \qquad \textbf{Reaction 2.4}$$

On the other hand, for high purity hydrogen production, the regeneration of oxygen carrier must be performed by using H_2O, obtaining a hydrogen stream as product. This type is called **Chemical looping steam reforming (CLSR)** [4]**.** A separate stream of pure and easily sequestered CO_2 can be also formed if the reducing agent is any syngas. The wide typical range of operation temperatures is 500-1000°C [9] depending on the reactants and solid material. [4]:

$$(2n+m)Me_xO_{y-1} + (2n+m)H_2O \rightarrow (2n+m)Me_xO_y + (2n+m)H_2 \qquad \textbf{Reaction 2.5}$$

Another kind of chemical looping process whose name is **Chemical Looping dry reforming (CLDR) or Chemical Looping CO_2 conversion** produces synthesis gas (mainly CO) which can be employed in other chemical processes. The oxidizing agent is CO_2 and the typical operating conditions are 700-900 °C [11]. Unlike the target of traditional dry reforming, CLDR is optimized for CO_2 activation with the goal of maximum CO yield and no selectivity for H_2 over an oxygen storage material [7], [4], [26]:

$$(2n+m)Me_xO_{y-1} + (2n+m)CO_2 \rightarrow (2n+m)Me_xO_y + (2n+m)CO \qquad \textbf{Reaction 2.6}$$

For each type of Chemical Looping process according to the application, it is totally crucial to find the best oxygen carrier material taking into account different operation conditions.

2.3 OXYGEN CARRIERS

2.3.1 Characteristics [1]

A key issue in the system performance is the selection of an appropriate oxygen carrier material. Among the characteristics taken into account to choose the carrier with criterion, it is found: its limited cost, some environmental aspects, the reactivity of the oxygen storage material, thermal stability, resistance to attrition, negligible carbon deposition, no agglomeration.

Oxygen storage capacity and favourable thermodynamics depend on the redox system because though oxidation reaction is always exothermic, the reduction reaction depends on the system redox, it is sometimes exothermic (H_2 or CO) and other times endothermic (with CH_4).

Besides, the pure metal oxides do not fulfil normally the characteristics and reaction rates so it is necessary a porous support to provide a higher surface area for reaction. Thus, the method used in the preparation of the materials strongly also affects the properties of the oxygen-carrier.

The economic cost, includes three important factors: cost of the metal oxide, the inert, and the manufacturing cost. Cobalt and nickel are the more expensive metals, followed by copper. Manganese and iron exhibit the lowest prices.

Oxygen carriers based on nickel and cobalt derived compounds have carcinogenic properties, hence toxic to the environment. Hence environmentally friendly materials, iron and manganese which are considered as non-toxic materials can be applied towards Chemical Looping applications

It has also to take into account the attrition behaviour of solids (in fluidized fuel reactors), the particles agglomeration due to the fact that it could cause solids circulation disturbances and channeling and carbon deposition on the oxygen-carrier particles since it reduces the efficiency of the CO_2 capture.

2.3.2 Oxygen carrier materials

Many efforts have been made to develop oxygen-carriers suitable for the different processes. Most of the oxygen-carriers proposed in the literature are synthetic materials. The active metal oxides (CuO, Fe_2O_3, NiO, Mn_3O_4 or CoO) are supported on different inert materials such as Al_2O_3, $MgAl_2O_4$, SiO_2, TiO_2, ZrO_2 [1].

The most important oxygen-carriers are [1]:

- ***Ni-based oxygen-carriers:*** high reactivity, good performance at high temperatures (900-1100 ºC) but more expensive (solution: particles with low nickel content) and toxic (safety measures). Pure NiO has low reaction rate (due to low porosity) so some improvements can be done like using support material or different preparation methods. Alumina (Al_2O_3) based compounds as support material is a good option because they show very high reactivity with fuel gases, no agglomeration problems, low attrition rates and avoidance of carbon deposition but the problem is the partial transformation of NiO into $NiAl_2O_4$ spinel compound.

- ***Cu-based oxygen-carriers:*** non-hazardous, cheaper, high reaction rates and oxygen transfer capacity and no thermodynamic restrictions. In particular, CuO has been investigated because of its high reactivity. However, the oxidation rate decreases with the number of cycles rise so to improve CuO performance, a number of Cu-based materials have been prepared using different compounds as support materials and different preparation methods. In spite of Cu-based materials have exhibited very high reactivity, they exhibit agglomeration problems due to the low melting point of Cu (1085 ºC). Therefore, Cu-based materials are good oxygen-carriers at temperatures lower than 800 ºC but higher temperatures would be preferred to obtain a better efficiency in the process.

- ***Mn-based oxygen-carriers:*** non-toxic and cheap material, higher oxygen transport capacity. Particles of pure manganese oxide show low reactivity. To improve its performance, ZrO_2 is used to stabilize the compound achieving a good reactivity and stability.

- ***Co-based oxygen-carriers:*** low economic and environmental feasibility but high transport capacity. Although several oxidation states can be involved in redox reactions, Cobalt oxide is not suitable as oxygen carrier due to low thermal stability of Co_3O_4.

- ***Fe-based oxygen-carriers:*** low cost, abundant availability, environmental compatibility (not toxic), no risk of sulphide or sulphate formation in Chemical Looping Combustion and overall favourable

thermodynamics [9]. Different oxidation states (Fe_3O_4, FeO, Fe) are detected when Fe_2O_3 is reduced (Fe_2O_3 => Fe_3O_4 => FeO => Fe), but Fe_3O_4 is thermodynamically unable to oxidize by CO_2 and H_2O, only using air (O_2) as oxidizing agent. Other problems have also been found, iron oxides with high surface area rapidly deactivate due to material sintering. To eliminate sintering problems, ferrites can be deposited on porous supports like Al_2O_3, TiO_2, $MgAl_2O_4$, SiO_2, ZrO_2, CeO_2 or $CeZrO_2$.

In general, Fe-based materials exhibited good reactivities, especially with CO and H_2. Fe-based oxygen carriers with small addition of Ni-based particles has been proposed by Juan Adanez et al. to be useful for Chemical Looping for hydrogen production.

- **Chemical looping dry and steam reforming**

Focusing on chemical looping reforming processes, reactivity is the strongest criterion because the reactivity of CO_2 and H_2O as oxidizers is lower than air. After a thermodynamic analysis to identify suitable metals, it was concluded that a great deal of transition metals can be oxidized by CO_2 but many of them present some restrictions such as equilibrium conversion for reduction depending on the fuel and required temperatures close to melting points [26]. Some metals give reasonable CO_2 reduction capacity to CO, however, among these, **iron** shows the widest operating temperatures range along with high oxygen storage capacity (for two moles of Fe, there are three moles of oxygen). Comparing thermodynamically specific oxides of Ni, Cu, Co and Mn, Fe_2O_3 shows the most promising conversion of CO and H_2 to CO_2 and H_2O, according to Victoria J. Aston [9]. Moreover, a higher conversion of H_2O to H_2 is obtained by oxidation of Fe and FeO to Fe_3O_4 [9]. Fe_3O_4 cannot split water to regenerate Fe_2O_3 without O_2 oxidation since Fe_3O_4 is thermodynamically unable to oxidize much of the CO and H_2 in syngas to CO_2 and H_2O, leaving part un reacted syngas.

The commonly performed reactions using Fe-based materials are:

$$3Fe_2O_3 + 9H_2/CO \leftrightarrow 6Fe + 9H_2O/CO_2 \qquad \textbf{Reaction 2.7}$$

$$6Fe + 8H_2O \leftrightarrow 2Fe_3O_4 + 8H_2 \qquad \textbf{Reaction 2.8}$$

$$2Fe_3O_4 + \frac{1}{2}O_2 \leftrightarrow 3Fe_2O_3 \qquad \textbf{Reaction 2.9}$$

2.3.3 Bifunctional materials

A bifunctional material is a novel material widely employed in chemical looping reforming process which apart from taking part in the redox process, i.e. reduction and oxidation, it improves reaction characteristics providing some essential qualities to the material such as sintering prevention and good material dispersion with support addition and better activity and stability in addition to fuel conversion to reducing agent over a catalyst addition [7]. In short, through a bifunctional material, three steps take place: a first catalyst step where fuel is split, a reduction process and an oxidation process, returning to its initial phase.

Hence, it is clear that the intrinsic properties of a metal oxide can be altered by changing or doping with additional metallic constituents in order to fulfill better properties. As a matter of fact, in the past decades, nanosized spinel ferrite particles have gained more attention. They have been investigated in a great deal of fields like ferrofluids, magnetic refrigeration systems, microwave industries. It is recognized that spinel ferrites (binary and ternary) are successfully used as catalysts for industrial processes such as Fischer-Tropsch reaction, hydrodesulfurization of crude petroleum, decomposition alcohols etc. [27]

2.3.3.1 Structure

The general formula of a spinel is $Me^{2+}Me_2^{+3}O_4$ and they present three ways of distribution [27]:

- Normal: divalent metal ions placed on tetrahedral A-sites $(Me^{2+})_A\ [Me_2^{+3}]_B\ O_4$
- Inverse: divalent metal ions located on octahedral B-sites $(Me^{3+})_A\ [Me^{2+}Me^{+3}]_B\ O_4$
- Intermediate or partially inverse: between normal and inverse $(Me_x^{2+}Me_\lambda^{3+})_A\ [Me_{1-x}^{2+}Me_{2-\lambda}^{+3}]_B\ O_4$

In the particular case of Fe, Fe^{3+} cations can occupy both A or B sites depending on the stoichiometric ratio. Thus, the distribution in spinel structure influences physically and chemically material so its determination is considerable to study the properties [27].

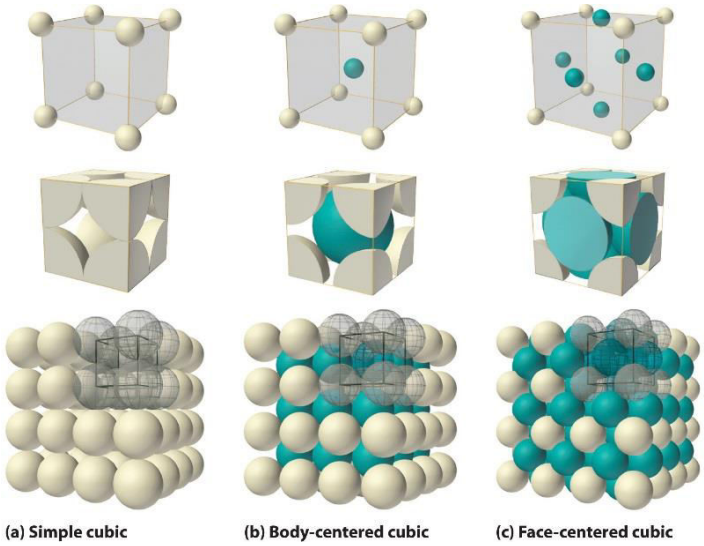

Figure 2.6. Lattice structure distribution

2.3.3.2 Modified iron oxides

Iron is suggested for hydrogen production at relatively high temperatures but redox cycles in that case induce structural changes, agglomeration, sintering and deactivation of iron. For this reason, a metal/metal oxide, a catalyst and a convenient support are some requisites to work at lower temperatures with high reactivity of solid reactants [28]. In particular, bifunctional materials are mostly utilized so as to increase the reactivity of particles, to improve the conversion of the fuel gas, to decrease the attrition and carbon deposition, to reduce the preparation cost and to minimize toxic metals [1].

Another important restraint of iron is the possibility of soot, Fe_3C and $FeCO_3$ formation in the reduction process by CO and CO_2 leading to hydrogen with carbon impurities production [28]. Therefore, looking for convenient conditions for a thermodynamically easier reduction step and to decrease carbide and carbonate formation tendency, some transitional metal are commonly employed. Cu, Co and Ni are the most sustainable for Chemical Looping.

Nevertheless, the main restraint of copper is that its operating temperature is limited due to the low melting point of metallic Cu (1063 -1085°C). Thus, several studies eliminated Cu as potential oxygen carrier owing to agglomeration problems [29]. Hence, Ni and Co have been chosen for cyclic hydrogen production in Chemical looping.

The mixed metal spinels $NiFe_2O_4$ and $CoFe_2O_4$ have the composition AB_2O_4. The alone magnetite Fe_3O_4 contains one Fe^{2+} ion for two Fe^{3+} ions whereas, in the mixed, all the Fe ions are Fe^{3+} and Ni and Co present

a 2+ charge [9]. A higher conversion of H_2 and CO_2 during mixed metal ferrite reduction than through Fe_3O_4 along with a mixed metal spinel regeneration after oxidation unlike Fe_2O_3 case were showed by Karel Svodoba et al. [28] . Special consideration should be given to the possible segregation upon cycling to Fe_3O_4, NiO, and CoO instead of cycling back to $NiFe_2O_4$ and $CoFe_2O_4$ spinel. Hydrogen yield will be higher in mixed metal ferrites because Fe^{2+} to Fe^{3+} oxidation gives rise to an additional H_2 production [9]. In fact, according to Jonathan R. Scheffe et al. $CoFe_2O_4$ generate twice the amount of hydrogen as Fe_2O_3 under the same conditions, probably, since the ability of Co^{2+} to cycle between metallic state and 2+ oxidation state. Furthermore, this study reported that the cyclability was maintained for up to 7 cycles [30].

In addition, a driving force is necessary so as to methanol and ethanol decomposition takes place. This is explained in a below section. Both cobalt and nickel are capable of provoking methanol decomposition. Besides, they are cheap and widely used in the industry, especially Ni. Furthermore, both can work at high temperatures (900-1100 °C). However, according to Kodama and Gokon, hydrogen production during first cycle is higher using Cobalt than nickel. On the other hand, considering average yield at the same reducing temperature, it is concluded that nickel is more promising [31].

2.3.3.3 Modified ferrites

Therefore, chemical looping process relies strongly on the material activity. As stated above, the main challenge is to select an appropriate oxygen carrier which maintains its activity and stability in repeated reduction and reoxidation cycles and iron oxides prove to be the best option for thesis aim but, it is well-known that these particles with high surface area rapidly deactivate due to material sintering and coke formation [4], [7]. Hence, redox support materials are commonly utilized to prevent catalyst deactivation. Among different supports like SiO_2, Al_2O_3, MgO, $MgAl_2O_4$, CeO_2 and $CeZrO_2$ [11], cerium oxide stands out as promoter owing to characteristics such as high activity in methane or syngas oxidation by lattice oxygen and improvement of metal catalyst dispersion. In addition, its redox couple (Ce^{4+}/Ce^{3+}) facilitates surface deposited coke gasification by storing and transferring active oxygen [4][7]. Thus, this promoter brings out structural modification and stabilization of iron oxides what makes it an ideal support material for hydrogen production chemical looping. Besides, it has been demonstrated an improvement in reducibility at lower temperatures with the creation of a solid solution between transition metal oxide and cerium oxide [4]. Finally, Zirconium enhances the surface area, thermal stability and oxygen storage capacity of material if it is introduced in the ceria lattice structure [32].

To sum up, CeO_2 was chosen due to its redox properties, taking part in the reaction and acting as a physical barrier and Zr was introduced to improve thermal stability of Ce.

2.3.4 Chemical looping reforming process

Chemical looping reforming process for H_2 production and CO_2 conversion from methanol and ethanol as reducing agents through $CoFe_2O_4$ and $NiFe_2O_4$ are based on three steps: firstly, biofuel must be decomposed in syngas over a catalyst, secondly spinel is reduced with the organic feed fuel whose products are CO, CO_2, H_2O and H_2 and, finally, reoxidation to initial state of material. In fact, in general, iron-based oxides of Co-, Cu, Ni-, Zn- ferrites, also with ceria and zirconia as support, are good candidates for the decomposition [22]. Stefano Cocchi et al. considered that $CoFe_2O_4$ presents great interest because of its higher reducibility and, consequently, lower reduction temperature and, also, E. Manova et al. studied the changes in redox properties of iron and mixed iron cobalt oxides in methanol decomposition [22], [27].

On the other hand, Nickel catalysts have also proved to be active for decomposition. Specific surface area of metal depends on the content and crystallite size of nickel, for that reason, they are key factors to control. For instance, the investigation of Yasuyuki Matsumura et al. showed that small nickel particles (2-4 nm) are less active than large ones what means that decomposition is promoted on well-crystallized Ni particles [33].

2.3.4.1 Methanol and ethanol steam reforming

According to conventional networks in which bioalcohols are usually employed and referring to Section 2.2.2.1. Methanol and ethanol can be used as feed fuels in hydrogen production by steam reforming process. Both reactions are endothermic, ΔH_r=131 kJ/mol for methanol [2] and ΔH_r= 238 kJ/mol for ethanol [34].

$$CH_3OH + H_2O \rightarrow CO_2 + 3H_2$$ **Reaction 2.10**

$$CH_3CH_2OH + 3H_2O \rightarrow 2CO_2 + 6H_2$$ **Reaction 2.11**

Methanol is a bulk chemical generated in large quantities and it can be produced from renewable feedstocks avoiding anthropogenic carbon dioxide emission to the atmosphere. Among its characteristics, it stands out its easy conversion at low temperatures (200-300 °C), high hydrogen-to-carbon ratio, it does

not possess carbon-carbon bond what makes it a energetically favourable process and prevents soot formation. [2]

On the other hand, the very attractive qualities of ethanol are its availability, handling safety, storage, moderately high hydrogen content and its renewable production from some biomass sources such as waste materials from agroindustries, organic fraction of municipal solid waste, energy plants, forestry residue materials, etc. [34], higher energy content and lower toxic level than methanol [2].

The steam reforming of these alcohols can be influenced by a great deal of undesirable factors, mainly, disliked side reactions. Therefore, to achieve a high yield of pure hydrogen, some variables have to be studied and adjusted such as temperature, pressure and reactants ratio. Because of this, first of all, it is to analyse the effect of these variables on product stream investigating the thermodynamics. Some studies have performed a thermodynamic analysis of the process and have concluded that the steam reforming of methanol and ethanol is totally attainable [3] [35]. For instance, concerning ethanol, the following statements guide to high purity hydrogen and syngas: low pressure, higher water/ethanol ratio and high temperatures [35][36].

The main difficulty is to find a catalyst which presents high stability and activity for steam reforming, resists to coke formation and, above all, leads to high yield of H_2. In the case of ethanol steam reforming, a few studies described the performance of a diversity of catalysts like Ni, Co, Cu and noble materials like Rh, Pd and Pt. To cite an instance, Dimitris K. Liguras et al. reported that both supported Ni catalysts and supported Rh catalyst present high activity, stability and selectivity under selected experimental conditions leading to hydrogen-rich process gas production [34]. However for methanol case, Copper-based catalysts are almost the most frequently material utilized for methanol steam reforming. B. Lindström et al. studied the reforming of methanol over various copper-based catalysts testing with different promoters such as chromium, zinc and zirconia and with aluminum oxide as support. The conclusion was that hydrogen yield increases if the content of Cu is higher and chromium promotes catalyst activity preventing the formation of agglomerates. [2]

2.3.4.2 Methanol decomposition

Methanol decomposition is a convenient process to obtain syngas for reduction reaction. To carry out the reduction process, a reducing agent like hydrogen and methane is necessary. Methanol has been become one of the most appropriate liquid energy carriers because of its synthesis from plentiful sources and its high hydrogen-to-carbon atomic ratio. The main objective concerning this thesis is to obtain high purity hydrogen or high purity of carbon monoxide so by means of methanol decomposition, it is produced syngas, i.e. hydrogen and carbon monoxide, which can be allocated for chemical processes or used as fuel for fuel cells, vehicles and gas turbines [27].

- ***Reaction***

Methanol conversion to hydrogen and carbon monoxide is an endothermic process with a 90.7 kJ/mol heat of reaction [37]. Therefore, a heat contribution is necessary to reach required temperature and to maintain the reaction. Furthermore, it is necessary a catalyst so that reaction takes place.

$$CH_3OH \rightarrow CO + 2H_2$$ **Reaction 2.12**

In consequence, methanol decomposition depends on temperature as it is showed in studies reported by E. Manova et al. and Yasuyuki Matsumura et al. [27], [33] Temperature range in which methanol decomposition is achieved is, approximately, between 250-450 °C.

- ***Reaction conditions***

As objection, carbon monoxide generated is an atmospheric pollutant, poisonous for fuel cells and harmful to health so another process must be done before using hydrogen product stream for fuel cells. Moreover, the reaction can give rise to undesired by-products like di-methyl-ether and methane. Both issues depend on the reaction conditions and catalyst choice [38].

Catalysts that work at low temperatures with high selectivity to H_2 and CO and good activity are necessary to apply methanol decomposition as hydrogen source for applications like vehicles and fuel cells [39].

- ***Methanol as feed gas in CLP***

Chemical looping process consists of three steps if methanol is used as feed gas. Before taking place the reduction, bioalcohol is decomposed through a catalyst, as stated above in the bifunctional material explanation. CO and H_2, i.e. syngas, are the products from the reaction and they are charge of carrying out reduction of the oxygen storage material. Next, bifunctional material is regenerated by mean of a oxidation process upon H_2O or CO_2 leading to H_2 and CO generation. Reactions performed are the following:

1. **Catalytic Step** $CH_3OH \rightarrow CO + 2H_2$ **Reaction 2.13**

2.	**Reduction Step**	$Fe_3O_4 + CO + H_2 \rightarrow Fe + CO_2 + H_2O$	**Reaction 2.14**
3.	**Oxidation Step**	$Fe + CO_2/H_2O \rightarrow Fe_3O_4 + CO/H_2$	**Reaction 2.15**

2.3.4.3 Ethanol decomposition

Ethanol is a very important energy carrier and it can be also utilized as feed fuel gas in Chemical Looping steam and dry reforming. This bioalcohol has potential as hydrogen carrier for fuel cell applications. Thermal decomposition of ethanol strongly depends on the pressure[40] and it takes place at high temperatures.

- ***Reaction***

The dominant decomposition reaction is showed at Reaction 2.16. When ethanol is decomposed, it gives rise to some products which can be employed as reducers in Chemical Looping process in order to produce high purity hydrogen or carbon monoxide relying on the chosen oxidizing agent.

$$C_2H_5OH \rightarrow CH_4 + CO + H_2 \qquad \textbf{Reaction 2.16}$$

- ***Reaction conditions***

Unlike methanol decomposition, ethanol exhibits an important restraint: It forms methane in its decomposition. As section 2.1.2.1. encloses, methane needs high temperatures to decompose, to carry out this second decomposition a third functional compound would be necessary so it would be a trifunctional material. For that reason, in this investigation, methane has not been decomposed working with some bifunctional materials.

- ***Ethanol as feed gas in CLP***

Ethanol Chemical Looping reforming process is also performed in three steps (one is subdivided in two).

1.	**Catalytic Step**	$C_2H_5OH \rightarrow CH_4 + CO + H_2$	**Reaction 2.17**
2.a.	**Reduction Step**	$CH_4 + Fe_3O_4 \rightarrow CO_2 + 2H_2O + Fe$	**Reaction 2.18**
2.b.		$Fe_3O_4 + CO + H_2 \rightarrow 3Fe + CO_2 + H_2O$	**Reaction 2.19**
3.	**Oxidation Step**	$3Fe + 4CO_2/4H_2O \rightarrow Fe_3O_4 + 4CO/4H_2$	**Reaction 2.20**

2.3.5 Material synthesis

Obviously, once it is known the importance of properties ferrites, it is necessary to carry out deeply some investigations on preparation procedures and characterization by various analytical techniques[41]. Various nanostructures of $CoFe_2O_4$ and $NiFe_2O_4$ have been successfully fabricated by the following methods: hydrothermal method, chemical co-precipitation, thermal decomposition, sol-gel method, pulsed laser deposition, electrodeposition, microemulsion, combustion and electrospinning [42].

The selection of an appropriate synthetic procedure often depends on the desired properties and the final applications. The following is a more detailed explanation of some of these methods, focusing on chemical co-precipitation which is used for this specific experiment.

- ***Electrospinning:*** it represents a simple, effective and convenient method for preparing polymer fibers and ceramic fibers (ultrathin). In a typical procedure, a high electrical potential is applied between a droplet of a polymer solution and a grounded target. When the applied electric field gets over the surface tension of the droplet, a charged jet of polymer solution is ejected and its route is controlled by the electric field. The charged jet undergoes a stretching process resulting in the formation of many continuous fibers.

  Only a few studies have been reported on electrospinning of magnetic oxide nanofibers but, some novel metal oxide nanofibers have been successfully prepared by this process followed by calcination at high temperature. An interesting investigation on this topic is reported by Montana Sangmanee and Santi Maensiri 2009 [42]. Another study of $CoFe_2O_4$ nanostructures and their variation of magnetic properties with calcination temperature was reported by Zhongli Wang et al. 2008 [43].

- ***Microwave combustion:*** it is one of the most effective, simple and feasible method for the rapid synthesis with high purity, homogeneity and improved characteristics of the nanomaterials. The procedure consists of the microwave energy transformation into heat energy by strong intermolecular friction and rises the precursor materials temperature suddenly. Other significant advantages are its adequacy for the preparation of large quantities of products without the need of higher temperatures for calcination, energy loss reduction, economical viability improvement and the chemical reaction and kinetics speeding up.

On the basis of some reported studies, an interesting investigation was carried out in order to try to improve the optical, magnetic and catalytic properties of spinel ferrites. The research attempts to identify the effects of Zn^{2+} doping and it was reported by E.Hema et al. 2015 [44].

- ***Sol-gel method:*** This synthesis route of the polymerized complex has been used to obtain especially nickel, nickel-zinc and strontium ferrites. It presents a better control in the stoichiometry of the products and, besides, it uses lower synthesis temperatures, shorter reaction times and gives better reproducibility.

  Two interesting studies are reported by Mathew George et al. 2006 [43] and by Sagrario M. Montemayor et al. 2007 [45] in which there is a comparison between $CoFe_2O_4$ and $NiFe_2O_4$ synthesis.

- ***Chemical co-precipitation:*** It consists of precipitating at the same time two metal compounds in aqueous solution which contains cation metal salt (nitrates). To get the precipitation, it is used a base which is added dropwise and which will be changing the pH until reaching a constant value. At this moment, the precipitation has been achieved with all cations in the same structure forming a spinel structure in this study case.

  Among all the synthesis methods, the **chemical co-precipitation method** is the most widely used for its simplicity, good control of crystallite size, free from contamination, lower cost and more homogeneous mixing of the components.

✓ LITERATURE SURVEY CONCLUSIONS

From the literature survey performed, Co and Ni ferrites show promising prospects as bifunctional materials in methanol and ethanol chemical looping. Their redox properties can further enhanced by modifying them with support materials such as $CeZrO_2$. A coprecipitation strategy would be adopted towards synthesis. These materials would be further tested for their activity and stability.

CHAPTER 3 MATERIALS AND METHODS

This main objective of this chapter is to describe procedures followed towards the synthesis (section 3.1) and testing of oxygen storage materials towards chemical looping (section 3.2).

3.1 MATERIAL SYNTHESIS

3.1.1 Synthesis strategy

Based on the literature survey (Chapter 2), co-precipitation method was adopted to synthesize modified iron ferrites as bifunctional materials in chemical looping. A batch of 5 grams for each sample was synthesized. The list of precursor materials used in synthesis is tabulated in Table 3.1, all of them were supplied by Sigma-Aldrich. The stoichiometric amount of precursor materials were weighed and mixed in a beaker with 400 ml of H_2O to form a solution. The solution was made homogeneous by constant stirring at 400 rpm at room temperature, once crystallites were dissolved, temperature was ramped to 70°C, while ammonium hydroxide solution was added dropwise. The onset of precipitation is characterized by change in the solution colour due to precipitate being formed. This process occurs at a pH between 10-11. Once the pH is attained the addition of base is stopped and the solution is stirred for 5 min in those conditions and then allowed to precipitate. pH control is a fundamental step to be followed during the co-precipitation. Samples with varying loadings (100, 80, 50, 20 wt% $CoFe_2O_4$/$NiFe_2O_4$-$CeZrO_2$) were synthesized.

Precursor	Molar weight (g/mol)	Function
$Fe(NO_3)_3{\cdot}9H_2O$	403.997	Novel material
$Co(NO_3)_2{\cdot}6H_2O$	291.035	Novel material
$Ni(NO_3)_2{\cdot}6H_2O$	290.79	Novel material
$ZrO(NO_3)_2{\cdot}xH_2O$	231	Support
$Ce(NO_3)_3{\cdot}6H_2O$	434.22	Support
NH_4OH	35.045	Driver precipitation

Table 3.1 – List of chemical precursors used in materials synthesis.

3.1.2 Post-treatment

After the procedure described in section 3.1.1, a post-treatment is performed on the samples. Firstly, obtained mixtures were vacuum filtered to separate desired precipitate from the solution (Figure 3.1.a). Secondly, this precipitate is dried overnight in an oven at 240 °C to eliminate water amount (Figure 3.1.b). After drying, samples were crushed using a pestle and mortar (Figure 3.1.c) and weighed to verify how much amount of material has been synthesized. Finally, resulting samples were calcined (Figure 3.1.d) at 650 °C for 6 hours from room temperature according to the following temperature program (Figure 3.2).

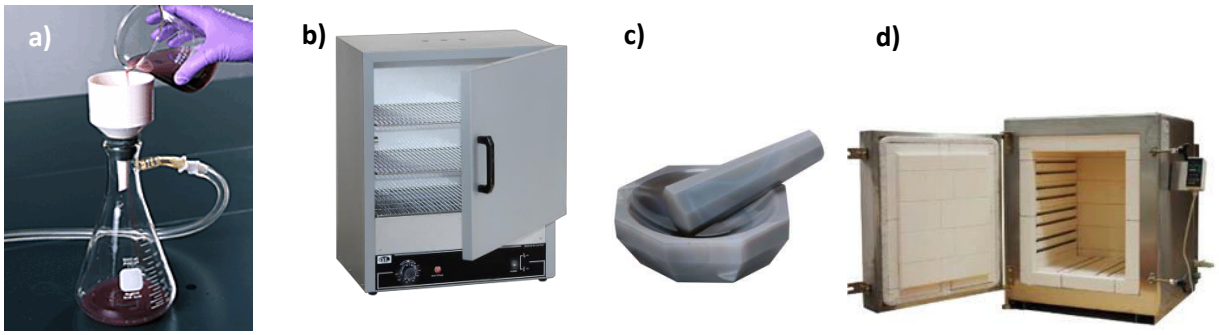

Figure 3.1. – Post-treatment devices:

a) Vacuum filtration, b) Drying oven, c) pestle and mortar, d) Calcination oven.

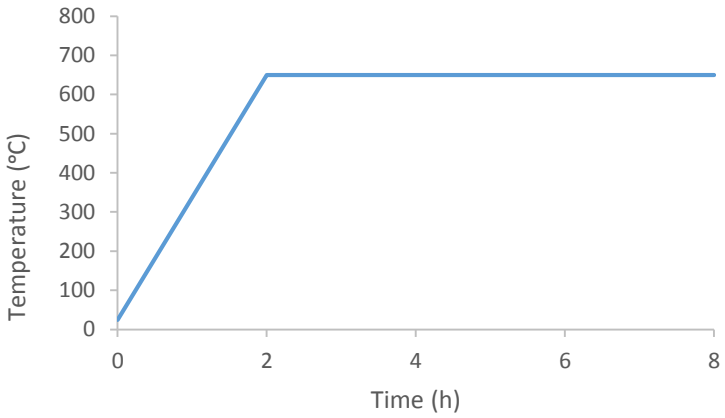

Figure 3.2. – Temperature program for calcination.

3.2 MATERIAL CHARACTERIZATION TECHNIQUES

The following experimental setups were used to characterize the samples and to analyze the physic-chemical properties.

- **XRD:** Siemens Kristalloflex D5000.
- **In-situ XRD**: Bruker Discover D8 (Vantec linear detector).
- **N_2- adsorption**: Micrometrics Tristar II 3020.
- **TPR / TPO**: Micromeritics Autochem II 2920.
- **Experimental reactor set-up**: Step response.
- **TEM**: JEOL JEM-2200FS.
- **EDX**: EDAX Genesis 4000.
- **ICP-AES**: Thermo Scientific iCAP 6500.

3.2.1 X-Ray Diffraction (XRD) analysis

XRD analysis is a non-destructive characterization tool used in materials science and solid state chemistry. Some basic concepts and the information derived from XRD are explained below.

A solid matter can be classified as [46]:

- Amorphous: atoms are arranged in a random way.
- Crystalline: periodic arrangement. In such a way that crystal is like a repetition of the smallest volume element in the structure called unit cell and whose dimensions (lattice parameters) are three axes (a,b,c) and the angles between them α, β, γ which can be determined by XRD.

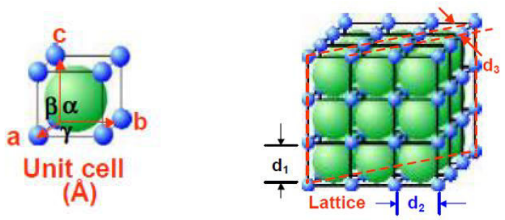

Figure 3.3. – Lattice structure of a crystal [52]

The structures of crystals and molecules are often being identified using X-Ray diffraction studies since its discovery in 1895. Each crystalline material always gives the same characteristic X-ray powder pattern

independently of the others in a mixture of substances, it is like a fingerprint used for its identification. Due to this property, XRD is mainly employed to determinate each compound in a sample and to characterize its structure.

- Information that can be obtained from powder x-ray diffraction are as follows [47]:
  - Lattice parameters
  - Phase identity
  - Phase purity
  - Crystallinity
  - Crystal structure
  - Percent phase composition

- **Operation**

In XRD, the sample is scattered with a monochromatic beam of X-rays photons (one wavelength by a filter or a crystal monochromator). When an X-Ray beam hits an atom, the electrons around it start to oscillate with the same frequency as the incoming beam. In almost all directions it will be found destructive interference (out of phase and no resultant energy leaving the solid sample). However, in a crystal, there will be constructive interference due to the regular pattern of their atoms so the waves will be in phase and X-Ray beams will leave the sample at various directions.

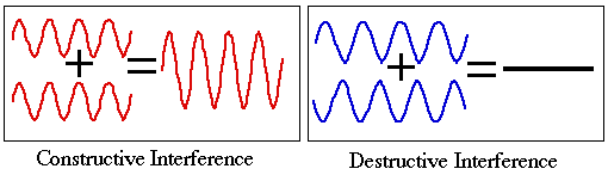

Figure 3.4. – Phase of Interferences

- **Beam production**

X-Rays are generated through a metal (Cu and Mo usually) by bombarding with a beam of high-speed electrons whose emission is produced from a hot filament (Tungsten as the most common material). When the beam impacts on the metal, electrons are ejected and drop from a lower level (1s) to an upper level (2p or 3p) filling the atom vacancies and giving rise to X-Rays emission. X-Ray source in XRD set-up was Cu metal whose K_α beam = 1.5418 Å

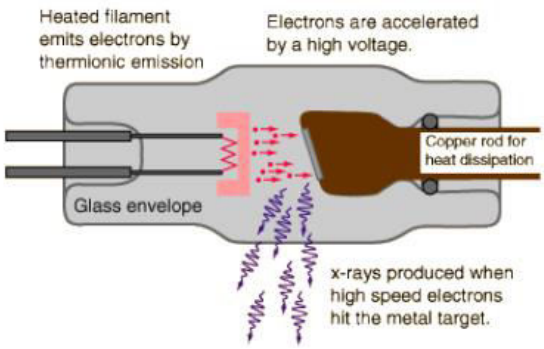

Figure 3.5. – X-Rays production device [47]

- ***Bragg's Law***

Diffraction is based on Bragg's Law. The law states that when the radiation is incident onto a crystal surface, its angle of incidence, θ, will reflect back with a same angle of scattering. And, when the path difference, d, is equal to a whole number, n, of wavelength (remaining in phase), the scattered waves interfere constructively. Therefore, Bragg's Law relates the lattice spacing and diffraction angle which, in turn, is a function of X-ray intensity.

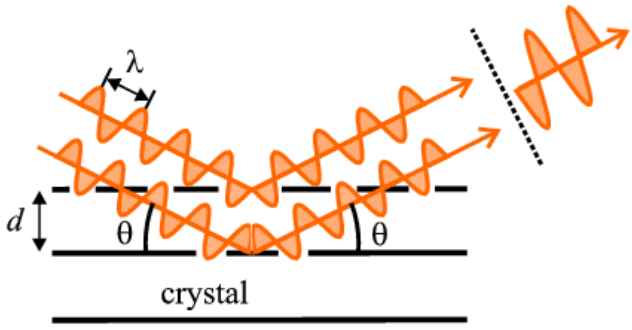

Figure 3.6. – Bragg´s Law

$$n\lambda = 2d\ sin\theta$$ **Equation 3.1**

Where:

- λ [nm] = wavelength of the x-ray
- d [nm] = spacing of the crystal layers (lattice space or path difference)
- θ [°C] = incident angle (the angle between incident ray and the scatter plane)
- n = a positive integer (order of reflection)

- ***Scherrer equation for crystallite size:***

The main disadvantage of XRD is its intensity dependency on the crystallite size. Crystallite size can be estimated by means of Scherrer equation calculation using full-width half maximum (FWHM) of each characteristic peak.

$$d = \frac{K\,\lambda}{(\beta - b)\cos\theta} \qquad \textbf{Equation 3.2}$$

Where:

- λ [nm] = wavelength of the x-ray.
- d [nm] = particle dimension (diameter).
- K = a dimensionless shape factor, with a value close to unity (constant).
- θ [°C] = Bragg angle.
- β [rad] = peak width at half the maximum intensity (FWHM).
- b [rad] = instrumental width

This equation is limited to nanoscale particles (no more than 0.1-0.2 µm) owing to the fact that a variety of factors can contribute to the width of a diffraction peak. For crystallite size calculation, it is necessary to correct β value obtained from the experiment peaks with a reference data base like the used in this master thesis, LaB_6 crystal reference.

Position (2θ)	Width (b)	Position (2θ)	Width (b)
21.354	0.250	63.267	0.299
30.395	0.242	67.603	0.330
37.464	0.245	71.803	0.340
43.534	0.256	75.907	0.363
48.993	0.266	79.931	0.353
54.029	0.278	83.920	0.392

Table 3.2 – Instrumental width (b) of LaB6 crystal.

3.2.2 In-situ X-Ray Diffraction analysis.

In-situ XRD can be utilized to examine crystallographic changes or solid-state reactions.[7] In the present study, crystallographic transformations in the sample during H_2-TPR, CO_2-TPO and isothermal cycling were followed in a Bruker-AXS D8 Discover (Cu K_α radiation of wavelength 0.154 nm), in situ XRD setup. The set up consisted of a homebuilt reaction chamber with a Kapton foil window to allow X-ray transmission and a linear Vantec detector covering 20^o with an angular resolution of approximately 0.1° in 2θ [11]. A collection time of 10 seconds was used during the experiment [7]. Approximately 10 mg of powder is spread on a single crystal Si wafer (1,1,1). No interaction between the Si wafer and catalyst sample was observed [11]. Prior to the start of experiment the chamber is degassed to a base pressure of 5 Pa by means of a rotation pump and purged with helium. A uniform ramp rate of 20 °C/min till a temperature of was used during H_2-TPR and CO_2-TPO studies. The isothermal cycling experiments were undertaken at 500 °C and 750 °C with alternating sequences of reduction and oxidation. All the gas flows were maintained at 33 Nml/sec and 10%H_2/He and CO_2 (100%) were employed for reduction and reoxidation. Full XRD scans (10° to 65° with a step of 0.02°) at room temperature is performed on as prepared samples at selected stages of experiments.

3.2.3 N_2-adsorption analysis. Brunauer–Emmett–Teller (BET)

BET analysis provides information on the sample specific surface area which is related to particle size, particle morphology, surface texturing and porosity [48]. This analysis technique is based on Brunauer–Emmett–Teller theory which explains physical adsorption of inert gas molecules (ex: Nitrogen) on a solid surface. Specific surface area of a material can be determined by calculating the amount of adsorbate corresponding to a monolayer on the surface at a given pressure. It is derived from van der Waals forces that are established between the adsorbent surface area of sample and adsorbate gas molecules. Surface area is determined by monolayer formation and the principle of capillary condensation is applied to detect the presence of pores, pore size distribution and pore volume. So not only BET surface area can be accomplished by this technique but also other useful information.

The basis of BET theory is an extension of Langmuir theory (monolayer adsorption) to multilayer adsorption on solid materials which is more realistic than the presupposition of monolayers.

Some assumptions are established [49]:

- Homogeneous surface
- No lateral interactions between molecules
- Uppermost layer is in equilibrium with vapor phase
- First layer: Heat of adsorption

  Higher layers: Heat of condensation
- At saturation pressure, the number of layers becomes infinite

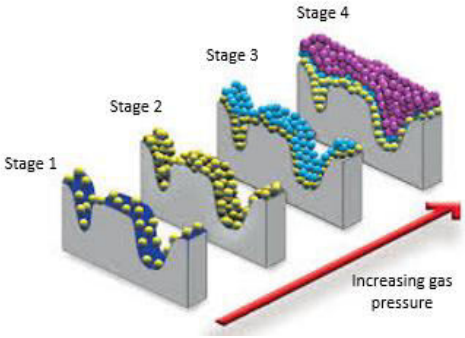

Figure 3.7. – Gas adsorption theory.

- Stage 1: Isolated sites on the surface begin to adsorb gas molecules at low pressure.
- Stage 2: Coverage of adsorbed molecules increases to form a monolayer with a gas pressure increase.
- Stage 3: Beginning of multi-layer coverage. Smaller pores fill first. BET to calculate specific surface area.
- Stage 4: Complete coverage. The BJH calculation to determine pore diameter, volume and distribution.

An adsorption isotherm is obtained by measuring the amount of gas adsorbed across a wide range of pressures at a fixed temperature (typically liquid N_2, 77 K) [50]. Conversely desorption isotherms are achieved by measuring gas removed as pressure is reduced. There are 6 types of isotherms presented on next Figure 3.8.

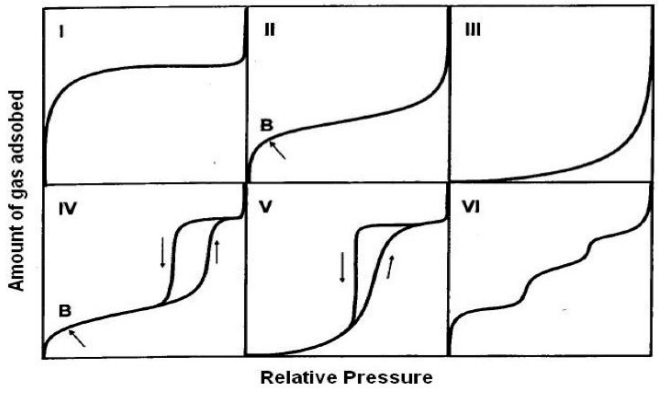

Figure 3.8. – Isotherms of adsorption [49].

- Type I: surface almost exclusively inside the pores. Once they are filled, there is no more external surface area or only a little bit.

- Type II: frequently nonporous powders or powders with diameters exceeding micropores.
- Type III: characterized by heats of adsorption lower than the adsorbate heat of liquefaction. Adsorption proceeds as the adsorbate interaction with an adsorbed layer is greater than the interaction with the adsorbent surface
- Type IV**:** porous adsorbents with pores in the range of 1.5 – 100nm. at higher pressures the slope shows increased uptake of adsorbate as pores become filled.
- Type V: small adsorbate-absorbent interaction and pores in the 1.5 – 100nm range
- Type VI: stepwise multilayer adsorption of on nanoporous non-uniform surface.

It is a cheap, fast and reliable method but it is not valid for all types of isotherms. Types II, IV and VI can be measured by BET but Types III and V present debilitated interactions between gas and adsorbent.

- ***CALCULATION*** [49]
  - At equilibrium:

$$a_i \cdot p \cdot s_{i-1} = b_i \cdot s_i \cdot e^{-E_i/RT} \qquad \textbf{Equation 3.3}$$

Where

- s_i = Surface area.
- p = Pressure.
- E_i = Heat of Adsorption.
- a,b = Constants.

  - Total surface area: $A = \sum_{i=0}^{\infty} s_i$
  - Total volume adsorbed: $V = V_o \sum_{i=0}^{\infty} i\, s_i$
  - Volume of gas adsorbed with totally covered surface: $V_m = V_o A$

From that point, Brunauer, Emmet and Teller derived the following equation:

$$\frac{V}{V_m} = \frac{c \cdot \frac{p}{p_o}}{(1-\frac{p}{p_o}) \cdot (1-\frac{p}{p_o}+c \cdot \frac{p}{p_o})} \qquad \textbf{Equation 3.4}$$

Where

- V [ml] = Volume of gas adsorbed at standard temperature and pressure (STP)(273.15 K and atmospheric pressure).
- V_m [ml] = Volume of gas adsorbed at STP to produce an apparent monolayer.
- p [Pa] = Partial pressure of adsorbate gas in equilibrium with the surface at 77.4 K (liquid nitrogen)
- p_o [Pa] = Saturated pressure of adsorbate gas.
- c = BET constant relating to the enthalpy of adsorption of the adsorbate on the sample.

By linear regression, Vm and c can be approximated so it is more convenient to write the equation as it follows [49]:

$$\frac{p}{V\cdot(p_o-p)} = \frac{1}{V_m\cdot c} + \frac{c-1}{V_m\cdot c}\cdot\frac{p}{p_o} \qquad \textbf{Equation 3.5}$$

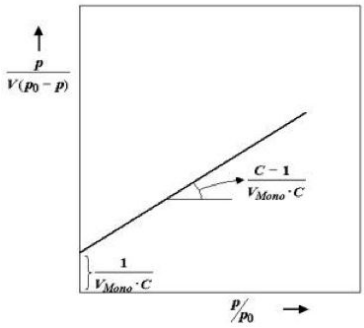

Figure 3.9. – Linear relationship

This linear relationship is only valid in the range of $0.05 < \frac{p}{p_o} < 0.35$

From V_m, BET specific surface area, S [m^2/g], can be calculated knowing the diameter of the sorbate:

$$S = \frac{V_m}{m}\cdot N_A \cdot \frac{1}{22400}\cdot a \qquad \textbf{Equation 3.6}$$

Where

- V_m [m^3] = Volume of gas adsorbed at STP to produce an apparent monolayer.
- m [g] = mass of sample
- N_A [mol^{-1}] = Avogadro constant (6.022 x 10^{23} mol^{-1}).
- a [m^2] = Effective cross-sectional area occupied by a singles adsorbate molecule (0.162 nm^2 for nitrogen).
- $^1/_{22400}$ [mol/m^3] = Concentration of adsorbate gas at STP.

Before carrying out the experiment, samples must be pretreated in order to remove all the other gases in the sample such as H_2O or CO_2 since the aim is to measure properties using N_2 adsorption. Hence, once samples are weighed and dried in the oven, they must be heated at 300 °C in the Smart-prep (Figure 3.10) overnight.

In the present investigation, Brunauer-Emmet-Teller surface area was determined by N_2 adsorption (five point BET method) using Micrometrics Tristar II 3020 (Figure 3.10.).

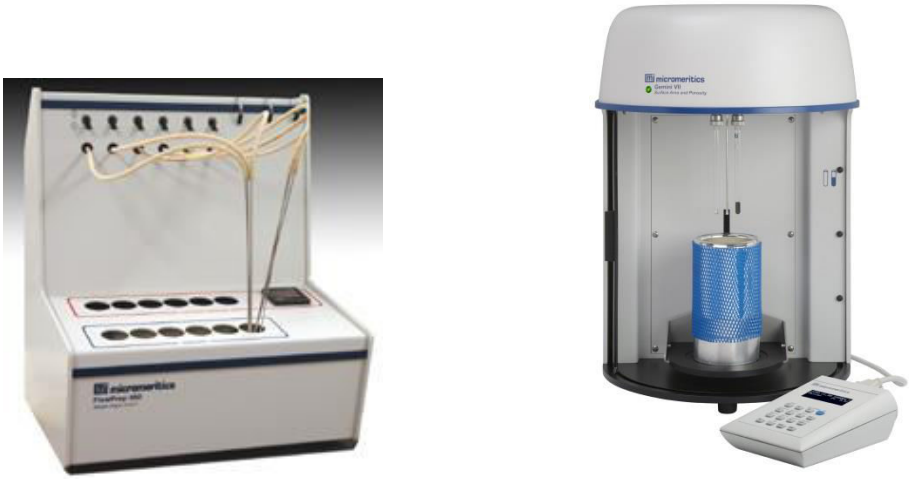

Figure 3.10. – a) Smart-prep and b) Micromeritics Gemini 2360 for BET measurements.

3.2.4 Temperature-Programmed Reduction and Oxidation (TPR/TPO)

Temperature-programmed reaction techniques are thermoanalytical techniques utilized to characterize chemical interactions between solid and gaseous substances. Among these analyses that can be performed, the most common tools for heterogeneous catalysts are: Temperature-programmed desorption (TPD), reduction (TPR) and oxidation (TPO). These material tests provide very useful information about redox properties of studied samples since it is possible to detect and follow physical or chemical transformations because of exchanges of matter and/or energy that occurred in the sample.

In this work, the H_2-TPR and CO_2-TPO experiments are carried out in a Micromeritics Autochem II 2920 setup. Micromeritics Autochem consists of an oven with a U shape quartz tube reactor inside. This reactor contains the sample arranged on the top of a quartz wool layer. Besides, there is a thermocouple measuring the temperature. Each sample was subjected to two cycles of H_2-TPR and CO_2-TPO to

investigate the redox properties. The samples were ramped from room temperature. Constant heating rate or temperature ramp in each test was 20 °C/min from room temperature until reaching 750 °C. The outlet gas compositions were monitored using a TCD detector. All the gas flows were maintained at 33 Nml/s. Results obtained from TPR and TPO by Autochem represent H_2 and CO_2 consumption (mol/s/kg material) as a function of time and temperature. Furthermore, the stability of materials was analysed by isothermal redox cycles alternating H_2 reduction, He purging, CO_2 oxidation and He purging again.

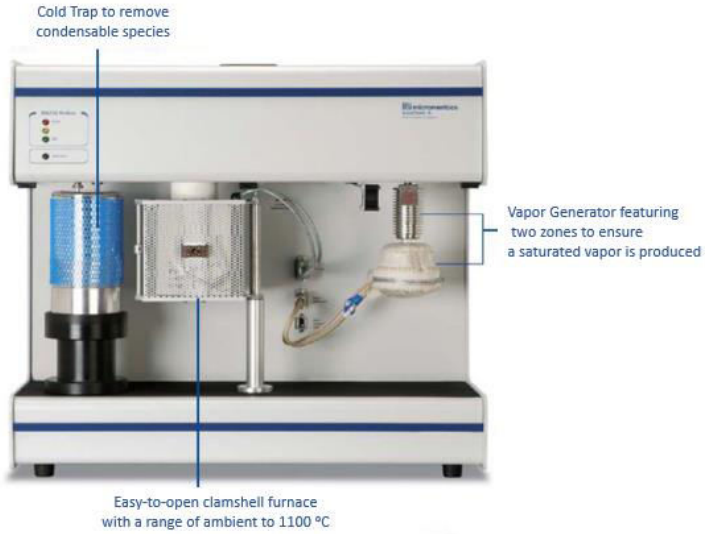

Figure 3.11. – Micromeritics Autochem II 2920 setup with a schematic representation of the reactor

Process that takes place between the sample and feed gas is represented in the following figure:

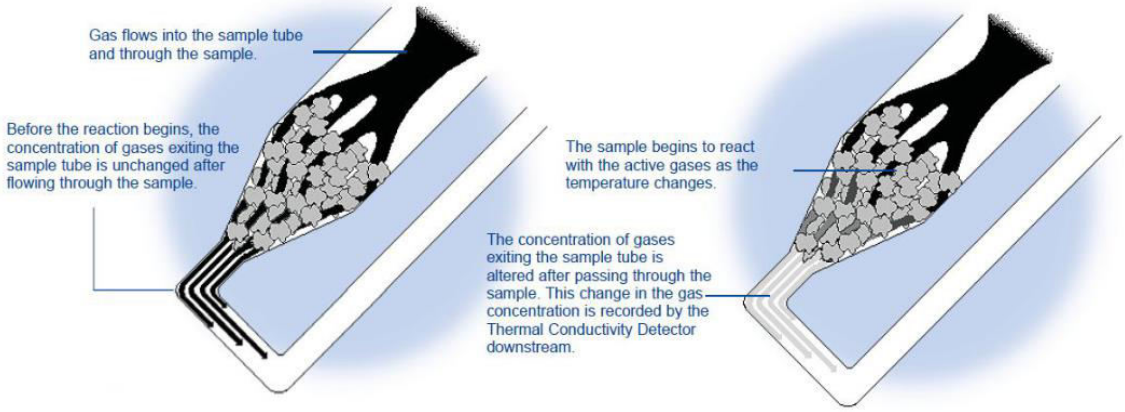

Figure 3.12. – Interaction solid-gas

3.2.5 Experimental reactor setup (Step response)

Figure 3.13. – Experimental reactor setup

Transient step-response experiments for both the reduction and reoxidation of modified iron oxides were carried out at atmospheric pressure in a quartz tube reactor (i.d. 10 mm) [11] in order to examine the stability in redox process to find out in detail its possible application in production of valuable chemicals towards chemical looping process. The loading of sample to be is approximately 100 mg and it is placed between quartz wool plugs. In addition, to achieve the desired temperature in the catalyst bed, the reactor is introduced in an electric furnace which is monitored by K-type thermocouples placed between inside and outside of the reactor [4].

Different reducers (methanol, bio-ethanol and bio-gas) and oxidizers (CO_2 and H_2O) were used in the redox experiments performed in the reactor depending on the particular aim. The methanol chemical looping experiments were performed at 500^{o}C whereas the bio-ethanol and bio-gas experiments were performed at higher temperature of 750^{o}C. Each chemical looping cycle consisted of a reduction pulse (3 min) followed by a reoxidation pulse (3 min) with He pulse (3 min) in between.

The experiments were carried out at two temperatures, 500^{o}C and 750^{o}C, using methanol and ethanol as reducing agents and CO_2 for reoxidation in both cases. At both these temperatures, redox pretreatment was carried out using alternating 5% H_2/Ar (reducer) and CO_2 (oxidizer) with He purging between them were set out for each sample. The total flows rate of gases into the reactor were kept constant, 200 Nml/s for reducer and oxidizer, by means of Brooks mass flow controllers. The consumption of H_2 and CO_2 during the process was monitored online using a Mass Spectrometer detector whose response was systematically

calibrated with reference gases [11]. The sample was again treated with methanol/ethanol chemical looping, to study the effect of crystallite size and redox cycles. As a proof of concept H_2O was used as reoxidizing agent, to study the production of H_2.

An important performance test which indicates the process results is **yield.** The yield of the process can be defined as the fuel conversion or product obtained. It is the product obtained during the process relying on fuel conversion divided mass of oxygen storage material used.

$$\text{Yield } (Y_i) = \frac{n_{CO}}{W} \qquad \textbf{Equation 3.7}$$

Where:

- n_{CO} = Mole of CO produced [mol]
- W_{Fe} = Mass of oxygen carrier material [kg]

3.2.6 Transmission Electron Microscopy (TEM)

Transmission electronic microscopy (TEM) is a significant analytical tool which procures crystallographic, morphologic and compositional information on materials. In this technique, a beam of electrons is transmitted through a sample causing the interaction between both and giving rise to an image which is magnified and focused onto an imaging instrument (a layer of photographic film or a fluorescent screen). The image resolution in TEM apparatus is very high due to the fact that the wavelength of electrons is dependent on the energy and, then, can be adjusted to achieve a smaller wavelength. Electrons can be engendered by field emission or by thermionic discharge and, next, they are speeded up by an electric field and focused on the specimen. Sample thickness must be sufficiently low to detect electrons.

A JEOL JEM-2200FS: Cs-corrected, operated at 200 kV, equipped with a Schottky-type field-emission gun (FEG), EDX JEOL JED-2300D and JEOL in-column omega filter (EELS) was used for TEM measurements [7]. Specimens were prepared by immersion of a lacey carbon film on a copper support grid into the as prepared sample by blowing off the excess of powder [4].

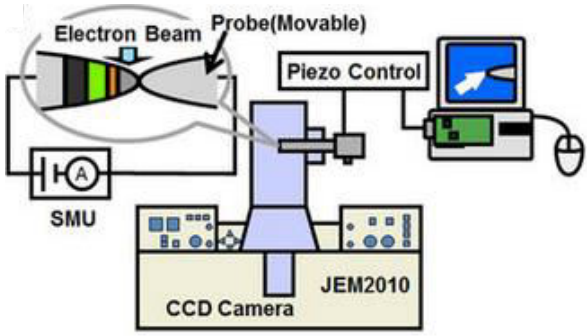

Figure 3.14. – TEM Experimental setup

3.2.7 Energy Dispersive X-Ray analysis (EDX)

It is an analytical X-Ray technique to determinate the elemental composition and chemical characterization of a material. This EDX system is attached to Transmission Electron Microscopy (TEM) setup. Apart from the composition calculation of each element in the analysed sample, an Elemental mapping and image analysis can be performed by EDX. A beryllium specimen retainer was used to remove secondary X-ray fluorescence in the spectra.

3.2.8 Inductively Coupled Plasma – Atomic Emission Spectroscopy (ICP-AES)

Inductively Coupled Plasma-Atomic Emission Spectroscopy also known as ICP-Optical Emission Spectrometry (ICP-OES) is a very versatile and one of the most common analytical technique for elemental analysis because of accurate detection limits, high specificity and multi-element capability.

The process consists of an Argon plasma source dissociates the nebulized sample exciting the electrons to a higher energy level. In a way that when they return to ground state, they emit radiation (energy, photons) at a specific wavelength which is characteristic of each element. The solid sample has to be dissolved before introducing it in the setup so materials are mixed with sodium peroxide or borate.

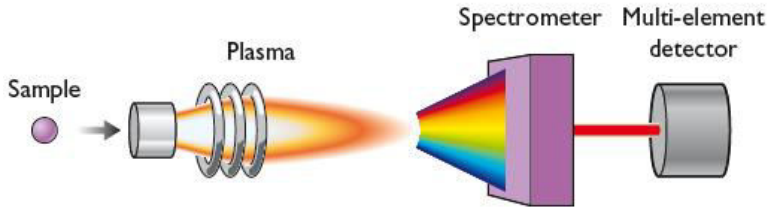

Figure 3.15. – ICP operation.

This technique is also employed towards quantitative analysis of the as prepared sample. The ionization of the sample results in the emission of wavelengths and the intensity of these peaks is proportional to the concentration of that element. This relationship is represented by Lambert-Beer law:

$$log_{10}\ \frac{I_o}{I} = \varepsilon \cdot l \cdot c \qquad \textbf{Equation 3.8}$$

Where

- I = Measured intensity.
- I_o = Measured reference intensity.
- ε [m^3/(mol/m)] = Molar absorptivity.
- c [mol/m^3] = Molar concentration.
- d [m] = Path length.

✓ **Materials and methods conclusions**

The various characterization techniques have been described in detail. TEM and ex situ XRD would be employed to study the state of the material before and after the reaction. Redox properties of these materials would be studied during H_2-TPR and CO_2-TPO in the Autochem set up. In addition the phase transformation during H_2-reduction and CO_2-reoxidation would be studied in a D8 discover in situ XRD set up. The activity and stability would be tested in step response reactor set up.

CHAPTER 4 CHARACTERIZATION

In this chapter a structural investigation on the as prepared modified ferrite materials has been performed using XRD and TEM. In addition the redox behavior of these materials were investigated by comparing the conventional H_2-TPR and CO_2-TPO consumption profiles with the crystallographic changes in the in-situ XRD.

4.1 CHARACTERIZATION OF AS PREPARED MATERIALS

4.1.1 XRD analysis

Phase identification of as prepared Co-ferrites ($CoFe_2O_4/CeZrO_2$) and Ni-ferrites ($NiFe_2O_4/CeZrO_2$) is described in this section. In the as prepared Co ferrites, the characteristic peaks for $CoFe_2O_4$ corresponding with 2θ positions at 30.5°, 35.5°, 43°, 54°, 58° and 62.5° (Figure 4.1a) were identified. The most intense peaks were observed in the unsupported $CoFe_2O_4$. However the intensity of these peaks decreased as the loading of the support material $CeZrO_2$ increased (Figure 4.1a). The peaks of $CoFe_2O_4$ are gradually replaced by peaks characteristic to $CeZrO_2$ at of 29°, 34.5°, 48° and 59° in higher loadings (20wt% and 50wt%$CoFe_2O_4$-$CeZrO_2$). This could be due to fine dispersion and a relatively smaller crystallite size. Similarly in the Ni ferrites (Figure 4.1b), diffraction patterns corresponding to $NiFe_2O_4$ at 30°, 36°, 44°, 54°, 57° were identified. As the loading of the support increases peaks characteristic to $CeZrO_2$ were more prominent as in the case of $CoFe_2O_4/CeZrO_2$ materials.

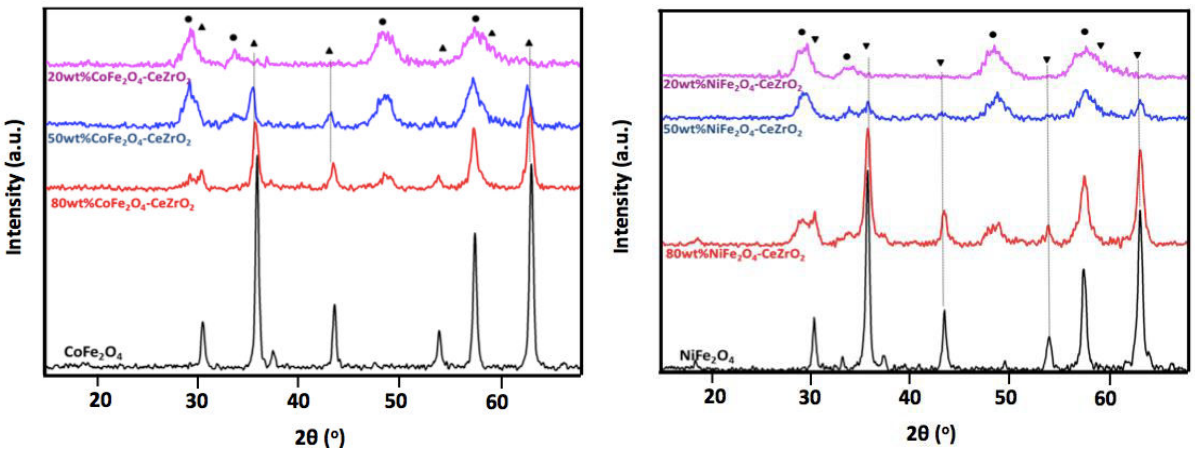

Figure 4.1 - XRD patterns of as prepared (a) $CoFe_2O_4$-$CeZrO_2$ and (b) $NiFe_2O_4$-$CeZrO_2$ with varying loading (100wt%-20wt%$CoFe_2O_4$/$NiFe2O_4$-$CeZrO_2$)

- **Crystallite size**

Crystallite size of $CeZrO_2$, $CoFe_2O_4$ and $NiFe_2O_4$ materials are calculated using Scherrer equation, by fitting Gaussian to the characteristic peaks. Figure 4.2 shows the calculated crystallite size with varying support content. Note that the error bars represent the standard deviation when averaging calculated crystallite dimension over different peaks.

The largest crystallite size is exhibited by unsupported crystallites, with $CoFe_2O_4$ ~57nm and $NiFe_2O_4$ ~45nm. With increasing loading, the crystallite size of spinel phase ($CoFe_2O_4$ and $NiFe_2O_4$) in Co and Ni modified ferrites decreased as shown in the Figure 4.2. A relatively smaller crystallite size was observed in Ni modified ferrites.

However in 20wt%$NiFe_2O_4$/$CoFe_2O_4$-80wt%$CeZrO_2$ major peak contributions from $CeZrO_2$ were observed. Due to the close overlap in the peak positions of $NiFe_2O_4$/$CoFe_2O_4$ and $CeZrO_2$, the crystallite size of these materials could not be accurately determined from XRD. But however the crystallite size of these materials is further expected to decrease which is indicated by the dotted line. A detailed TEM study has been performed on this material to identify the sample morphology and elemental distribution.

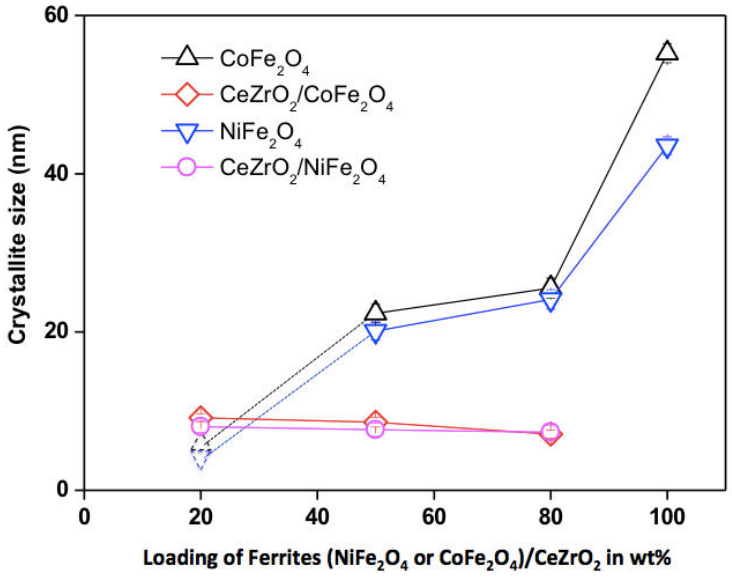

Figure 4.2 – Evolution of crystallite size in $CoFe_2O_4$/NiFe2O4-$CeZrO_2$ materials. Error bars represent standard deviation on averaging the crystallite size over different peaks. The dotted lines are a guide to the eye.

Similarly for $CeZrO_2$ phase the crystallite size analysis showed that highest crystallite size was shown in 20wt%$NiFe_2O_4$/$CoFe_2O_4$-80wt%$CeZrO_2$ (~15nm) and smallest crystallites in 80wt%$NiFe_2O_4$/$CoFe_2O_4$-20wt%$CeZrO_2$.

4.1.2 TEM-EDX analysis

In order to obtain structural information on samples with lower loading of $CoFe_2O_4$ and $NiFe_2O_4$, TEM measurements along with EDX elemental mapping are performed.

- 20wt% $CoFe_2O_4$-$CeZrO_2$

The Figure 4.3a shows the sample morphology with crystallite sizes varying between ~10-20nm. The elemental mapping of these images exhibits that Co and Fe (Figure 4.3b) are dispersed uniformly throughout the material indicating the formation of $CoFe_2O_4$. Similarly, Ce and Zr (Figure 4.3c) are also evenly distributed in the sample. This suggests the formation of $CeZrO_2$. However from TEM images the crystallite size of two different types of crystallites could not be determined as all the elements are uniformly distributed throughout the material. The observations from TEM support the findings obtained from XRD.

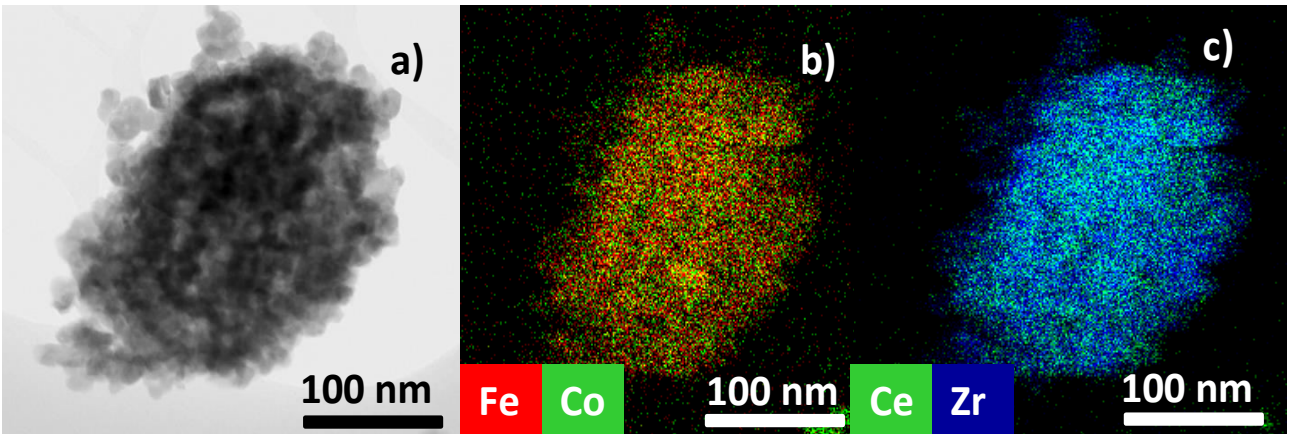

Figure 4.3 – TEM-images of 20wt%$CoFe_2O_4$ - $CeZrO_2$: showing the sample a) morphology and EDX elemental mapping of (b), Co and Fe along with (c) Ce and Zr

- 20 wt% $NiFe_2O_4$-$CeZrO_2$

Similarly, TEM analysis on these as prepared materials showed crystallites between 10-20nm were observed (Figure 4.4a). The EDX overlay images of Ni and Fe show that these were spread throughout the

sample uniformly (Figure 4.4b) indicating the formation of $NiFe_2O_4$. Additionally the elemental distribution of Ce and Zr shows (Figure 4.4b) that they are evenly distributed throughout the sample forming $CeZrO_2$. As in the case of $CoFe_2O_4$ the crystallite size of two different types of phases namely $NiFe_2O_4$ and $CeZrO_2$ could not be distinguished as they were distributed throughout the sample uniformly. In addition to the TEM analysis, the bulk elemental composition was also determined using ICP analysis. The results were in agreement with the expected composition of the samples.

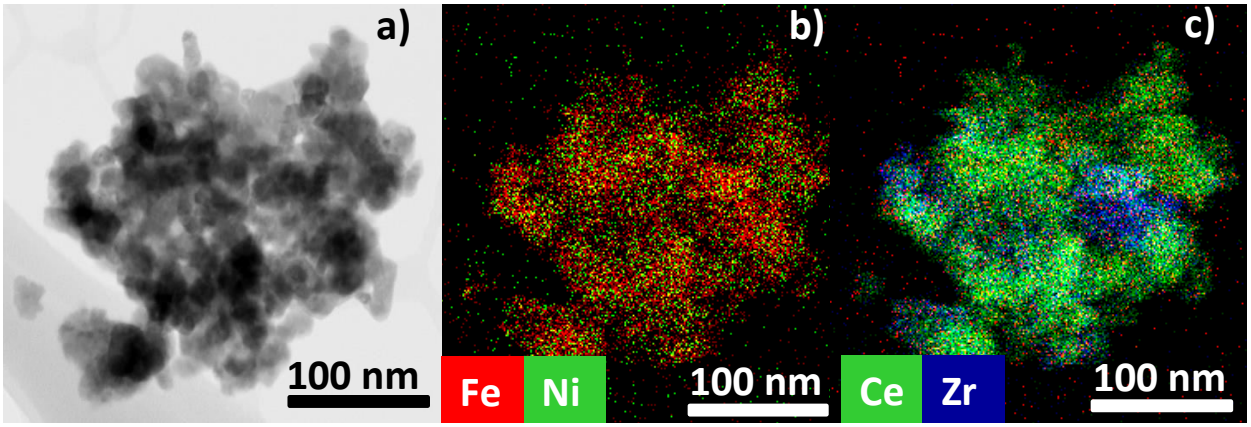

Figure 4.4 – TEM-images of 20wt%$NiFe_2O_4$- $CeZrO_2$ showig the a) sample morphology and b) elemental mapping of Ni and Fe along with c) Ce and Zr.

4.1.3 N_2-B.E.T. analysis

The Figure 4.5 shows the obtained specific surface area results of N_2-B.E.T. measurements for each sample of both Co and Ni ferrites. It is observed that cobalt modified iron oxide surface area increases with the loading of $CeZrO_2$ promoter.

The main functions of the support material is to prevent sintering and to achieve a good dispersion. Thus, the more quantity of support, the better activity of the sample meaning higher surface area. Furthermore, on the basis of literature, the larger surface area (more active sites), the smaller particles since the relationship between surface area and crystallite size is inverse (Equation 4.1). For Ni samples, a similar trend was observed.

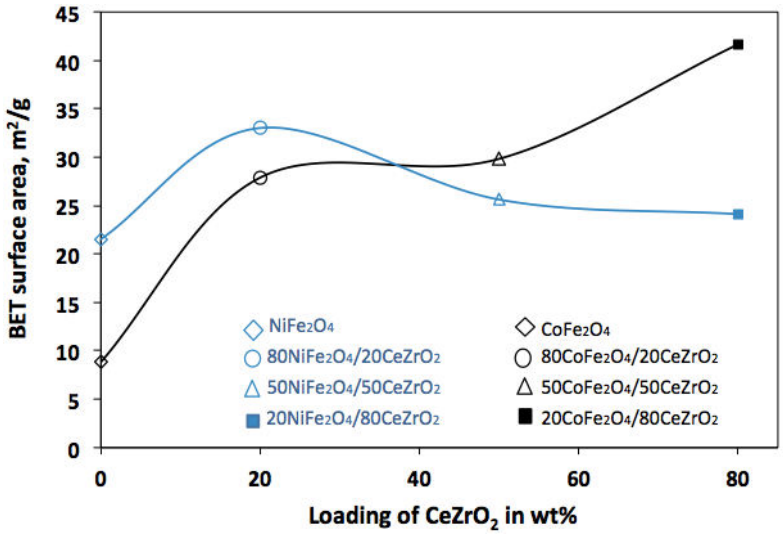

Figure 4.5 – N_2- B.E.T. specific surface area of as-prepared bifunctional materials.

4.2 REDOX PROPERTIES

A H_2-TPR and CO_2-TPO study was performed on bulk iron oxides and modified ferrites to compare the redox properties. The materials were subjected towards two consequent redox cycles to test the repeated reducibility. The repeated reducibility of these materials was studied in Autochem and the various phases that were being reduced and oxidized were identified using in situ XRD.

As a first step, the redox properties of bulk iron oxide were compared with ferrites. The H_2-TPR of Fe_2O_3, $NiFe_2O_4$ and $CoFe_2O_4$ (Figure 4.6a) show that the ferrite materials showed complete reduction at a much lower temperature (~525°C).

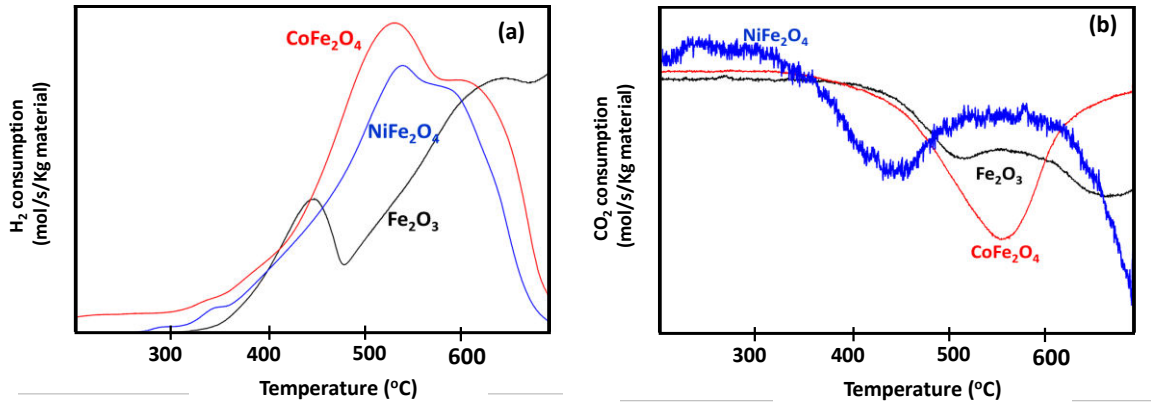

Figure 4.6 – Iron oxide vs Modified iron oxide redox properties during a) H_2-TPR and b) CO_2-TPO.

However the reduction of bulk Fe_2O_3 remains incomplete with a consumption peak at ~425°C characteristic to transition of Fe_2O_3 to Fe_3O_4. The peak at ~600°C represents transition of Fe_3O_4 to FeO. The complete reduction to metallic Fe can only take place at a much higher temperature.

Similarly the CO_2-TPO (Figure 4.6b) reoxidation profiles show an early onset of reoxidation in $NiFe_2O_4$ (~425°C) followed by $CoFe_2O_4$ (~550°C). However the oxidation of bulk Fe in Fe_2O_3 remains incomplete with two consumption peaks at ~500°C and ~640°C. Thus ferrite materials showed enhanced redox properties in comparison to bulk Fe_2O_3. Thus ferrite materials were further investigated.

4.2.1 $CoFe_2O_4$ and $NiFe_2O_4$

The bulk $CoFe_2O_4$ and $NiFe_2O_4$ were subjected to two times redox cycles. The H_2-TPR of $CoFe_2O_4$ (Figure 4.7a) shows a first reduction peak at 530°C and a small shoulder at 600°C. The first consumption peak could be due to the reduction of surface spinel and the second represents the onset of bulk reduction. However in the second cycle the reduction temperature shifted to a much higher temperature with a single broad consumption peak.

Nevertheless during the CO_2-TPO the material reoxidized at the same temperature, in contrary to the profile exhibited during H_2-TPR. But the amount of material redoxidized was much lower in comparison to the first cycle. This shift in redox temperatures could be due to probable sintering or phase segregation.

A similar analysis was performed on $NiFe_2O_4$, the H_2-TPR (Figure 4.7c) revealed that the temperature of reduction increased from 540°C in cycle 1 to 580°C in cycle 2. However, the CO_2 reoxidation temperature (Figure 4.2d) shifted from 450°C in cycle 1 to 550°C in cycle 2 unlike $CoFe_2O_4$ where the spinel reoxidized at the same temperature. The reduction and reoxidation temperatures exhibited by $NiFe_2O_4$ were lower in comparison to $CoFe_2O_4$. Further, phase transformation during the redox process was investigated using in situ.

Figure 4.8 gives an overview of in-situ XRD of two consecutive cycles: H_2-TPR and CO_2-TPO carried out in $CoFe_2O_4$ sample. The diffraction peaks of $CoFe_2O_4$ are identified at 2θ = 36° and 43.5°. During the H_2-TPR cycle 1 the spinel reduces to FeO (wuestite) (2θ = 42°) at 420°C. In addition alloy CoFe (2θ = 45°) formation is detected at 480°C. During reoxidation the alloy transforms to probable Fe_3O_4 and a separate metallic Co phase.

This indicates that the spinel segregates into metallic Co and Fe_3O_4 and does not reoxidize back to spinel $CoFe_2O_4$. Similarly in the second cycle the spinel undergoes reduction to CoFe alloy and reoxidizes to Fe_3O_4 and Co metal. This could eventually lead to phase segregation and elevated temperatures of reduction and reoxidation. This is in agreement with the result obtained from the conventional H_2-TPR and CO_2-TPO study.

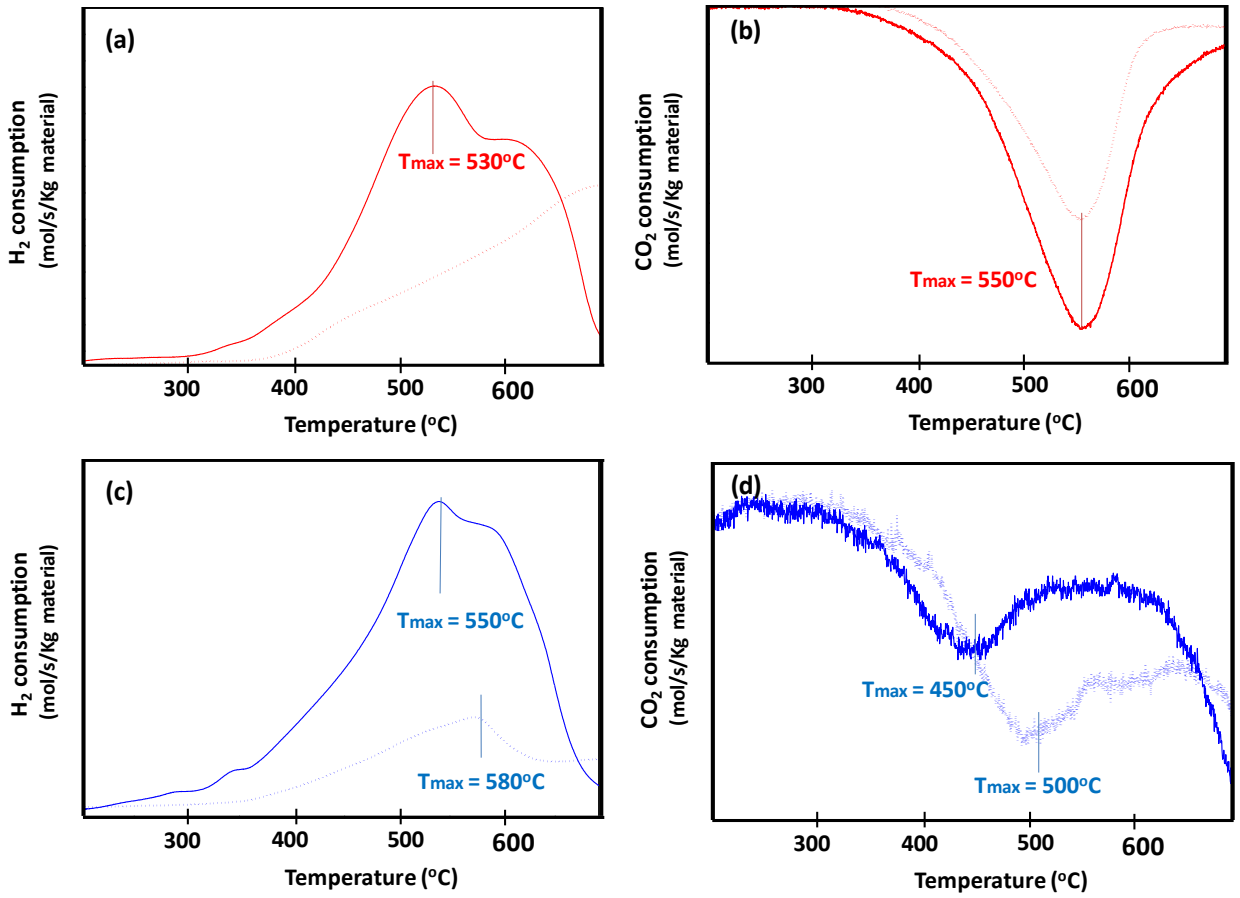

Figure 4.7 –The redox properties of $CoFe_2O_4$ during. a) H_2-TPR and b) CO_2-TPO and $NiFe_2O_4$ during c) H_2-TPR and d) CO_2-TPO

(———) $CoFe_2O_4$ cycle1, (– · – · –) $CoFe_2O_4$ cycle2, (———) $NiFe_2O_4$ cycle1, (– · –) $NiFe_2O_4$ cycle 2

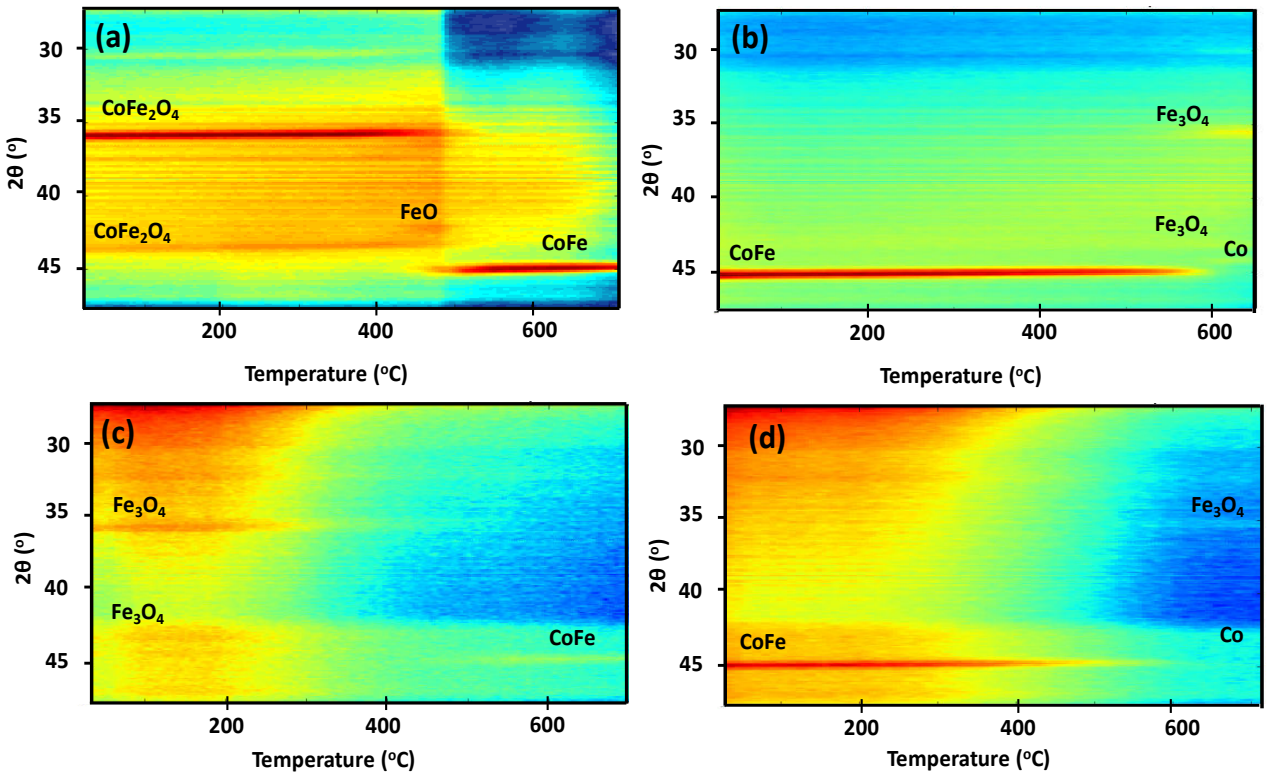

Figure 4.8 –In-situ XRD for $CoFe_2O_4$ between RT and 700°C: a) H_2-TPR cycle 1, b) CO_2-TPO cycle 1, c) H_2-TPR cycle 2 and d) CO_2-TPO cycle 2.

A similar study was performed on $NiFe_2O_4$ materials, Figure 4.9 shows an overview of in-situ XRD of two consecutive cycles: H_2-TPR and CO_2-TPO carried out in $NiFe_2O_4$ sample. From $NiFe_2O_4$ spinel (2θ = 36° and 45°), sample is reduced to alloy Fe_3Ni_2 (43.5° and 35.5°) through a transition to metallic Fe (2θ= 45°). Trance of metallic Fe are detected at 405°C and it is completely reduced at 570°C.

However during the CO_2 reoxidation, the alloy remains stable and traces of Fe_3O_4 are observed at temperatures above 600°C. This suggests that alloy is not reoxidized to spinel, it remained stable though probably, part of it is transformed to Fe_3O_4. During H_2-TPR in the second cycle the Fe_3O_4 is reduced again to alloy phase through a transition to metallic Fe. Similarly during the reoxidation a part of Fe from alloy is transformed to Fe_3O_4.

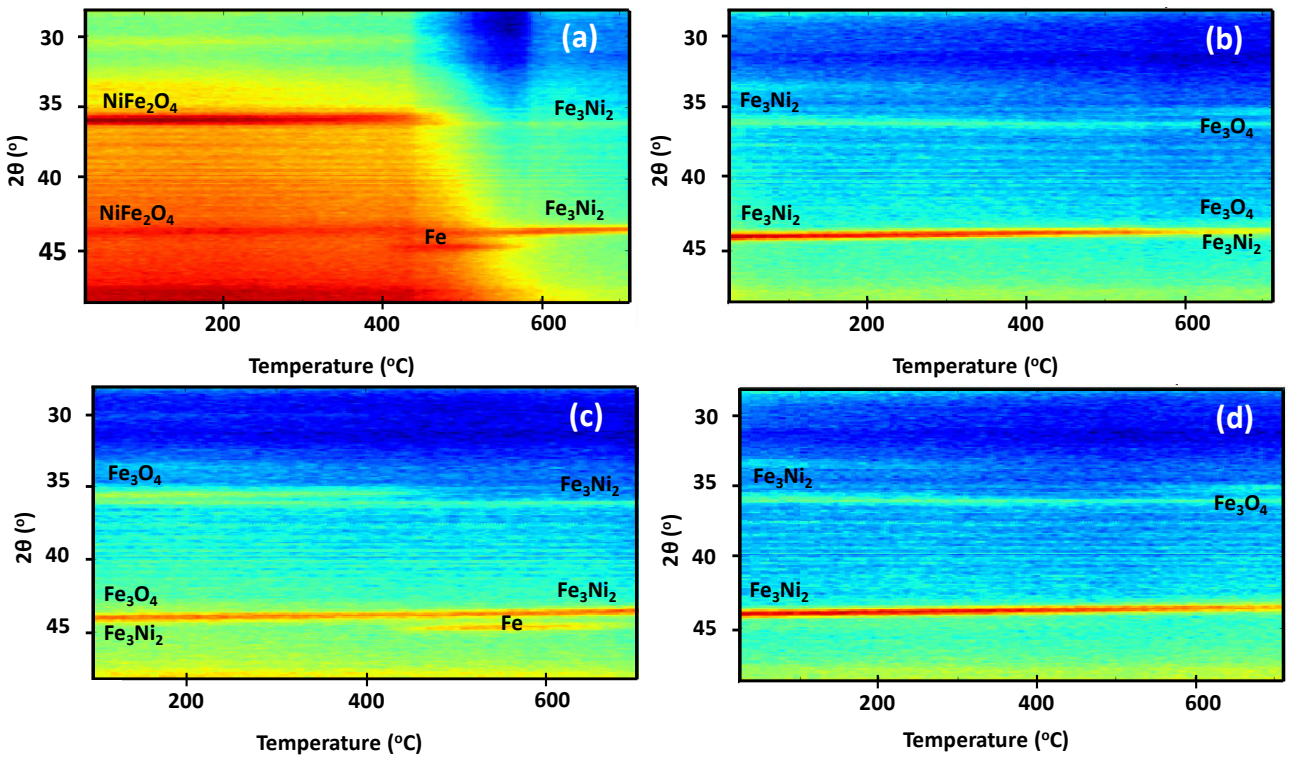

Figure 4.9 –In-situ XRD for $NiFe_2O_4$ between RT and 700°C: a) H_2-TPR cycle 1, b) CO_2-TPO cycle 1, c) H_2-TPR cycle 2 and d) CO_2-TPO cycle 2.

Hence from both the bulk material the major reason for deactivation is phase segregation into materials which transform to phases which result in loss of oxygen storage capacity hence these materials are modified with support $CeZrO_2$. A detailed redox property study on these materials has been presented in the following section.

4.2.2 80wt% $CoFe_2O_4$-$CeZrO_2$

A similar study on repeated reducibility was performed on the $CeZrO_2$ supported materials. The H_2-TPR of these materials show that during cycle 1, the reduction peak is observed at 560°C and a second shoulder at 620°C, these two peaks suggest probable surface and bulk reduction. A similar reduction profile is seen during cycle 2. The material reduced at similar temperatures in two consecutive cycles unlike the bulk unsupported material.

Similarly during reoxidation the material showed two consumption peaks with a most intense consumption peak at 560°C and a small shoulder at 620°C. This could be due to surface and bulk contributions.

The H_2-TPR and CO_2-TPO study shows that this material can repeatedly reduce (~560°C, Figure 4.10a) and reoxidize (~560°C, Figure 4.10b) at the similar temperatures unlike unsupported $CoFe_2O_4$.

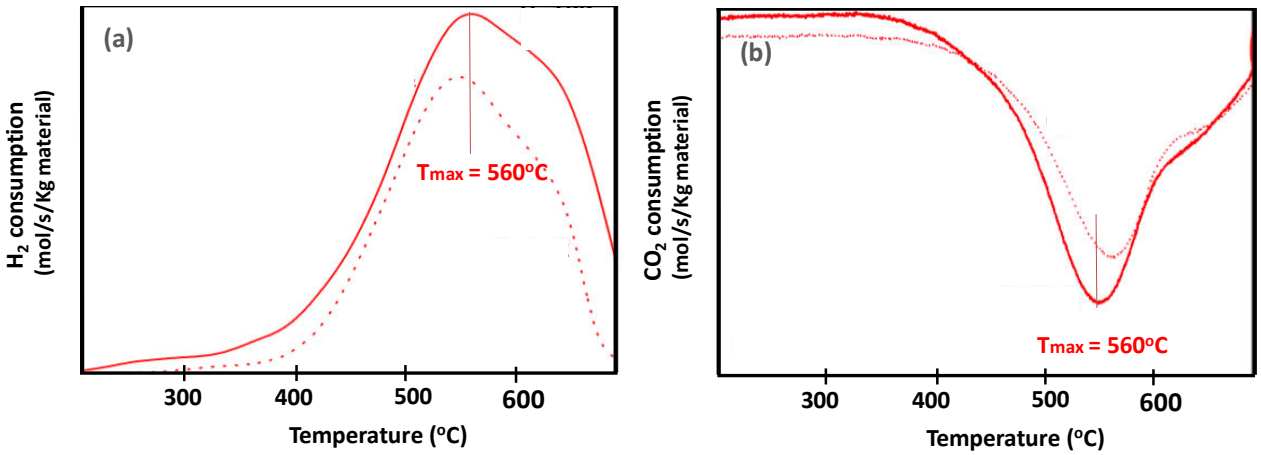

Figure 4.10 –Redox properties of 80wt%$CoFe_2O_4$-$CeZrO_2$ during. a) H_2-TPR and b) CO_2-TPO.

(———) $CoFe_2O_4$ cycle1, (.....) $CoFe_2O_4$ cycle 2

To understand the phase transformations responsible for the repeated reduction and reoxidation an in situ XRD study was performed (Figure 4.11). The H_2-TPR study (Figure 4.11a) showed the $CoFe_2O_4$ underwent a reduction through a transition from FeO phase to CoFe alloy as seen in the unsupported material.

However the alloy formation was observed at a relatively lower temperature (460°C). During reoxidation (Figure 4.11b) the alloy phase oxidized to $CoFe_2O_4$ at a temperature of 600°C and no segregation of Co metal was observed. A similar phase transition was observed during second cycle (Figure 4.11 c&d). Thus the spinel could reduce and reoxidize back to its original state without loss in oxygen storage capacity.

Nevertheless no noticeable changes in $CeZrO_2$ peak were noticed during the in situ reduction and reoxidation. A peak position analysis showed partial shift in peak position during reduction and reoxidation. This shift can be attributed to a possible partial reduction of CeO_2 owing to its redox couple (Ce^{4+}/Ce^{3+}) [4], [7].

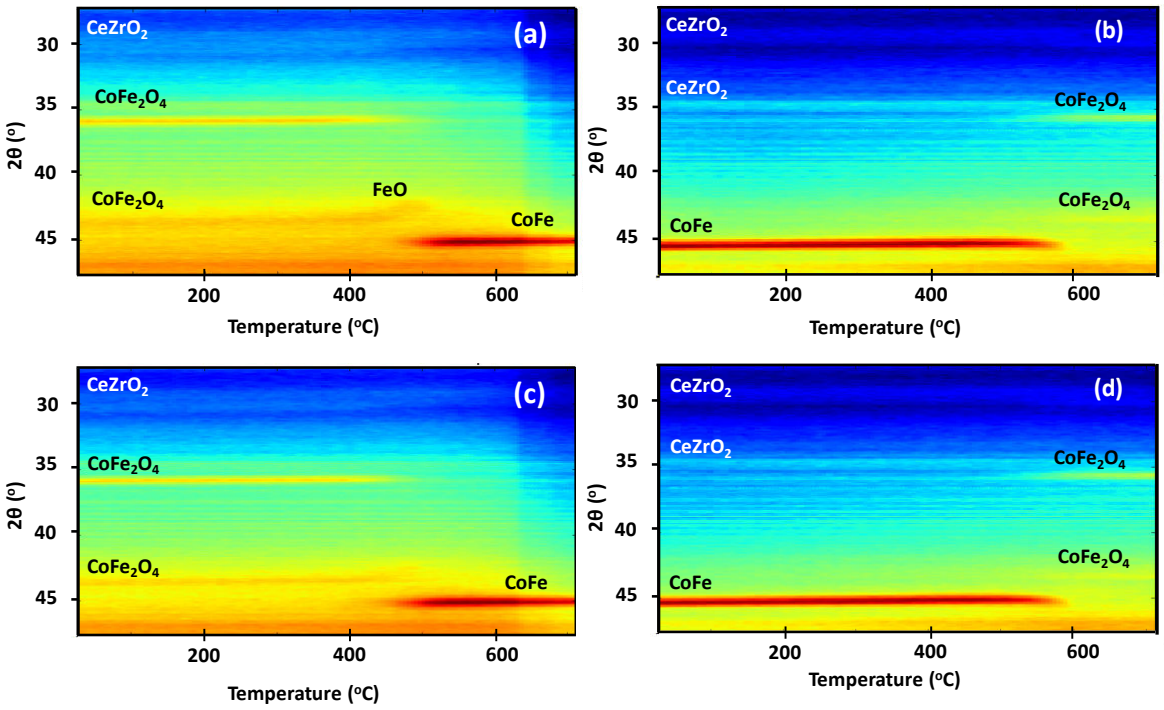

Figure 4.11 –In-situ XRD for 80wt%$CoFe_2O_4$ / 20wt%$CeZrO_2$ between RT and 700°C: a) H_2-TPR cycle 1, b) CO_2-TPO cycle 1, c) H_2-TPR cycle 2 and d) CO_2-TPO cycle 2.

The downward shift of diffraction peaks occurs because reduced cation Ce^{3+} is larger than Ce^{4+} which can provoke a lattice parameter increase realizing from its bulk fluorite lattice and, therefore, lower 2θ position [4], [7]. This is seen during the reduction (Figure 4.12a), and the vice versa has been observed during the reoxidation process (Figure 4.12b).

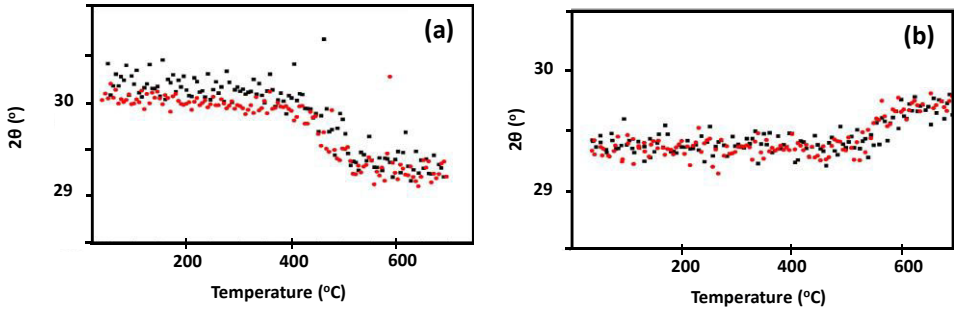

Figure 4.12 –$CeZrO_2$ peak position during: a) Reduction, H_2-TPR cycles 1,2 and b) Oxidation, CO_2-TPO cycles 1,2. (■)cycle 1 (■) cycle 2

A similar analysis was performed on 50wt%$CoFe_2O_4$-$CeZrO_2$ materials, the phase transition temperatures were similar to 80wt%$CoFe_2O_4$-$CeZrO_2$ and the results are reported in the appendix (Appendix Figure B9, Figure B10).

4.2.3 20wt% $CoFe_2O_4$-$CeZrO_2$

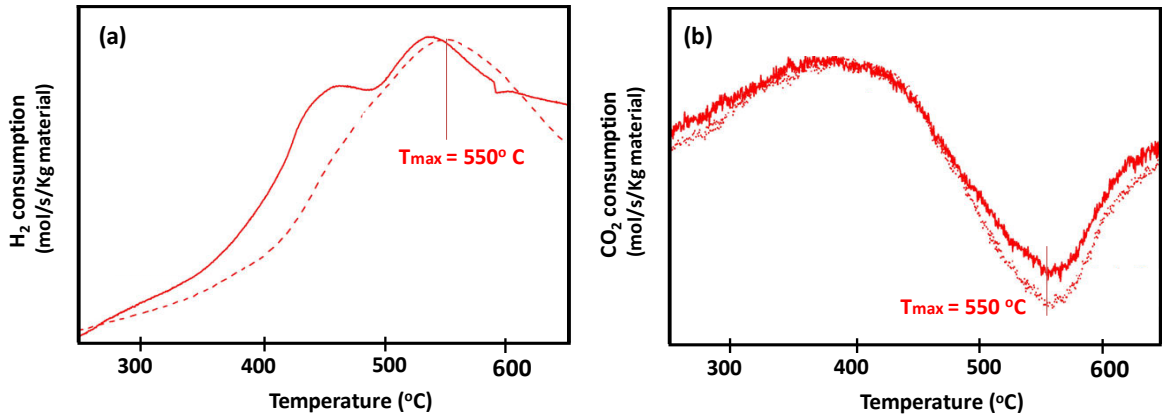

Figure 4.13 –Redox cycles of 20wt%$CoFe_2O_4$-$CeZrO_2$ during. a) H_2-TPR and b) CO_2-TPO.

(———) cycle1, (.....) cycle 2

In 20wt%$CoFe_2O_4$-$CeZrO_2$, during the H_2-TPR (Figure 4.13), onset of reduction occurs at a much lower temperature (450°C) and a second maximum at 550°C. However during the second cycle a single peak with a maximum at 550°C was observed. Whereas during the reoxidation step the material reduced and reoxidized at the same temperature (550°C). An in situ XRD analysis was performed on this material to understand the phase transformations.

A faint diffraction peak of $CoFe_2O_4$ is noticed during the first H_2-TPR cycle (Figure 4.14a), which exhibits a transition to CoFe alloy at 450°C. However during reoxidation step, alloy is reoxidized back to spinel at 500°C. The reduction and reoxidation of spinel occurred at a relatively lower temperature in comparison to higher loadings of $CoFe_2O_4$. A similar trend in the next consecutive cycle of H_2-TPR and CO_2-TPO was observed.

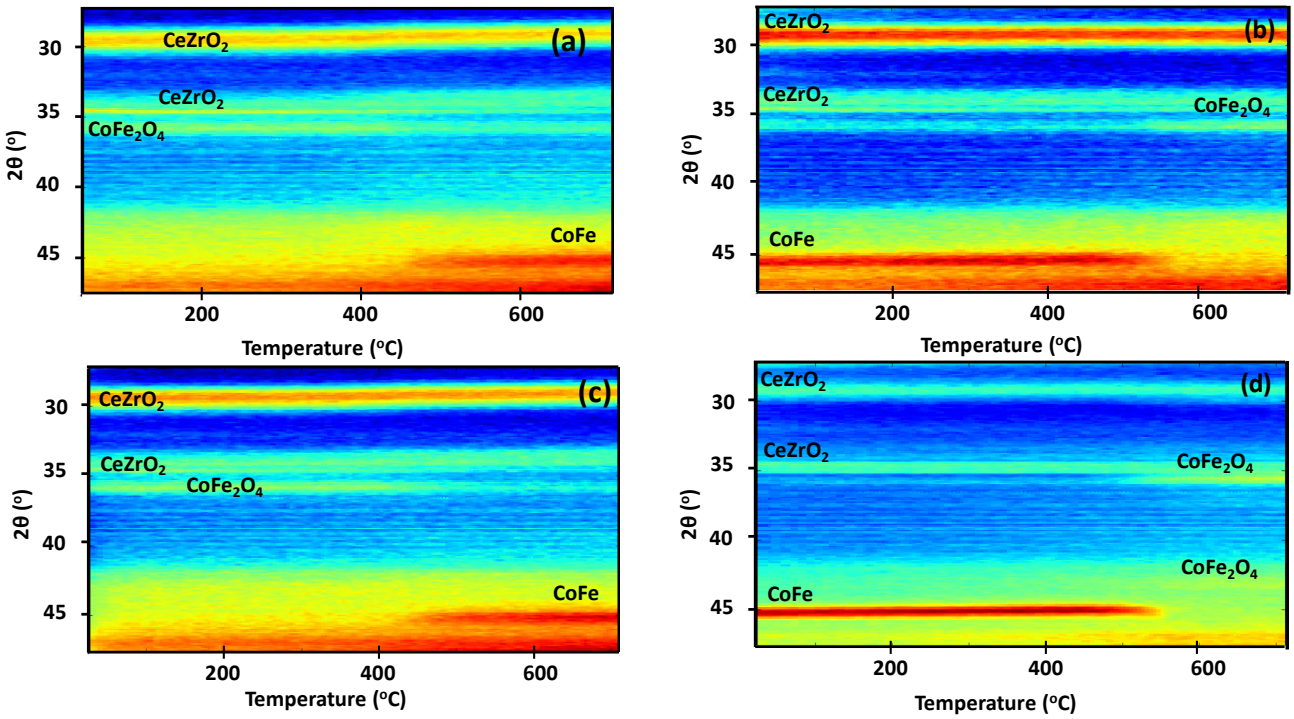

Figure 4.14 –In-situ XRD for 20wt%$CoFe_2O_4$ / 80wt%$CeZrO_2$ between RT and 700°C: a) H_2-TPR cycle 1, b) CO_2-TPO cycle 1, c) H_2-TPR cycle 2 and d) CO_2-TPO cycle 2.

However the $CeZrO_2$ peaks remained stable during reduction and reoxidation. No peaks due to reduction to Ce^{+3} were identified. However a peak position analysis as in the case of 80wt%$CoFe_2O_4$-$CeZrO_2$ showed partial reduced and reoxidation.

4.2.4 80wt% $NiFe_2O_4$ - $CeZrO_2$

The H_2-TPR study is shown in Figure 4.15a. Similar to modified ferrites these materials also show repeated reduction at similar temperatures, with consumption peak at 540°C and a shoulder at around 600°C. These peaks also represent the contributions of surface and bulk reduction in the case of contributions of $CoFe_2O_4$ The reoxidation profiles also show that these materials can be reoxidized at similar temperatures as shown in the H_2-TPR. However in the case of cycle 1, two contributions of surface and bulk reoxidation are clearly observed but in the second cycle, the first shoulder at 450°C becomes less prominent, but the major reoxidation peak is seen at 600°C.

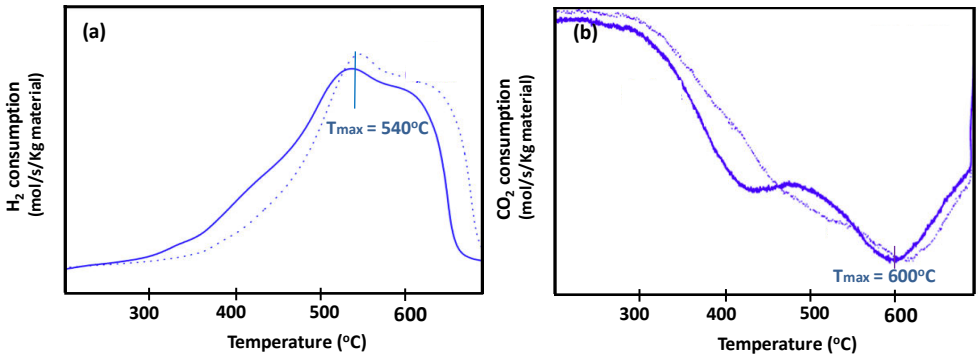

Figure 4.15 –Reduction and reoxidation of 80wt%$NiFe_2O_4$ -$CeZrO_2$ during. a) H_2-TPR and b) CO_2-TPO.

(———) $NiFe_2O_4$ cycle1, (.....) $NiFe_2O_4$ cycle 2

The in situ XRD study showed that during reduction (Figure 4.16a) the spinel transforms to alloy Fe_3Ni_2.at 500°C. This alloy remains stable during reoxidation (Figure 4.16b), however under CO_2, it decomposes to metallic Ni at 44.5° and magnetite (Fe_3O_4) at 600°C. In second reduction process, apart from Fe_3Ni_2, the presence of metallic Fe is exhibited at higher temperatures (Figure 4.16c). However during reoxidation the Fe is reoxidized to Fe_3O_4 at 480°C and also a part of alloy decomposes to Fe_3O_4 and metallic Ni.

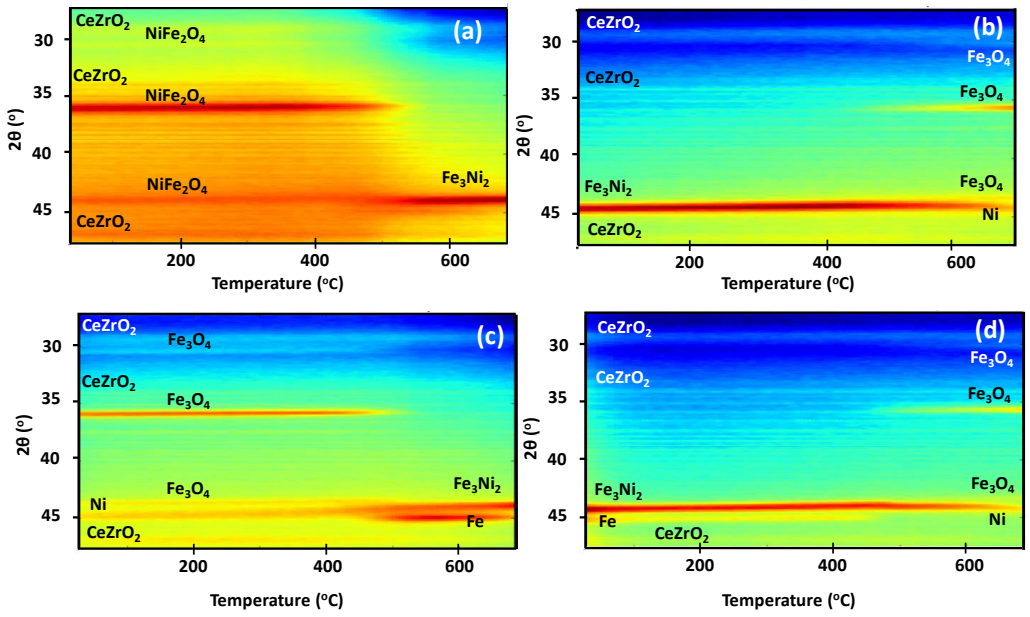

Figure 4.16 –In-situ XRD for 80wt%$NiFe_2O_4$-$CeZrO_2$ between RT and 700°C: a) H_2-TPR cycle 1, b) CO_2-TPO cycle 1, c) H_2-TPR cycle 2 and d) CO_2-TPO cycle 2.

No noticeable phase transitions were observed in $CeZrO_2$ peaks hence to understand the reducibility of $CeZrO_2$ phase, a peak position analysis was performed as in the case of $CoFe_2O_4$-$CeZrO_2$ materials. The peak position analysis showed a similar trend in Figure 4.12, indicating that $CeZrO_2$ also contributed towards the redox reaction. A similar redox analysis was performed on samples on 50wt%$NiFe_2O_4$-$CeZrO_2$. (Appendix Figure B12, Figure B13)

4.2.5 20wt% $NiFe_2O_4$ - $CeZrO_2$

However in lower loading, the reduction and oxidation occurred at a much lower temperature. The H_2-TPR and CO_2-TPO analysis show that during the first cycle (Figure 4.17a) the reduction occurred at much lower temperatures (330°C) in comparison to other materials. However during the second cycle shifted to a much higher temperature (390°C). The reoxidation of the material during the first and the second occurred at the same temperatures (490°C).

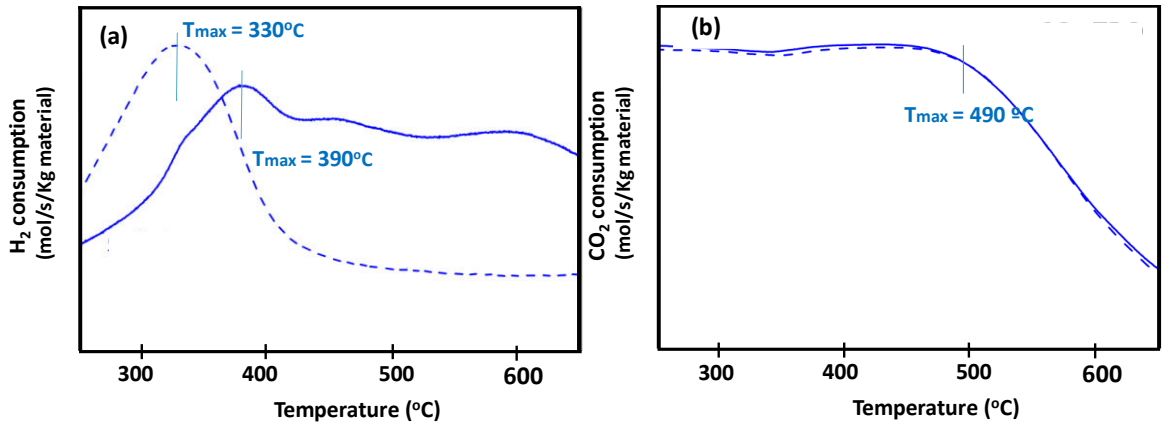

Figure 4.17 –Reduction and reoxidation of 20wt%$NiFe_2O_4$ -$CeZrO_2$ during. a) H_2-TPR and b) CO_2-TPO.

(——) $NiFe_2O_4$ cycle1, (…….) $NiFe_2O_4$ cycle 2

Further an in situ XRD analysis was performed on this sample and it was observed that the spinel reduced to an alloy Fe_3Ni_2 and metallic Fe, during first H_2-TPR (Figure 4.18a). The reduction to alloy phase Fe_3Ni_2 is seen at temperature of 430°C. However during the reoxidation, the metallic Fe is reoxidized to Fe_3O_4 and a part of the alloy remains unoxidized in the form of metallic Ni (Figure 4.18b). A same trend in reduction and reoxidation is seen in cycle 2, during H_2-TPR (Figure 4.18c) and CO_2-TPO (Figure 4.18d). In Ni-modified ferrites most of the spinel reduces to an alloy Fe_3Ni_2 and a part of it remains as metallic Ni, due to which

there is a loss in oxygen storage capacity. The $CeZrO_2$ peaks remained stable throughout and did not show reduction due to phase transformation. However a peak position analysis revealed a partial reduction and reoxidation as in 80wt%$NiFe_2O_4$-$CeZrO_2$ (Appendix Figure B.14)

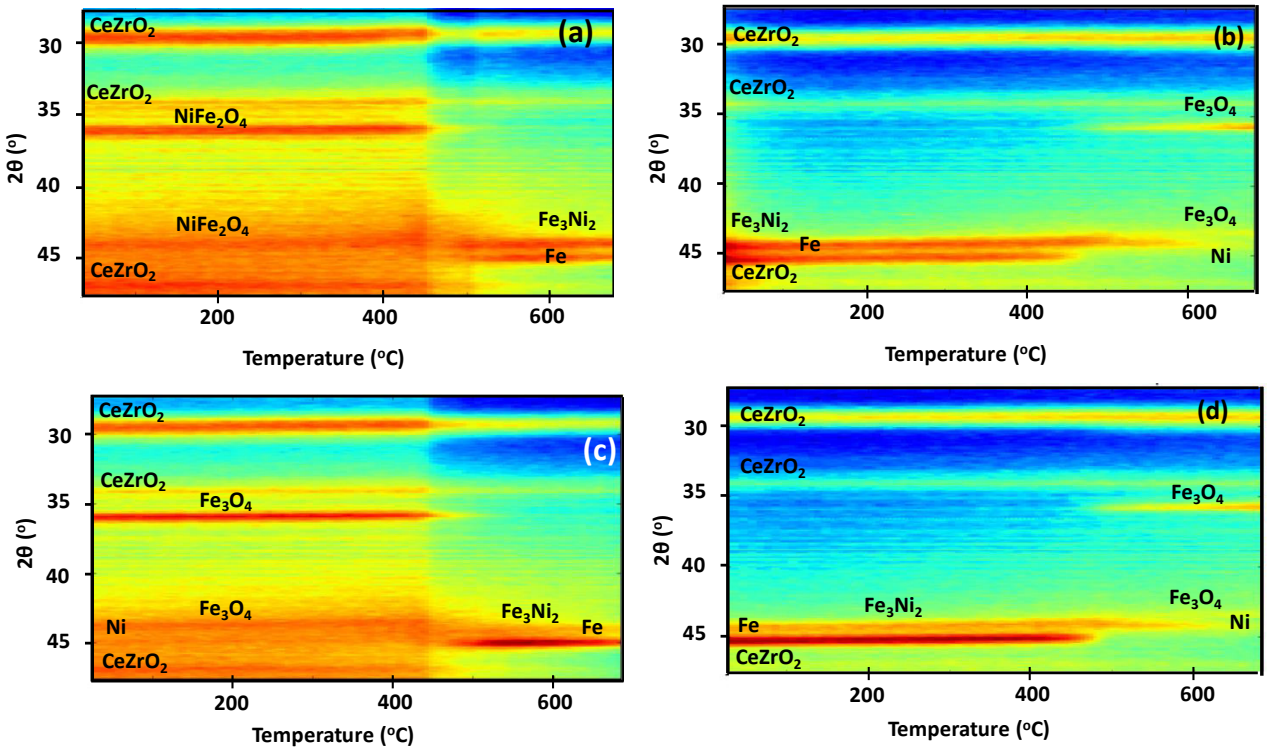

Figure 4.18 –In-situ XRD for 20wt%$NiFe_2O_4$ - $CeZrO_2$ between RT and 700°C: a) H_2-TPR cycle 1, b) CO_2-TPO cycle 1, c) H_2-TPR cycle 2 and d) CO_2-TPO cycle 2.

For all the $CoFe_2O_4$/$CeZrO_2$ samples a detailed full XRD scan analysis is presented in the Appendix B under phase segregation. Further, to test the repeated reducibility redox cycles were performed at 500°C and 750°C to see the applicability in the cyclic redox process. The various phase transformations were monitored in an in situ XRD.

4.3 IN-SITU XRD ISOTHERMAL REDOX CYCLES

In order to test the stability of modified ferrite materials as oxygen carrier, several samples were exposed to 5 subsequent in-situ XRD redox cycles. Each cycle consists of four stages: Firstly, stabilization through

helium stream followed by H_2 reduction, purging under helium and, finally, CO_2 oxidation according to the following scheme (Figure 4.19)

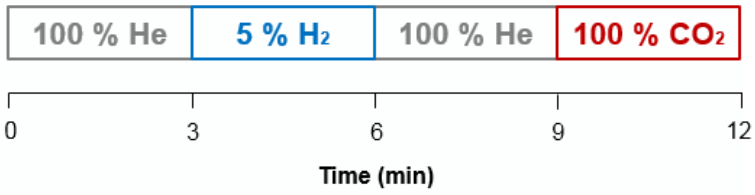

Figure 4.19 –Scheme of one isothermal redox cycle.

4.3.1 Low temperature (500 °C) redox cycles

Both Co and Ni ferrites were subjected to repeated redox cycles at 500°C. In the $CoFe_2O_4$ materials it was observed that the spinel repeatedly reduces and reoxidizes between an alloy and spinel phase. $CeZrO_2$ remain visually stable during the experiment.

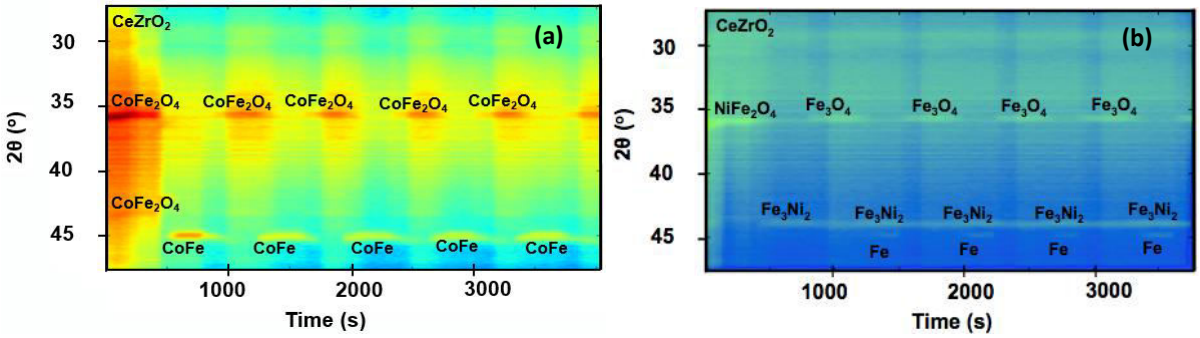

Figure 4.20 –In-situ XRD isothermal redox cycles at 500 °C for (a) 80wt% $CoFe_2O_4$-$CeZrO_2$ and (b) 80wt% $NiFe_2O_4$-$CeZrO_2$

However in the Ni ferrites the spinel transforms partly to alloy Fe_3Ni_2 (Figure 4.20b) and metallic Fe during reduction. During reoxidation Fe is transformed into Fe_3O_4 and alloy remains stable. No peak position changes were noticed in $CeZrO_2$.

4.3.2 High temperature (750 °C) redox cycles

Similarly both the materials were tested at high temperatures for H_2 reduction and CO_2 reoxidation. The Co-modified ferrites showed similar behavior during 500°C (Figure 4.21a). However the Ni-Ferrites, reduced to Fe_3Ni_2 alloy and then reoxidized to Fe_3O_4 and a part remained unoxidized as metallic Ni. Unlike the low temperature redox cycles the Ni-ferrites showed the occurrence of metallic Ni (Figure 4.21b).

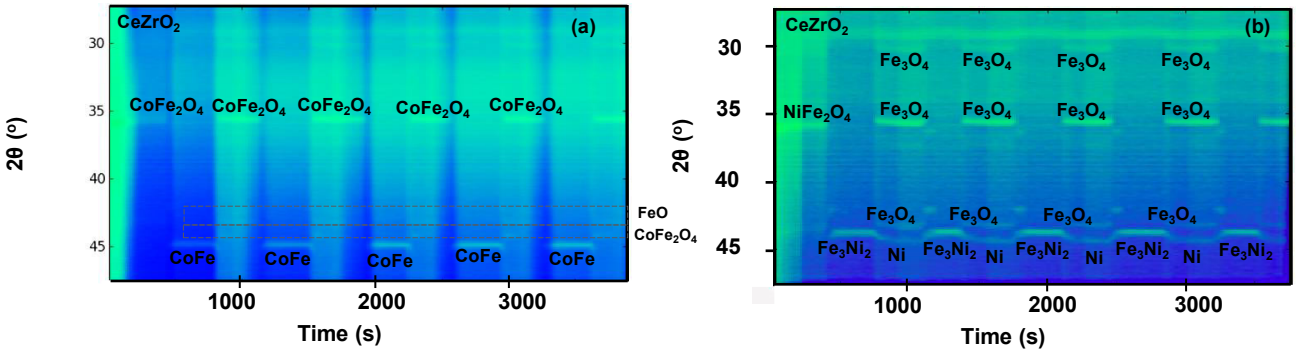

Figure 4.21 – In-situ XRD isothermal redox cycles at 750 °C for (a) 80wt% $CoFe_2O_4$-$CeZrO_2$ and (b) 80wt% $NiFe_2O_4$-$CeZrO_2$

Among both the ferrites, Co-modified ferrites show that they can cycle back to their spinel state when modified with $CeZrO_2$. This properties can be exploited to design materials which can repeatedly reduce and reoxidize at lower temperatures without loss in oxygen storage capacity. However the Ni-Ferrites undergo phase segregation and a part of Ni remains in metallic form. The presence of metallic Ni can be interesting in reforming reactions at high temperatures.

✓ **Characterization conclusions**

The in situ XRD study shows that among both the ferrites, Co-modified ferrites could cycle back to their as prepared spinel state when modified with $CeZrO_2$. This properties can be exploited to design materials which can repeatedly reduce and reoxidize at lower temperatures without loss in oxygen storage capacity. However the Ni-Ferrites undergo phase segregation and a part of Ni remains in metallic form. The presence of metallic Ni could be interesting in reforming reactions at high temperatures.

In this chapter results on activity and stability of modified ferrites have been discussed. Different feed gas namely methanol and ethanol have been tested. The state of material after reaction has been characterized using TEM.

CHAPTER 5 REDOX ACTIVITY AND STABILITY

5.1 METHANOL AND ETHANOL CHEMICAL LOOPING

In the previous section the redox properties of various materials have been investigated using H_2 and CO_2. Both the Co and Ni ferrites were subjected to test their activity and stability using methanol and ethanol as feed gas. The reaction products were monitored by a mass spectrometer and CO yield has been calculated in the reoxidation half cycle. The methanol decomposition was tested at 500°C and ethanol decomposition at 750°C.

To test activity and stability, the redox process consists of three stages. The modified iron ferrites were subjected to methanol/ethanol decomposition pulses for a period of three minutes and the regeneration was performed using CO_2 with He purging in between. This allowed to check material activity towards methanol/ethanol decomposition into syngas. Secondly, a pretreatment was performed to test stability of these materials through 100 cycles upon H_2-reduction and CO_2-reoxidation. Finally, to test real activity of the material after a long time, four more cycles were undertaken under the same conditions as first stage.

5.1.1 Methanol as feed gas

All the metal modified ferrites: 80wt%$CoFe_2O_4$-$CeZrO_2$, 50wt%$CoFe_2O_4$-$CeZrO_2$, 20wt%$CoFe_2O_4$-$CeZrO_2$, 80wt%$NiFe_2O_4$-$CeZrO_2$ and 20wt%$NiFe_2O_4$-$CeZrO_2$ were tested towards methanol chemical looping (Figure 5.1). First of all, according to Figure 5.1, it is observed that the highest CO_2 conversion to CO is attained by 20wt%$CoFe_2O_4$-$CeZrO_2$, reaching yield values between 0.002 and 0.003 mol CO/kg material, approximately. On the other hand, the lowest yield was obtained by 80wt%$CoFe_2O_4$/20wt%$CeZrO_2$, it might be due to low amount of $CeZrO_2$ leading to sintering. During the first three cycles rapid deactivation is observed in 20wt%$CoFe_2O_4$-$CeZrO_2$, the materials with 80wt%$CoFe_2O_4$-$CeZrO_2$ showed a relatively stable yield. As similar trend is seen after pretreatment of 100 cycles.

Concerning stability, both bifunctional materials with 80wt% $CeZrO_2$ support remain almost stable throughout the process owing to the fact that, after pretreatment, CO yield results are similar to those of the first period, there is no huge deactivation as for instance, the 50wt%$CoFe_2O_4$-$CeZrO_2$ case which presents high loss of activity meaning low CO_2 conversion. It is concluded that 20wt%$CoFe_2O_4$-$CeZrO_2$ is a suitable bifunctional material to be employed by Chemical Looping process as oxygen carrier.

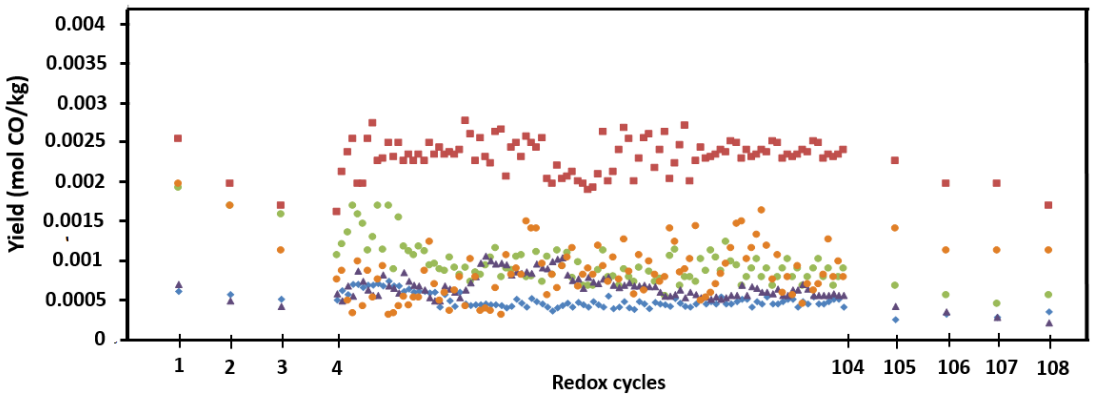

Figure 5.1 – Estimated CO yield (mol CO formed during each cycle per kg material) over several redox cycles at 500 °C using CH_3OH and CO_2 for first three cycles, H_2 and CO_2 for next 100 cycles and, again, CH_3OH and CO_2 for last four cycles. Each cycle lasts 12 min and helium is purged between each reduction and oxidation. A total gas flow of 200 Nml/s was maintained during each redox cycle. Samples subjected are (◆) 80wt%$CoFe_2O_4$/20wt%$CeZrO_2$, (●) 50wt%$CoFe_2O_4$/50wt%$CeZrO_2$, (■) 20wt%$CoFe_2O_4$/80wt%$CeZrO_2$, (▲)80wt%$NiFe_2O_4$/20wt%$CeZrO_2$ and (●)20wt%$NiFe_2O_4$/80wt%$CeZrO_2$.

In addition to the experiments above additional experiments were performed to test the ability of these materials in H_2O splitting (Figure 5.2). The sample was pre reduced and tested towards the decomposition of H_2O, then He was purged for a short period of time followed by the CH_3OH pulse. The amount of H_2 produced decreased gradually during the cycles.

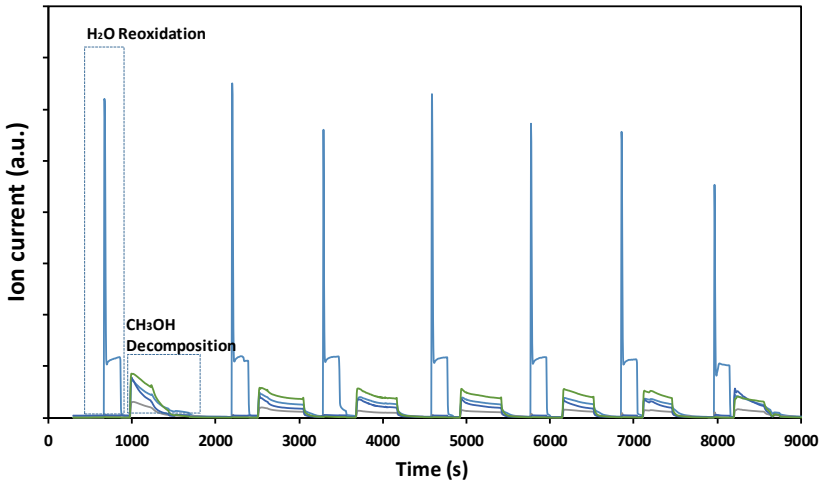

Figure 5.2 –Redox cycles at 500 °C for (a) 80wt% $CoFe_2O_4$-$CeZrO_2$ and (b) 80wt% $NiFe_2O_4$-$CeZrO_2$ (▬) H_2, (▬) CO_2, (▬) CO

5.1.2 Ethanol as feed gas

A mixture of ethanol and water in 1:1 molar ratio was prepared to test the applicability of chemical looping towards renewable feed stocks such as bio ethanol. The CO yield data for 20wt%$CoFe_2O_4$-$CeZrO_2$, 80wt%$NiFe_2O_4$-$CeZrO_2$ and 20wt%$NiFe_2O_4$-$CeZrO_2$ is shown in Figure 5.3. The highest yield was obtained by using 20wt%$CoFe_2O_4$-$CeZrO_2$ as oxygen storage material. This material a relatively stable yield during the first three and the last four cycles, unlike when using methanol where the deactivation during these cycles was rapid. This material also shows remarkable stability during the 100 redox cycles. However the material with higher $CoFe_2O_4$ content showed a much lower yield. The CO yield during the first three and the last four cycles showed a gradual decline.

The yield obtained by Ni-ferrites was much lower in comparison to that of Co-ferrites, as in the case of methanol decomposition. The CO yield during the ethanol decomposition cycles continued to degenerate continuously. This could be due to alloy formation (Fe_3Ni_2) which results in the loss of active phase. This was also observed during the in situ XRD cycling study.

The Co-ferrites showed a superior ability to split methanol and ethanol during the cycling processes. The ability to reoxidize back and forth between $CoFe_2O_4$ helped to maintain its oxygen storage capacity. However the deactivation was inevitable in these materials. The two factors responsible for deactivation are sintering and carbon formation.

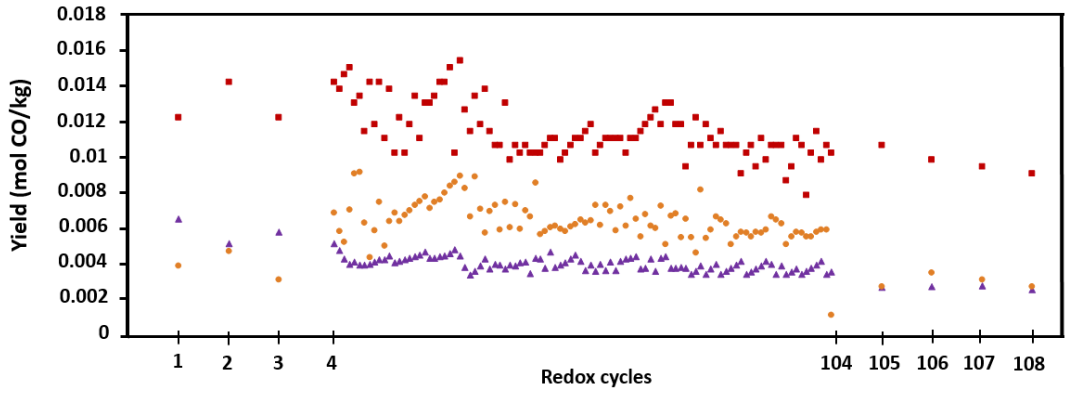

Figure 5.3 – Estimated CO yield (mol CO formed during each cycle per kg material) over several redox cycles at 750 °C using C_2H_5OH/H_2O and CO_2 for first three cycles, H_2 and CO_2 for next 100 cycles and, again, C_2H_5OH/H_2O and CO_2 for last four cycles. Each cycle lasts 12 min and helium is purged between each reduction and oxidation. A total gas flow of 200 Nml/s was maintained during each redox cycle. Samples subjected are (▲)80wt%$NiFe_2O_4$/20wt%$CeZrO_2$, (●) 50wt%$CoFe_2O_4$/50wt%$CeZrO_2$ and (■) 20wt%$CoFe_2O_4$/80wt%$CeZrO_2$.

5.2 CARBON FORMATION

The present study investigates the applicability of chemical looping process towards methanol and ethanol chemical looping process. The modified ferrites ($CoFe_2O_4/CeZrO_2$ and $NiFe_2O_4/CeZrO_2$) were subjected to methanol and ethanol chemical looping applications but deactivation due to carbon formation could not be avoided. The carbon formation was studied by using TEM and varying the redox cycle time.

5.2.1 TEM-EDX analysis

Morphological and structural analyses were performed using TEM on samples after the reaction. The TEM images of 20wt%$CoFe_2O_4$-$CeZrO_2$ are shown in Figure 5.3. The TEM image (Figure 5.4a) shows crystallites with large diameter (~30-50nm). This could be due to sintering during the cycling processes. The EDX overlay of Co and Fe together (Figure 5.4b) show that Co and Fe occur together in large crystals, indicating the existence of spinel phase. However Fe remains dispersed throughout the sample. The elemental mapping of C shows the existence of C and Fe (Figure 5.4c) together, indicating possible formation of carbides and possible encapsulation of spinel phase which leads to deactivation.

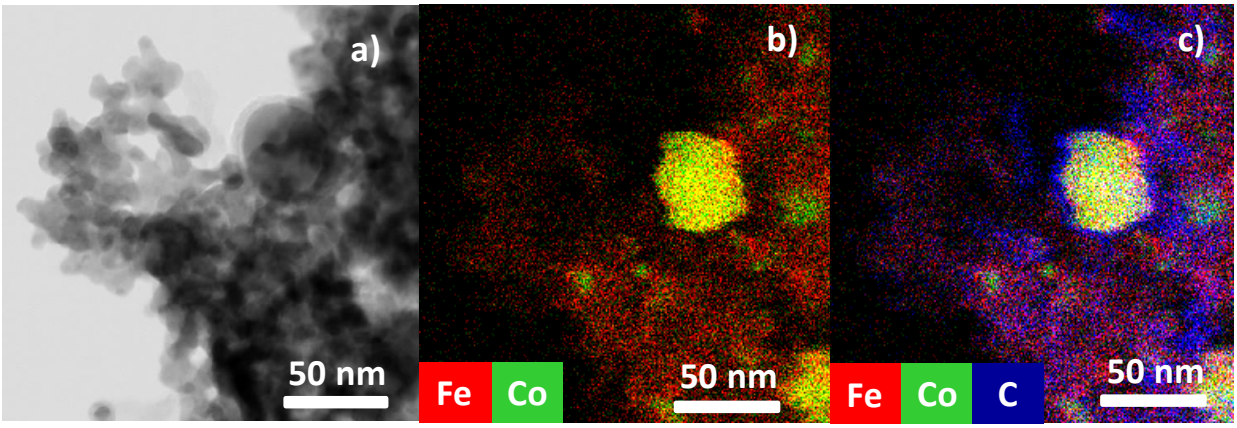

Figure 5.4. – TEM-images of 20wt%$CoFe_2O_4$-$CeZrO_2$ after methanol redox cycles: a) TEM micrograph and EDX elemental mapping b) of Fe and Co combined and c) Fe, Co, C together.

A similar TEM analysis was performed on 20wt%$NiFe_2O_4$-$CeZrO_2$. The sample showed filaments (Figure 5.5a) and agglomeration of crystallites (~28 nm). However in these images separate clusters of Ni and Fe (Figure 5.5b) are seen, indicating possible phase segregation. Carbon formation is more intense in comparison to Co-ferrites (Figure 5.5c). The samples of Ni are prone to carbon formation , not only carbon

formation is very strong but no spinel phase between Ni and Fe is observed (Figure 5.5b). Thus, due to segregation of the spinel phase the redox activity decreases and lead to deactivation.

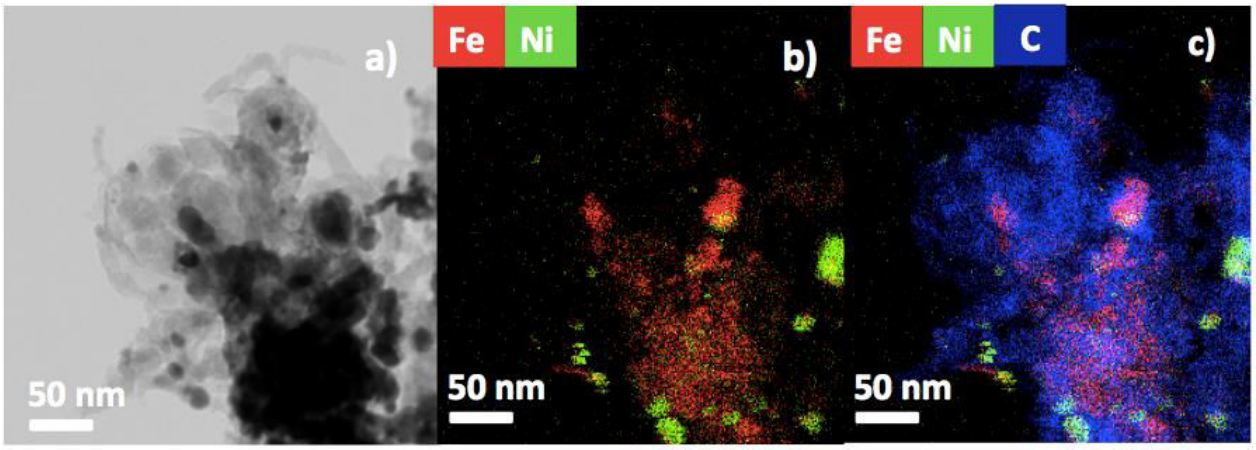

Figure 5.5 – TEM-images of 20wt%$NiFe_2O_4$-$CeZrO_2$ after redox processes: a) TEM micrograph and EDX elemental mapping of Ni (b), Fe (c), Fe and Ni combined (d), C (e) and Fe, Ni, C together.

The TEM images show that the deactivation in the samples after methanol chemical looping cycles is due to carbon formation. The TEM study of the materials after ethanol is still under progress and was not performed within the time frame, but could provide interesting insights on carbon formation. Further a carbon formation analysis was also performed on the basis of the cycle time and also the XRD analysis on the samples after the reaction. These results are discussed in detail in the next section.

5.2.2 Effect of varying redox cycling time

Carbon formation was studied by using methanol for reduction and O_2 for reoxidation and by varying cycle time from 3 min to 1 min. The experiment was performed by pulsing CO_2 for reoxidation and then pulsing O_2 to burn the carbon formed. In the oxidation half cycle the less intense fragments of CO_2 and CO can be noticed. With increase in cycle time the amount of carbon formed increases. Thus carbon formation was inevitable(Figure 5.6). This implies that these materials could not be used for high purity H_2 applications. However when CO_2 is used as reoxidation agent high purity CO could be produced, but material stability and activity are constraints. Similarly during ethanol chemical looping deactivation due to carbon formation and sintering was observed.

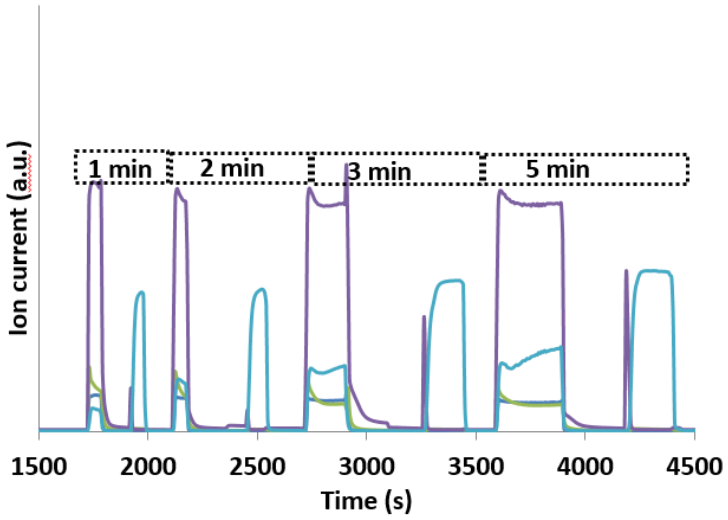

Figure 5.6 –Redox cycles at 500 °C for (a) 80wt% $CoFe_2O_4$-$CeZrO_2$ and (b) 80wt% $NiFe_2O_4$-$CeZrO_2$
( ) O_2, ( ) O, ( )CO, ( ) CO_2

Figure 5.7 shows material state after prolonged 100 cycles of methanol. In all the samples characteristic peaks of $CeZrO_2$ and $CoFe_2O_4$ were identified. In all the materials the final state of spinel was $CoFe_2O_4$, this is in agreement with the TEM EDX analysis. However in all these materials the carbide formation is inevitable. However the peak positions of FeC and CoC show a close overlap, hence it is not clear to identify the specific type of carbide.

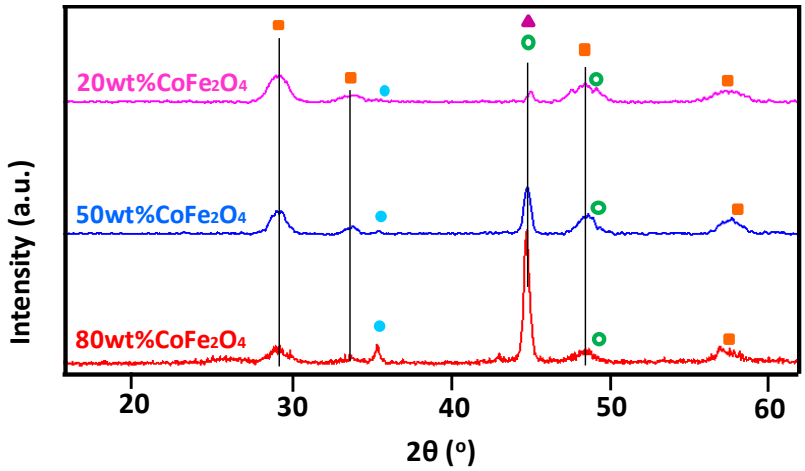

Figure 5.7 –XRD diffraction patterns of materials after 100 methanol redox cycles at 500 °C for 20wt% $CoFe_2O_4$-$CeZrO_2$, 50wt% $CoFe_2O_4$-$CeZrO_2$ and 80wt% $CoFe_2O_4$-$CeZrO_2$
(●) $CoFe_2O_4$, (Δ) Co, (▲) Cobalt carbide (Co_2C, Co_3C) , (■) CO_2, (○) Iron carbide (Fe_3C).

In addition during ethanol decomposition, CH_4 is also one of the important by-products. It was observed that CH_4 remained stable during the reaction. The applicability to decompose CH_4 was tested using a mixture of CH_4:CO_2 in 1:1 ratio.

5.3 METHANE DECOMPOSITION

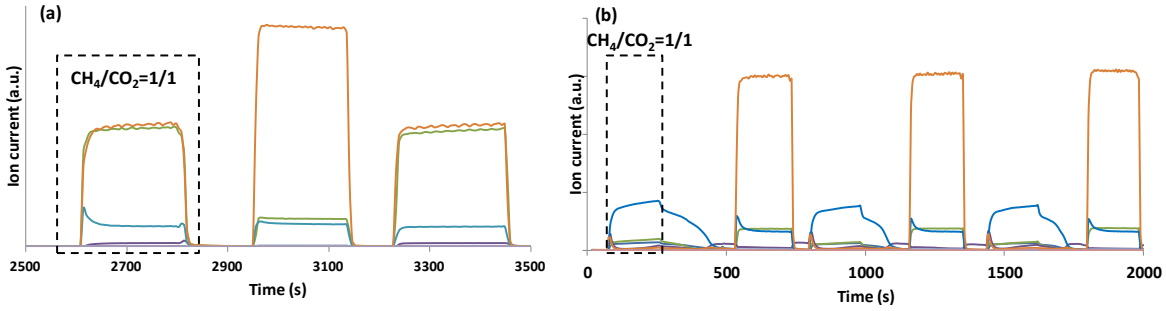

Figure 5.8 - Mass spectrometer response during dry reforming on bifunctional 20wt%$CoFe_2O_4$-$CeZrO_2$ (a) with no catalyst bed and (b) with a catalyst bed.

The experimental results showed that the material showed no activity towards splitting of CH_4 (Figure 5.8a). To investigate the decomposition of CH_4 a dual bed with layer of 10wt%Ni/$MgAl_2O_4$ was placed before the oxygen storage material. It was observed that CH_4 decomposed to CO and H_2 (Figure 5.8b), hence a catalyst is necessary to decompose methane. This needs a careful tailoring of the catalyst composition. It is well known that metallic Ni and Ni rich alloys are responsible for the decomposition of CH_4 hence find their application in reforming reactions [51]. An important learning from the thesis is to alter the composition in Ni-ferrites, so that it forms a Ni-rich alloy which would help in the decomposition of CH_4. In this case a probable Fe_3Ni_2 alloy is formed, which could result in decreased activity. The synthesis of inverse spinels ($NiFe_2O_4$, $NiFeAlO_4$) on a highly active support such as $CeZrO_2$ should be pursued further to improve the processes.

✓ **<u>Stability conclusions</u>**

Among the ferrites Co-modified $CeZrO_2$ ferrites showed best redox activity during 100 cycles during methanol and ethanol chemical looping. Carbon formation was observed in both the ferrites. In the case of $CoFe_2O_4$/$CeZrO_2$ materials no phase segregation was observed from TEM, however in $NiFe_2O_4$ separate Fe and Ni clusters were observed indicating phase segregation, which leads to loss in oxygen storage capacity. However both these bifunctional materials were not able to convert CH_4 an extra catalyst component was necessary for splitting CH_4.

CHAPTER 6 CONCLUSION

The present study investigates the applicability of chemical looping process towards methanol and ethanol chemical looping process. The modified ferrites ($CoFe_2O_4/CeZrO_2$ and $NiFe_2O_4/CeZrO_2$) were subjected to methanol and ethanol chemical looping applications, deactivation due to sintering and carbon formation could not be avoided. This implies that these materials could not be used for high purity H_2 applications. However when CO_2 is used as reoxidation agent high purity CO could be produced, but material stability and activity are constraints. Similarly during ethanol chemical looping deactivation due to carbon formation and sintering was observed.

It is well known that ferrites have an AB_2O_4 spinel structure, where A is usually a cation with +2 charge (ex: Ni, Co) and B is a cation with +3 charge (ex: Fe^{+3}). In bulk iron oxide materials (Fe_2O_3) the iron oxide cycles back to Fe_3O_4 when using CO_2 as reoxidizing agent. The Fe_3O_4 has also a spinel structure but, not all the iron cycles back to +3 state, where as in the metal ferrites the Fe occupies the B site and is always reoxidized back to +3 state during cyclic operation. Hence, when a metal ferrite cycles back and forth not only is the oxygen storage capacity of the material is restored but also has a higher oxygen storage capacity than Fe_3O_4. In this respect $CoFe_2O_4/CeZrO_2$ materials show promising application towards chemical looping applications.

However the most important finding is the spinel $CoFe_2O_4/CeZrO_2$ can reduce and reoxidize repeatedly, this could be a new application to chemical looping reforming processes. However, if in the first step these materials are thermally reduced (ex: by solar energy based sources) and then regenerated by using H_2O, high purity hydrogen with no carbon emission could be achieved. But it is limited by higher temperature of operation, currently CeO_2, $CeZrO_2$ are widely investigated materials by solar thermochemical conversion. High temperature of operation could also result in sintering of bifunctional material. However if these materials are pre-reduced using H_2, and then regenerated by using H_2O these can be used for high purity applications. Using, $CeZrO_2$ along with $CoFe_2O_4$ would combine the advantage of using renewable solar energy to generate high purity H_2. The thermally reduced material would be stored in portable storage device and then be reoxidized by H_2O to produce H_2.

APPENDICES

Appendix A: Overview of performed experiments

MATERIAL SYNTHESIS			
DATE	**EXPERIMENT**	**MATERIAL**	**LAB JOURNAL PAGE**
27/10/2015	$CoFe_2O_4/CeZrO_2$ synthesis via coprecipitation method (CP)	100-0,80-20,50-50 and 20-80 (wt%) of $CoFe_2O_4$-$CeZrO_2$	25
27/10/2015	$NiFe_2O_4/CeZrO_2$ synthesis via coprecipitation method (CP)	100-0,80-20,50-50 and 20-80 (wt%) of $NiFe_2O_4$-$CeZrO_2$	26
3/11/2015-4/11/2015	Calcination of samples	Calcination for all the samples at 650°C	27-28
17/11/2015-20/11/2015	B.E.T. measurements	All the samples	30-32
28/11/2015	TPR/TPO Autochem	Prior $CoFe_2O_4$	33
29/11/2015	TPR/TPO Autochem	80wt%$NiFe_2O_4$-$CeZrO_2$, 50wt%$NiFe_2O_4$-$CeZrO_2$and 20wt%$NiFe_2O_4$-$CeZrO_2$	33
30/11/2015	TPR/TPO Autochem	Prior $NiFe_2O_4$ and 80wt%$NiFe_2O_4$-$CeZrO_2$	33
10/12/2015	TPR/TPO Autochem	20wt%$NiFe_2O_4$-$CeZrO_2$	35
16/12/2015-18/12/2015	B.E.T. measurements	All the samples	38-39
18/01/2016	B.E.T. measurements	50wt%$NiFe_2O_4$-$CeZrO_2$ and 20wt%$NiFe_2O_4$-$CeZrO_2$	40
26/01/2016-27/01/2016	In-situ XRD analyses	100-0,80-20,50-50 and 20-80 (wt%) of $CoFe_2O_4$-$CeZrO_2$ samples	41-42
22/02/2016-23/02/2016	In-situ XRD analyses	100-0,80-20,50-50 and 20-80 (wt%) of $NiFe_2O_4$-$CeZrO_2$ samples	49-50
25/02/2016	TPR/TPO Autochem	50wt%$NiFe_2O_4$-$CeZrO_2$	50
26/02/2016	Isothermal cycles In situ XRD	90CaO-10$CaZrO_3$ sample for having more material for further study	51-54
04/03/2016-07/03/2016	Methanol Step Response experiments	80-20,50-50 and 20-80 (wt%) of $CoFe_2O_4$-$CeZrO_2$ samples	55
22/03/2016	TEM-EDX measurements	90CaO-10$CaZrO_3$ sample for having more material for further study	56

Appendix B

PHASE SEGREGATION

- $CoFe_2O_4$

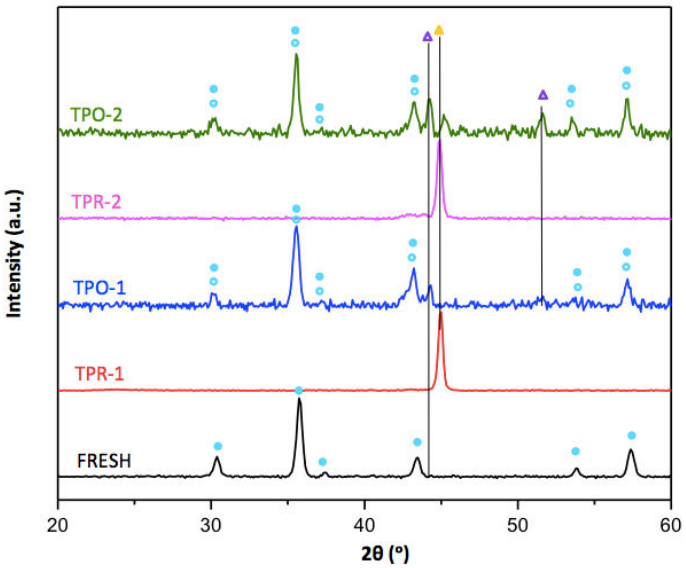

Figure B.1 – XRD spectrums identification for prior $CoFe_2O_4$: Fresh, 1st cycle TPR, 1st cycle TPO, 2nd cycle TPR, 2nd cycle TPO. (●) $CoFe_2O_4$, (○) Fe_3O_4. (Δ) Co, (▲) CoFe alloy

- 80wt% $CoFe_2O_4$-$CeZrO_2$

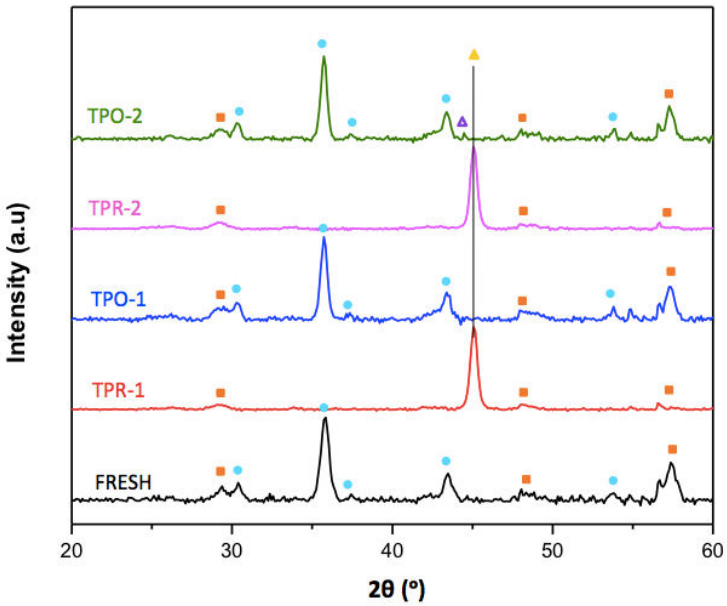

Figure B.2 - XRD spectrums identification for 80wt%$CoFe_2O_4$-$CeZrO_2$: Fresh, 1st cycle TPR, 1st cycle TPO, 2nd cycle TPR, 2nd cycle TPO. (●) $CoFe_2O_4$, (Δ) Co, (▲) CoFe alloy , (■) $CeZrO_2$,

- 50wt% $CoFe_2O_4$-$CeZrO_2$

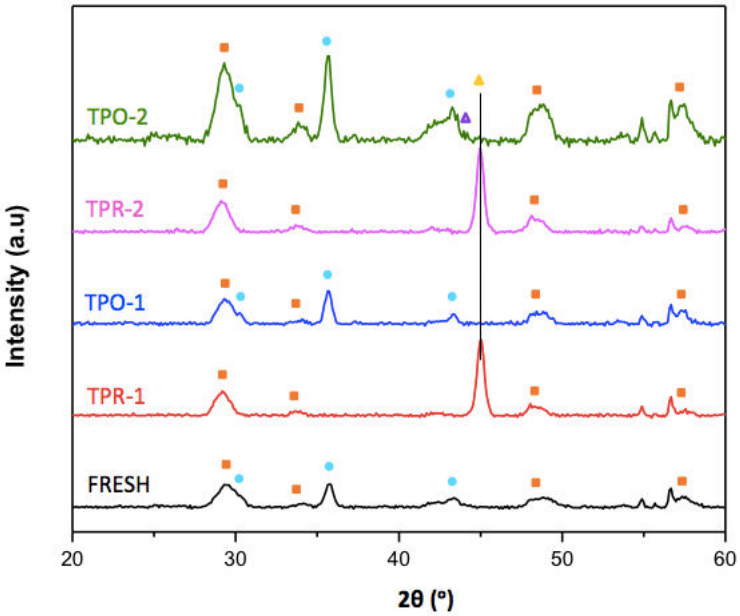

Figure B.3 - XRD spectrums identification for 50wt%$CoFe_2O_4$-$CeZrO_2$: Fresh, 1st cycle TPR, 1st cycle TPO, 2nd cycle TPR, 2nd cycle TPO. (●) $CoFe_2O_4$, (Δ) Co, (▲) CoFe alloy , (■) $CeZrO_2$,

- 20wt% $CoFe_2O_4$-$CeZrO_2$

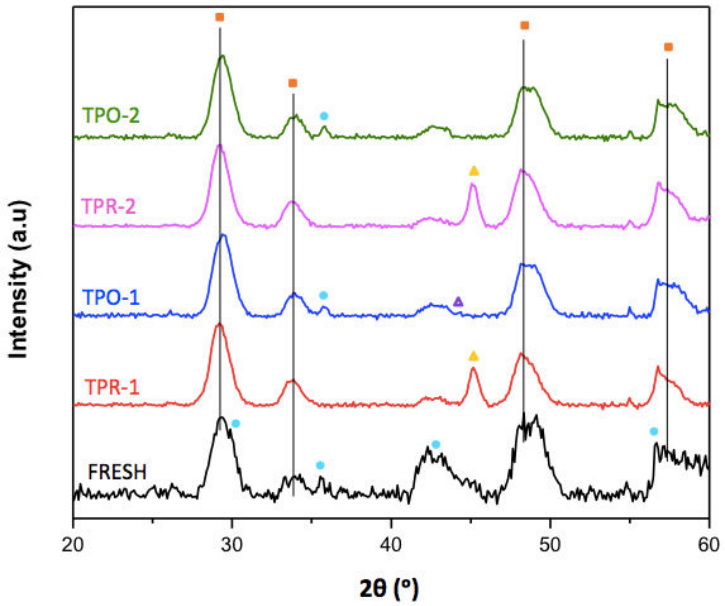

Figure B.4 - XRD spectrums identification for 20wt%$CoFe_2O_4$-$CeZrO_2$: Fresh, 1st cycle TPR, 1st cycle TPO, 2nd cycle TPR, 2nd cycle TPO. (●) $CoFe_2O_4$, (Δ) Co, (▲) CoFe alloy , (■) $CeZrO_2$,

- $NiFe_2O_4$-$CeZrO_2$

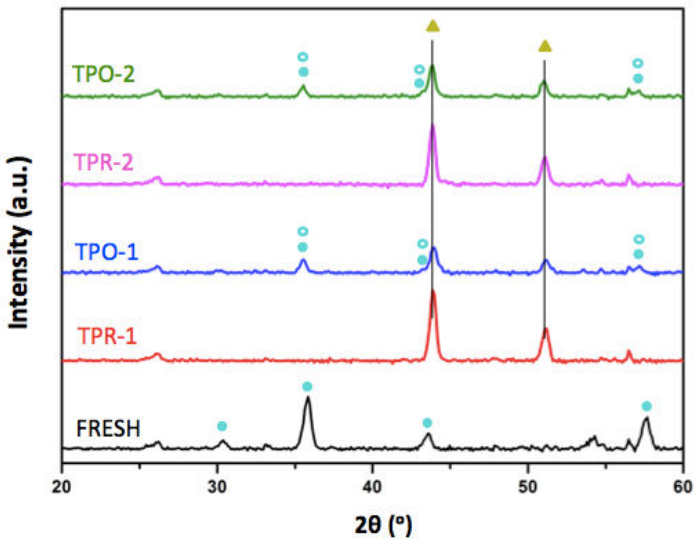

Figure B.5 – XRD spectrums identification for prior $NiFe_2O_4$: Fresh, 1st cycle TPR, 1st cycle TPO, 2nd cycle TPR, 2nd cycle TPO. (●) $NiFe_2O_4$, (○) Fe_3O_4. (▲) Fe_3Ni_2 alloy

- 80wt% $NiFe_2O_4$-$CeZrO_2$

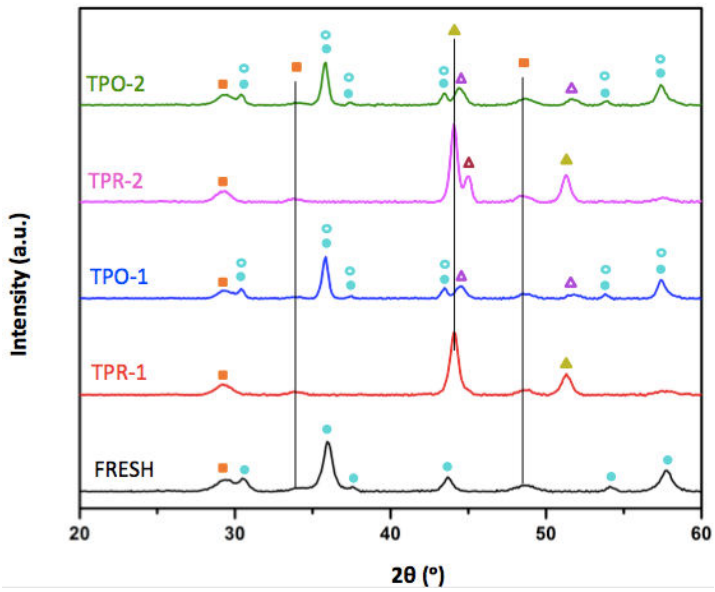

Figure B.6 - XRD spectrums identification for 80wt%$NiFe_2O_4$-$CeZrO_2$: Fresh, 1st cycle TPR, 1st cycle TPO, 2nd cycle TPR, 2nd cycle TPO. (●) $NiFe_2O_4$, (○) Fe_3O_4, (Δ) Ni, (▲) Fe_3Ni_2 alloy, (■) $CeZrO_2$, (Δ) Fe

- 50wt% $NiFe_2O_4$-$CeZrO_2$

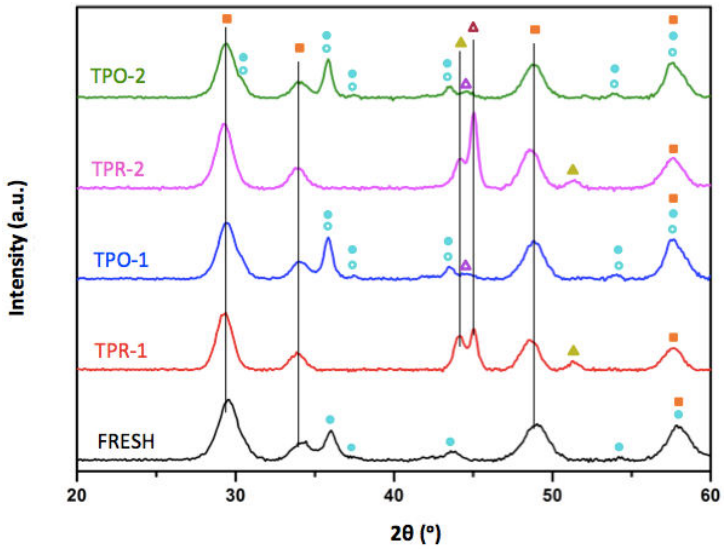

Figure B.7 - XRD spectrums identification for 50wt%$NiFe_2O_4$-$CeZrO_2$: Fresh, 1st cycle TPR, 1st cycle TPO, 2nd cycle TPR, 2nd cycle TPO. (●) $NiFe_2O_4$, (○) Fe_3O_4, (Δ) Ni, (▲) Fe_3Ni_2 alloy, (■) $CeZrO_2$, (Δ) Fe

- 20wt% $NiFe_2O_4$-$CeZrO_2$

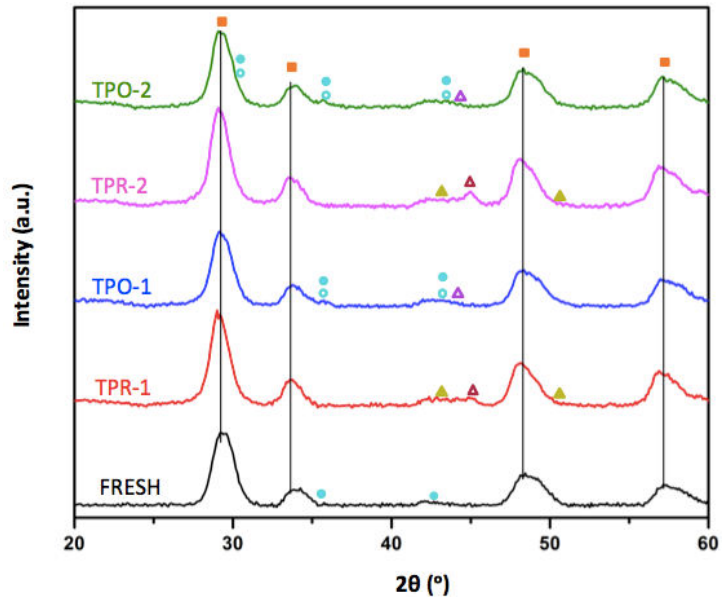

Figure B.8 - XRD spectrums identification for 20wt%$NiFe_2O_4$-$CeZrO_2$: Fresh, 1st cycle TPR, 1st cycle TPO, 2nd cycle TPR, 2nd cycle TPO. (●) $NiFe_2O_4$, (○) Fe_3O_4, (Δ) Ni, (▲) Fe_3Ni_2 alloy, (■) $CeZrO_2$, (Δ) Fe

CHARACTERIZATION IN SITU XRD

- 50wt% $CoFe_2O_4$-$CeZrO_2$

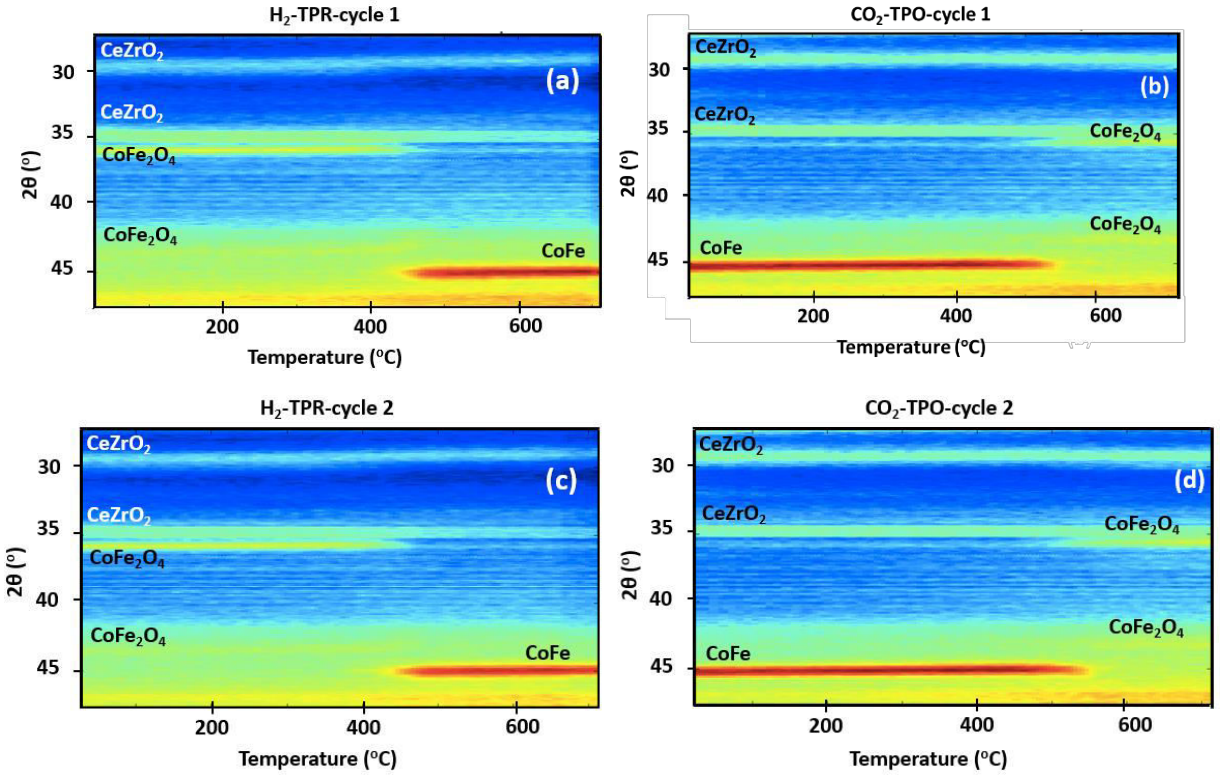

Figure B.9 –In-situ XRD for 50wt%$CoFe_2O_4$-$CeZrO_2$ between RT and 700°C: a) H_2-TPR cycle 1, b) CO_2-TPO cycle 1, c) H_2-TPR cycle 2 and d) CO_2-TPO cycle 2.

- $CeZrO_2$ peak position

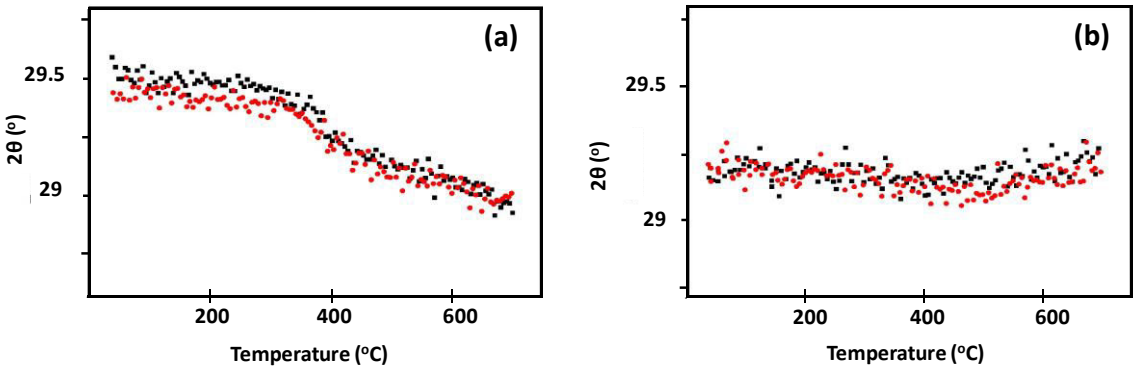

Figure B.10 –$CeZrO_2$ peak position during: a) Reduction, H_2-TPR cycles 1,2 and b) Oxidation, CO_2-TPO cycles 1,2. (■)cycle 1 (■) cycle 2

- 50wt% $NiFe_2O_4$-$CeZrO_2$

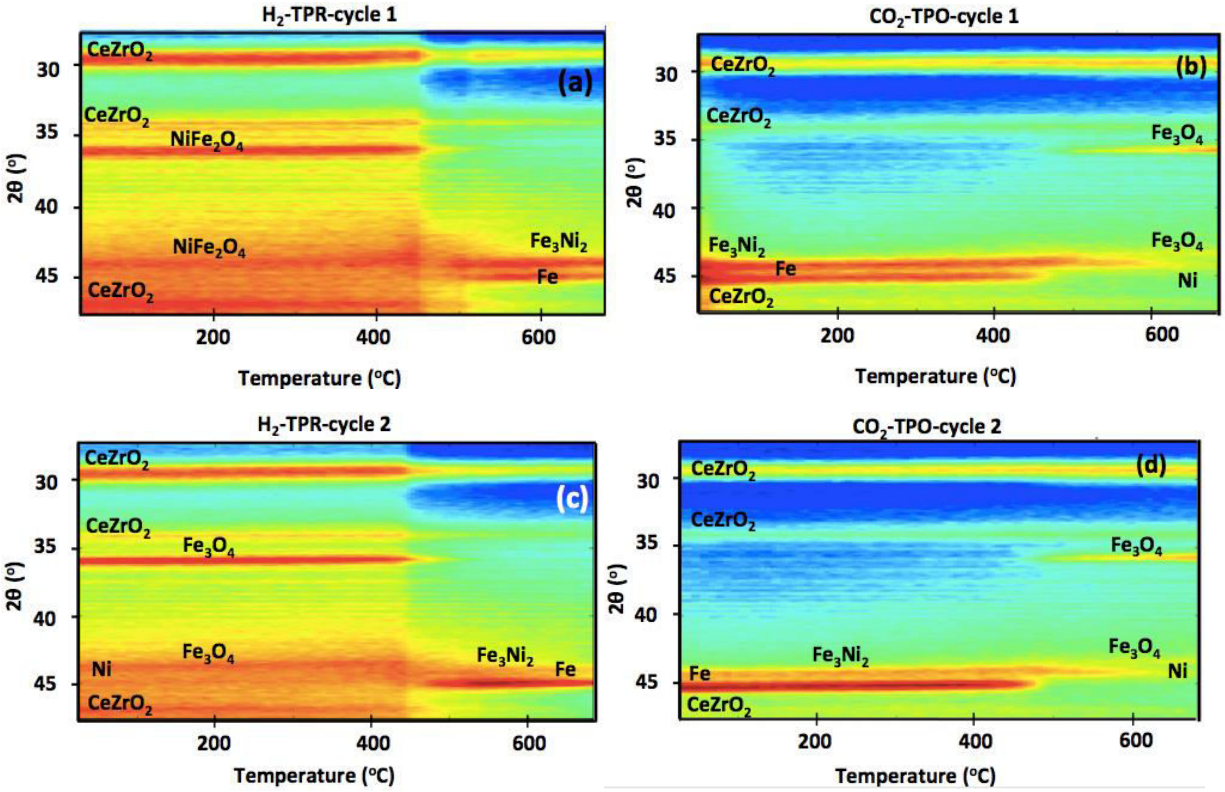

Figure B.11 –In-situ XRD for 50wt%$NiFe_2O_4$-$CeZrO_2$ between RT and 700°C: a) H_2-TPR cycle 1, b) CO_2-TPO cycle 1, c) H_2-TPR cycle 2 and d) CO_2-TPO cycle 2.

- $CeZrO_2$ peak position

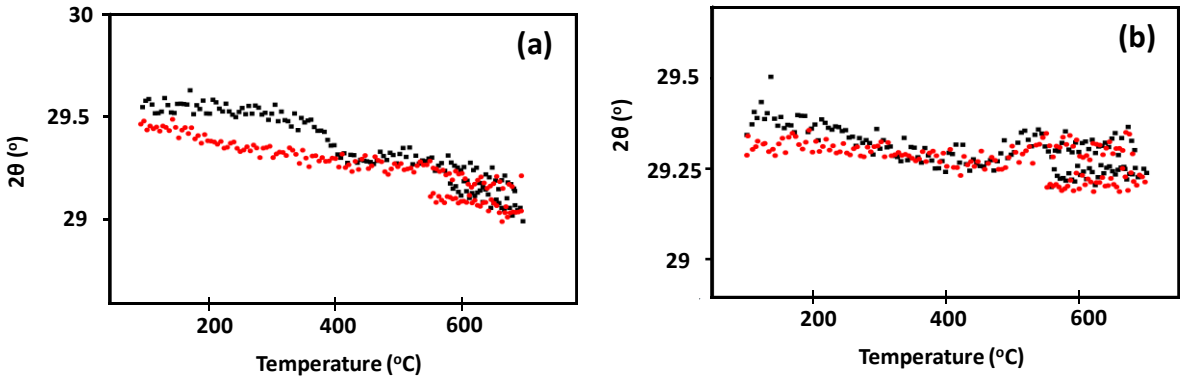

Figure B.12 –$CeZrO_2$ peak position during: a) Reduction, H_2-TPR cycles 1,2 and b) Oxidation, CO_2-TPO cycles 1,2.

(■)cycle 1 (■) cycle 2

- 80wt% $NiFe_2O_4$-$CeZrO_2$

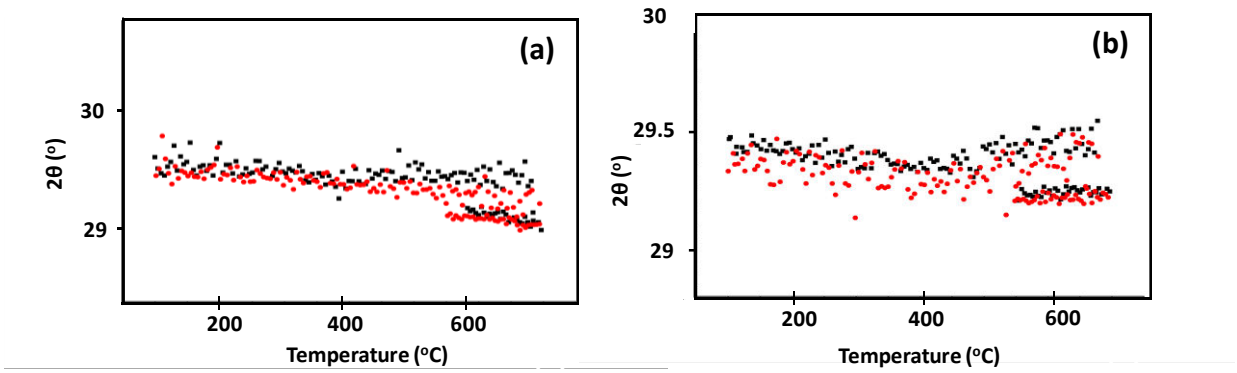

Figure B.13 –$CeZrO_2$ peak position during: a) Reduction, H_2-TPR cycles 1,2 and b) Oxidation, CO_2-TPO cycles 1,2. (■)cycle 1 (■) cycle 2

- 20wt% $NiFe_2O_4$-$CeZrO_2$

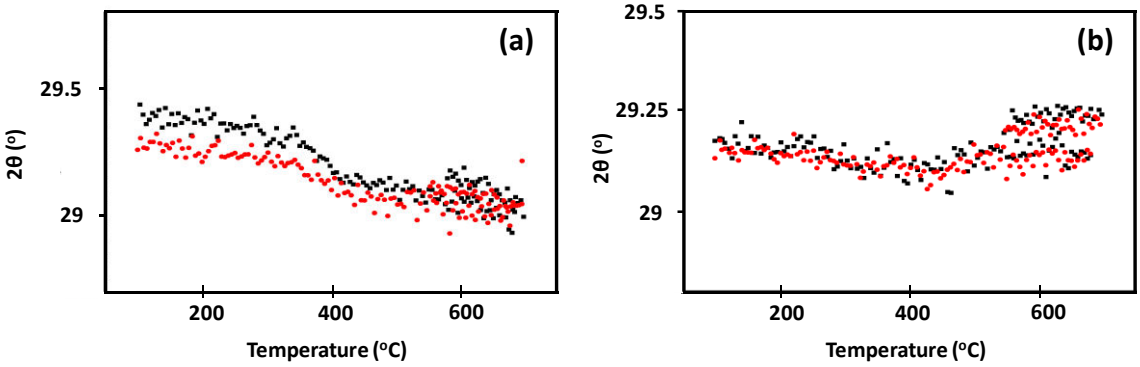

Figure B.14 –$CeZrO_2$ peak position during: a) Reduction, H_2-TPR cycles 1,2 and b) Oxidation, CO_2-TPO cycles 1,2. (■)cycle 1 (■) cycle 2

REDOX PROPERTIES: TPR/TPO

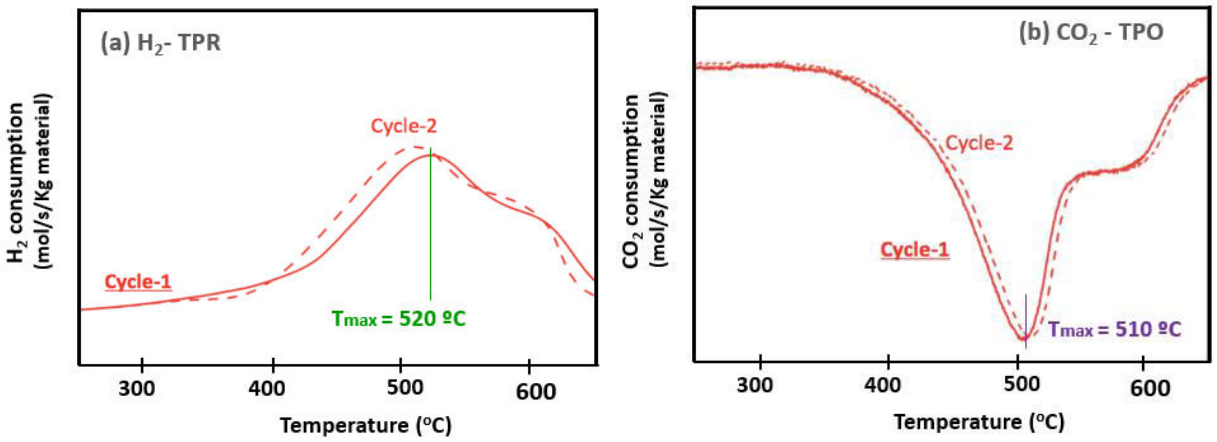

Figure B.15 –Redox properties of 50wt%$CoFe_2O_4$-$CeZrO_2$ during. a) H_2-TPR and b) CO_2-TPO.

(———) $CoFe_2O_4$ cycle1, (.....) $CoFe_2O_4$ cycle 2

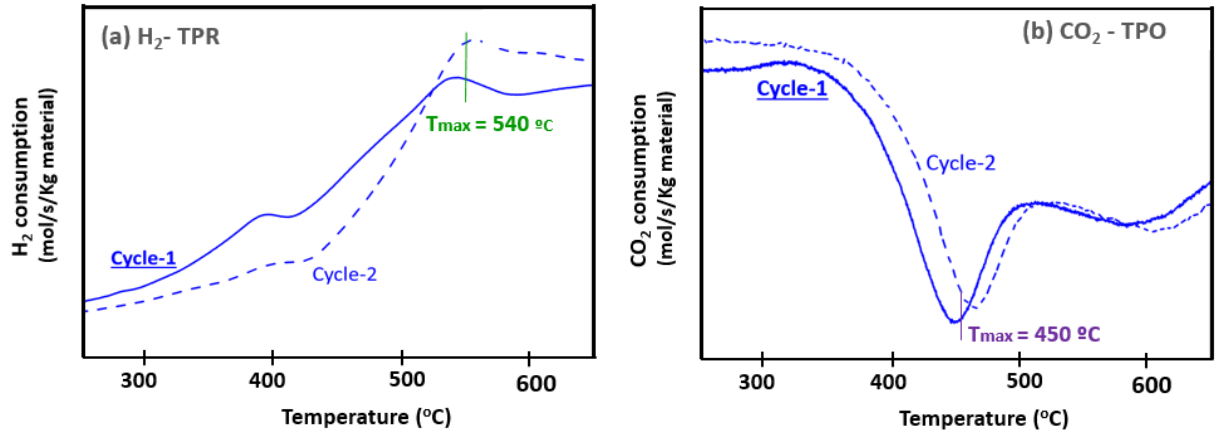

Figure B.16 –Redox properties of 50wt%$NiFe_2O_4$-$CeZrO_2$ during. a) H_2-TPR and b) CO_2-TPO.

(———) $CoFe_2O_4$ cycle1, (.....) $CoFe_2O_4$ cycle 2

STABILITY AND ACTIVITY: ISOTHERMAL IN SITU XRD CYCLES

- 20wt% $CoFe_2O_4$-$CeZrO_2$

Temperature 500 °C

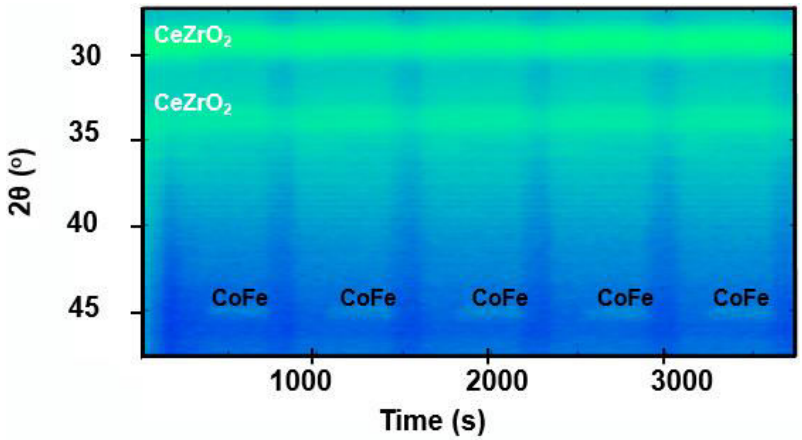

Figure B.17 – In-situ XRD isothermal redox cycles at 500 °C for 20wt% $CoFe_2O_4$ / 80wt%$CeZrO_2$

Temperature 750 °C

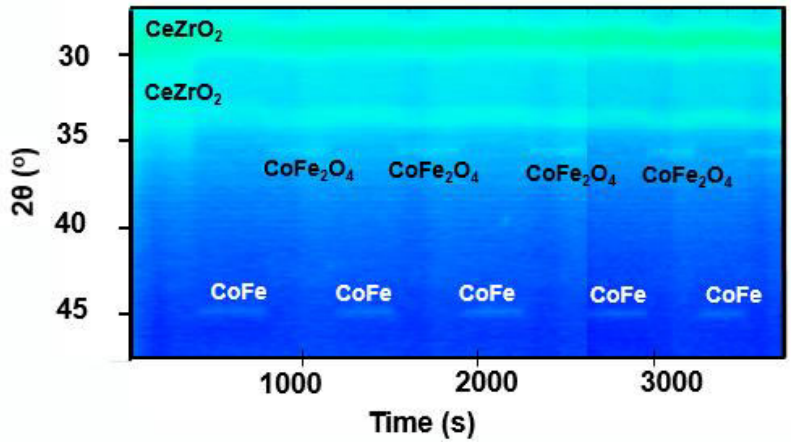

Figure B.18 – In-situ XRD isothermal redox cycles at 750 °C for 20wt% $CoFe_2O_4$ / 80wt%$CeZrO_2$

- 20wt% $NiFe_2O_4$-$CeZrO_2$

Temperature 750 °C

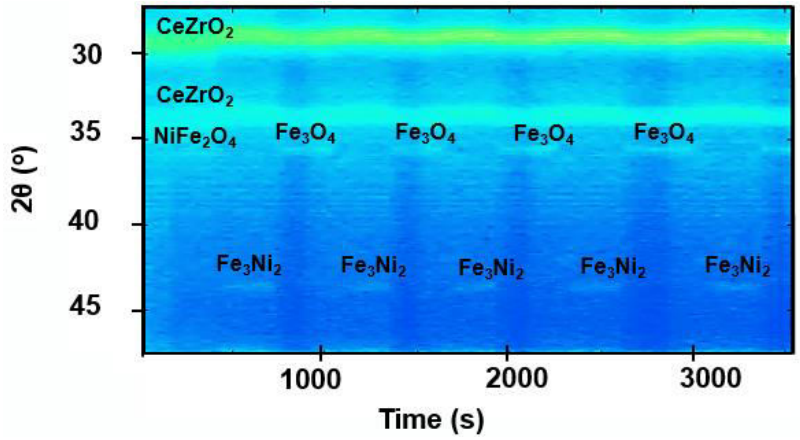

Figure B.19 – In-situ XRD isothermal redox cycles at 750 °C for 20wt% $NiFe_2O_4$ / 80wt%$CeZrO_2$

REFERENCES

[1] J. Adanez, A. Abad, F. Garcia-Labiano, P. Gayan, and L. F. De Diego, “Progress in chemical-looping combustion and reforming technologies,” *Prog. Energy Combust. Sci.*, vol. 38, no. 2, pp. 215–282, 2012.

[2] B. Lindström, “Hydrogen generation by steam reforming of methanol over copper-based catalysts for fuel cell applications,” *Int. J. Hydrogen Energy*, vol. 26, no. 9, pp. 923–933, 2001.

[3] N. Mitra, P. Umasankar, K. Vasudeva, and S. C. Dhingra, “Steam Reforming of Ethanol for Hydrogen Production: Thermodynamic Analysis,” *Int. J. Hydrogen Energy*, vol. 21, no. I, pp. 13–18, 1996.

[4] V. V Galvita, H. Poelman, V. Bliznuk, C. Detavernier, and G. B. Marin, “CeO 2 -Modified Fe 2 O 3 for CO 2 Utilization via Chemical Looping,” *Ind. Eng. Chem. Res.*, vol. 52, no. 25, pp. 8416–8426, 2013.

[5] Y. Choi and H. G. Stenger, “Water gas shift reaction kinetics and reactor modeling for fuel cell grade hydrogen,” *J. Power Sources*, vol. 124, no. 2, pp. 432–439, 2003.

[6] C. D. Bohn, J. P. Cleeton, C. R. Müller, J. F. Davidson, a N. Hayhurst, S. a Scott, and J. S. Dennis, “The Kinetics of the Reduction of Iron Oxide by Carbon Monoxide Mixed with Carbon Dioxide,” *AIChE J.*, vol. 56, no. 4, pp. 1016–1029, 2010.

[7] V. V. Galvita, H. Poelman, C. Detavernier, and G. B. Marin, “Catalyst-assisted chemical looping for CO2 conversion to CO,” *Appl. Catal. B Environ.*, vol. 164, pp. 184–191, 2015.

[8] V. V. Galvita, H. Poelman, and G. B. Marin, “Hydrogen production from methane and carbon dioxide by catalyst-assisted chemical looping,” *Top. Catal.*, vol. 54, no. 13–15, pp. 907–913, 2011.

[9] V. J. Aston, B. W. Evanko, and A. W. Weimer, “Investigation of novel mixed metal ferrites for pure H 2 and CO 2 production using chemical looping,” *Int. J. Hydrogen Energy*, vol. 38, no. 22, pp. 9085–9096, 2013.

[10] A. Evdou, V. Zaspalis, and L. Nalbandian, “Ferrites as redox catalysts for chemical looping processes,” *Fuel*, vol. 165, pp. 367–378, 2016.

[11] A. N. V. R. Dharanipragadaa, L. Buelens, H. Poelman, E. De Grave, V. Galvita, and G. B. Marin, “Mg-Fe-Al-O for advanced CO2 to CO conversion: carbon monoxide yield vs. oxygen storage capacity,” *J. Mater. Chem. A*, vol. 3, pp. 16251–16262, 2015.

[12] P. R. D. Elivery, S. T. C. Onversion, A. P. P. U. E. Ducation, and O. Utreach, “NATIONAL

HYDROGEN," no. November, 2002.

[13] I. E. Agency, "HYDROGEN PRODUCTION AND STORAGE."

[14] "HYDROGEN : FUEL OF THE FUTURE Rachel Chamousis," 2000.

[15] J. Zhu, D. Zhang, and K. D. King, "Reforming of CH4 by partial oxidation: Thermodynamic and kinetic analyses," *Fuel*, vol. 80, no. 7, pp. 899–905, 2001.

[16] C. Trevisanut, "A chemical-loop approach for the generation of hydrogen by means of ethanol reforming," 2014.

[17] Y. Matsumura and T. Nakamori, "Steam reforming of methane over nickel catalysts at low reaction temperature," *Appl. Catal. A Gen.*, vol. 258, no. 1, pp. 107–114, 2004.

[18] T. (PhD) Lipman, "An overview of hydrogen production and storage systems with renewable hydrogen case studies."

[19] C. Trevisanut, M. Mari, J. M. M. Millet, and F. Cavani, "Chemical-loop reforming of ethanol over metal ferrites: An analysis of structural features affecting reactivity," *Int. J. Hydrogen Energy*, vol. 40, no. 15, pp. 5264–5271, 2014.

[20] S. Uemiya, N. Sato, H. Ando, T. Matsuda, and E. Kikuchi, "Steam Reforming of Methane in a Hydrogen-Permeable Membrane Reactor," *Appl. Catal.*, vol. 67, no. 2, pp. 223–230, 1991.

[21] V. Galvita, T. Schröder, B. Munder, and K. Sundmacher, "Production of hydrogen with low COx-content for PEM fuel cells by cyclic water gas shift reactor," *Int. J. Hydrogen Energy*, vol. 33, no. 4, pp. 1354–1360, 2008.

[22] S. Cocchi, M. Mari, F. Cavani, and J. M. M. Millet, "Chemical and physical behavior of CoFe2O4 in steam-iron process with methanol," *Appl. Catal. B Environ.*, vol. 152–153, no. 1, pp. 250–261, 2014.

[23] D. L. Trimm, "Minimisation of carbon monoxide in a hydrogen stream for fuel cell application," *Appl. Catal. A Gen.*, vol. 296, no. 1, pp. 1–11, 2005.

[24] S. Abanades and H. I. Villafan-Vidales, "CO2 and H2O conversion to solar fuels via two-step solar thermochemical looping using iron oxide redox pair," *Chem. Eng. J.*, vol. 175, no. 1, pp. 368–375, 2011.

[25] A. Hedayati, A. M. Azad, M. Rydén, H. Leion, and T. Mattisson, "Evaluation of novel ceria-supported metal oxides as oxygen carriers for chemical-looping combustion," *Ind. Eng. Chem. Res.*, vol. 51, no. 39, pp. 12796–12806, 2012.

[26] M. Najera, R. Solunke, T. Gardner, and G. Veser, “Carbon capture and utilization via chemical looping dry reforming,” *Chem. Eng. Res. Des.*, vol. 89, no. 9, pp. 1533–1543, 2011.

[27] E. Manova, T. Tsoncheva, C. Estourn??s, D. Paneva, K. Tenchev, I. Mitov, and L. Petrov, “Nanosized iron and iron-cobalt spinel oxides as catalysts for methanol decomposition,” *Appl. Catal. A Gen.*, vol. 300, no. 2, pp. 170–180, 2006.

[28] K. Svoboda, A. Siewiorek, D. Baxter, J. Rogut, and M. Poho??el??, “Thermodynamic possibilities and constraints for pure hydrogen production by a nickel and cobalt-based chemical looping process at lower temperatures,” *Energy Convers. Manag.*, vol. 49, no. 2, pp. 221–231, 2008.

[29] J. Adánez, F. García-Labiano, L. F. De Diego, P. Gayán, J. Celaya, and A. Abad, “Nickel-copper oxygen carriers to reach zero CO and H2 emissions in chemical-looping combustion,” in *Industrial and Engineering Chemistry Research*, 2006, vol. 45, no. 8, pp. 2617–2625.

[30] J. R. Scheffe, M. D. Allendorf, E. N. Coker, B. W. Jacobs, A. H. McDaniel, and A. W. Weimer, “Hydrogen production via chemical looping redox cycles using atomic layer deposition-synthesized iron oxide and cobalt ferrites,” *Chem. Mater.*, vol. 23, no. 8, pp. 2030–2038, 2011.

[31] S. Cocchi, “A chemical loop approach for methanol reforming,” *Amsdottorato.Cib.Unibo.It*, 2012.

[32] M. A. Ebiad, D. R. Abd El-Hafiz, R. A. Elsalamony, and L. S. Mohamed, “Ni supported high surface area CeO2-ZrO2 catalysts for hydrogen production from ethanol steam reforming,” *RSC Adv.*, vol. 2, no. 21, pp. 8145–8156, 2012.

[33] Y. Matsumura, N. Tode, T. Yazawa, and M. Haruta, “Catalytic methanol decomposition to carbon monoxide and hydrogen over NiSiO2 of high nickel content,” *J. Mol. Catal. A Chem.*, vol. 99, no. 3, pp. 183–185, 1995.

[34] D. K. Liguras, D. I. Kondarides, and X. E. Verykios, “Production of hydrogen for fuel cells by steam reforming of ethanol over supported noble metal catalysts,” *Appl. Catal. B Environ.*, vol. 43, no. 4, pp. 345–354, 2003.

[35] I. Fishtik, A. Alexander, R. Datta, and D. Geana, “A thermodynamic analysis of hydrogen production by steam reforming of ethanol via response reactions,” *Int. J. Hydrogen Energy*, vol. 25, no. 1, pp. 31–45, 2000.

[36] V. V. Galvita, G. L. Semin, V. D. Belyaev, V. a. Semikolenov, P. Tsiakaras, and V. a. Sobyanin, “Synthesis gas production by steam reforming of ethanol,” *Appl. Catal. A Gen.*, vol. 220, no. 1–2, pp. 123–127, 2001.

[37] J. C. Brown and E. Gulari, “Hydrogen production from methanol decomposition over Pt/Al 2O3 and ceria promoted Pt/Al2O3 catalysts,” *Catal. Commun.*, vol. 5, no. 8, pp. 431–436, 2004.

[38] Y. Matsumura, K. Kuraoka, T. Yazawa, and M. Haruta, “Production of carbon monoxide and hydrogen by methanol decomposition over nickel dispersed on porous glass,” *Catal. Today*, vol. 45, no. 1–4, pp. 191–196, 1998.

[39] T. Tsoncheva, L. Ivanova, C. Minchev, and M. Fröba, “Cobalt-modified mesoporous MgO, ZrO2, and CeO2 oxides as catalysts for methanol decomposition,” *J. Colloid Interface Sci.*, vol. 333, no. 1, pp. 277–284, 2009.

[40] Z. R. S. and L. M. C. Park J., “Thermal decomposition of ethanol. 1. Ab Initio MO/RRKM Prediction of rate constant and product branching ratios,” *J. Chem. Inf. Model.*, vol. 53, no. 9, pp. 1689–1699, 2013.

[41] S. Zare, A. a. Ati, S. Dabagh, R. M. Rosnan, and Z. Othaman, “Synthesis, structural and magnetic behavior studies of Zn–Al substituted cobalt ferrite nanoparticles,” *J. Mol. Struct.*, vol. 1089, pp. 25–31, 2015.

[42] M. Sangmanee and S. Maensiri, “Nanostructures and magnetic properties of cobalt ferrite (CoFe 2O4) fabricated by electrospinning,” *Appl. Phys. A Mater. Sci. Process.*, vol. 97, no. 1, pp. 167–177, 2009.

[43] M. George, S. S. Nair, K. A. Malini, P. A. Joy, and M. R. Anantharaman, “Finite size effects on the electrical properties of sol-gel synthesized CoFe2O4 powders: deviation from Maxwell-Wagner theory and evidence of surface polarization effects,” *J. Phys. D-APPLIED Phys.*, vol. 40, no. 6, pp. 1593–1602, 2007.

[44] E. Hema, A. Manikandan, P. Karthika, S. A. Antony, and B. R. Venkatraman, “A Novel Synthesis of Zn2+-Doped CoFe2O4 Spinel Nanoparticles: Structural, Morphological, Opto-magnetic and Catalytic Properties,” *J. Supercond. Nov. Magn.*, vol. 28, no. 8, pp. 2539–2552, 2015.

[45] S. M. Montemayor, L. A. García-Cerda, J. R. Torres-Lubián, and O. S. Rodríguez-Fernández, “Comparative study of the synthesis of CoFe2O4 and NiFe2O4 in silica through the polymerized complex route of the sol-gel method,” *J. Sol-Gel Sci. Technol.*, vol. 42, no. 2, pp. 181–186, 2007.

[46] H. Stanjek and W. Häusler, “Basics of X-ray diffraction,” *Hyperfine Interact.*, vol. 154, pp. 107–119, 2004.

[47] R. S. Devoto, “Transport properties of ionized monoatomic gases,” *Phys. fluids*, vol. 9, p. 1230,

1966.

[48] a Trunschke, “Surface area and pore size determination,” *Mod. Methods Heterog. Catal. Res.*, vol. 1, no. November, 2013.

[49] Y. Fujita, “The Determination Method of Surface Area by the BET Method,” *Shinku*, vol. 6, no. 5, pp. 169–176, 1963.

[50] N. Leddy, “SURFACE AREA AND Adsorption,” *C. Anal.*, vol. 5, pp. 23–64, 2012.

[51] S. A. Theofanidis, R. Batchu, V. V. Galvita, H. Poelman, and G. B. Marin, “Carbon gasification from Fe-Ni catalysts after methane dry reforming,” *Appl. Catal. B Environ.*, vol. 185, pp. 42–55, 2016.

[52] X. Diffraction and I. Sources, “Bragg ’ s Law,” *Production*, vol. 5, no. 6, pp. 371–372, 1970.